

Mesophases in Molecular and Granular Systems: From Liquid Crystalline Polymers to Granular Rods

Der Universität Bayreuth
zur Erlangung des Grades eines
Doktors der Naturwissenschaften (Dr. rer. nat.)
vorgelegte Abhandlung

von

Thomas Müller

geboren am 19.04.1985

in Pegnitz

1. Gutachter: Prof. Dr. Ingo Rehberg (Universität Bayreuth)
2. Gutachter: Prof. Dr. Lothar Kador (Universität Bayreuth)
3. Gutachter: Prof. Dr. Igor Aronson (University of Chicago, USA)

Tag der Einreichung: 19.05.2015

Tag des Kolloquiums: 26.11.2015

Kurzdarstellung

Die nematisch flüssigkristalline Phase stellt ein typisches Beispiel einer Mesophase eines thermodynamischen Systems dar. Sie zeichnet sich durch eine langreichweitige Orientierungsordnung bei gleichzeitig fehlender Positionsordnung der Moleküle aus und wird deshalb als zusätzlicher Zustand zwischen einer konventionellen Flüssigkeit und einem festen Kristall eingeordnet. Dabei ist die Anisotropie der einzelnen Moleküle eine notwendige Bedingung für das Auftreten der Mesophase. Entsprechend sind in einer nematischen Substanz die Moleküle typischerweise durch ein längliches Profil ausgezeichnet. In ähnlicher Art und Weise kann auch Granulat, also eine Ansammlung vieler makroskopischer Teilchen, durch Einwirken einer äußeren Anregung eine gewisse Orientierungsordnung ausbilden. Die Anisotropie der einzelnen Bestandteile ist auch hier eine notwendige Voraussetzung. Um einen Einblick in die Gemeinsamkeiten und Unterschiede mesomorpher Zustände in thermischen und athermischen Systemen zu geben, nimmt diese Arbeit auf experimentelle Ergebnisse in molekularen sowie in granularen Systemen Bezug.

Der erste Abschnitt schildert ein thermisches System bei dem ein nematischer Flüssigkristall mit geringem Molekulargewicht als Hauptkomponente verwendet wird. Dabei wird in binären Mischungen mit durch mesogene Seitenketten funktionalisierten Blockcopolymeren der Einfluss des Polymers auf den Nematiten untersucht. Die Mikrophasenseparation der Polymerendblöcke und das Überschreiten einer kritischen Konzentration führen zur Ausbildung eines physikalischen Netzwerks, was einen gelierten Zustand des Nematiten mit sich bringt. Im Gegensatz dazu verhalten sich die Mischungen unterhalb der kritischen Konzentration wie gewöhnliche Nematiten, einschließlich ihrer typischen doppelbrechenden Charakteristika. Zur Bestimmung der viskoelastischen Eigenschaften solcher verdünnter Mischungen wurden unter Zuhilfenahme eines Polarisationsmikroskops dynamische elektrooptische Messungen durchgeführt. Dabei wurde mit zunehmender Polymerkonzentration ein Anstieg der Rotationsviskosität festgestellt. Die Ergebnisse können sowohl zur Dimensionsabschätzung der durch Selbstassemblierung entstandenen Polymercluster, als auch zur Bestimmung des Gelpunktes verwendet werden.

Zusätzlich zu den Ergebnissen der ersten Publikation sind auch Untersuchungen über die Langzeitstabilität der verdünnten Lösungen Bestandteil dieser Arbeit. Auf langen Zeitskalen wurde eine Abnahme der Rotationsviskosität beobachtet, was durch eine effektive Abnahme der Polymerkonzentration beschrieben werden kann. Außerdem wurden mit Hilfe der Polarisationsmikroskopie in einigen der binären Mischungen regelmäßige Strukturen detektiert, welche an Suspensionen kolloidaler Teilchen in einem Nematiten erinnern. Solch eine Verformung des ansonsten gleichförmigen Direktorfelds wird auf eine Aggregation vieler Polymerketten in große Cluster

zurückgeführt. Die thermische Behandlung des Materials und das elektrooptische Verhalten der Strukturen werden im Rahmen dieser Arbeit diskutiert. Außerdem wird ein phänomenologisches Modell für die Verteilung des Direktors in der Nähe der Agglomeration vorgestellt.

Der letzte Teil über molekulare Systeme nimmt auf die zweite Publikation Bezug, in welcher experimentelle Untersuchungen von Mischungen oberhalb der kritischen Polymerkonzentration beschrieben sind. Im Gegensatz zu den gering konzentrierten Proben liefert dieser gelierte Zustand des Flüssigkristalls aufgrund des Netzwerks eine Polydomänenstruktur, was zu einer starken Streuung des Lichts führt. Durch starke elektrische Felder ist es allerdings möglich eine bevorzugt parallele Ausrichtung der Flüssigkristallmoleküle zu erzeugen. Somit kann von einem opaken in einen transparenteren Zustand umgeschaltet werden. Eine Analyse dieses elektrisch induzierten Schaltverhaltens und der rheologischen Charakteristika liefert eine Beziehung zwischen den physikalischen Eigenschaften des Gels und einer Variation der Struktur des Blockcopolymers.

Im zweiten Abschnitt dieser Arbeit werden makroskopische, granulare Systeme behandelt. Den Untersuchungen der dritten Publikation entsprechend wird dabei insbesondere die Orientierungsordnung in einer Monolage vertikal angeregter zylinderförmiger Stäbchen beschrieben. In solch einem quasi-zweidimensionalen System können je nach Längen-Durchmesser-Verhältnis der Zylinderstifte zwei unterschiedliche Arten mesomorpher Zustände beobachtet werden. Während kurze Stäbchen einen tetraischen Zustand mit vierfacher Rotationssymmetrie ausbilden, findet man in Systemen mit längeren Stäbchen eine einachsige nematische Ordnung. Für das Auftreten eines geordneten Zustandes ist die Packungsdichte der Teilchen ein entscheidender Parameter, die Frequenz und Stärke der vertikalen Anregung spielen hingegen keine große Rolle. Die Zustandsdiagramme von getriebenem Granulat und entsprechenden Monte-Carlo-Simulationen weisen einige Gemeinsamkeiten auf, wodurch eine gewisse Universalität bei der Anordnung stäbchenförmiger Teilchen in Nichtgleichgewichts- und Gleichgewichtssystemen verdeutlicht wird.

Zum Abschluss dieser Arbeit wird der dissipative Charakter granularer Materie beleuchtet. Außer Reibung und inelastischen Stößen kann bei der Wechselwirkung makroskopischer Teilchen auch eine Flüssigkeitsschicht auf deren Oberfläche zu einem Energieverlust führen. In solch einem Fall müssen viskose Dämpfung, Kapillarbrücken, sowie die Trägheit der Flüssigkeit berücksichtigt werden. Im Rahmen der vierten Publikation wurde der senkrechte Aufprall einer frei fallenden Kugel auf einer mit Flüssigkeit benetzten ebenen Oberfläche experimentell untersucht. Dabei konnte mit Hilfe des normalen Restitutionskoeffizienten der dissipative Einfluss der Flüssigkeit quantifiziert werden. Viele Parameter, wie Aufprallgeschwindigkeit, Kugelgröße, Filmdicke und Viskosität der Flüssigkeit, haben einen Einfluss auf den Wert des Restitutionskoeffizienten. Mit Hilfe der Stokeszahl ist eine Normierung möglich. Experimentelle Ergebnisse einer Variation der Materialeigenschaften der Kugel legen eine allgemeingültige Anwendbarkeit solch einer Normierung, abhängig vom Größen- und Dichteverhältnis zwischen Kugel und Flüssigkeitsschicht, nahe.

Abstract

The nematic liquid crystalline phase constitutes one of the most prominent examples of a mesophase. Characterized by long range orientational order and no positional order of the single constituents, it is classified as an intermediate phase between a liquid and a solid crystal. In thermodynamic systems, the anisotropy of the molecules is a necessary requirement for the appearance of a mesophase. Thus, typical nematic substances are characterized by an elongated molecular shape. Similarly, a conglomeration of agitated macroscopic particles can also exhibit orientational order, when the components satisfy the condition of shape-anisotropy. Considering the experimental results of both molecular and granular systems, this thesis gives insights into similarities as well as dissimilarities of mesomorphic states in thermal and athermal systems.

The first section highlights a particular thermal system where a low molecular weight nematic liquid crystal is used as the main component. In binary mixtures with mesogenic side-chain block copolymers, the influence of the polymer on the nematic host is investigated in detail. Above a critical concentration, microphase separation of the polymer end blocks yields the formation of physical bonds and a polymeric network, resulting in a gellified state. In contrast, below the gelation point, the mixtures behave like usual nematics and demonstrate typical birefringent features. Dynamical electro-optical measurements with polarizing microscopy were performed in order to determine some of the viscoelastic properties in the dilute regime. The measurements reveal an increase of rotational viscosity with increasing concentration of polymer. The data can be utilized to estimate the cluster size of the self-assembled block copolymer chains and to determine the gelation point of the system.

In addition to the results of the first publication, the long term stability of the dilute solutions is another topic of this thesis. At long time scales, a redcrease of the rotational viscosity could be observed, comparable to an effective loss of polymer concentration. Moreover, using polarizing microscopy, micron-sized regular patterns were detected in some of the binary mixtures, reminding of suspensions of colloidal particles in a nematic solvent. In the dilute polymeric mixtures, the local distortions of the otherwise well aligned nematic director field is attributed to the aggregation of many polymer chains into big clusters. Investigations on the thermal treatment and the electro-optical response are discussed in this work. Furthermore, a phenomenological model for the director distribution around the agglomerate is proposed.

The last part about molecular systems refers to the second publication, where investigations on mixtures above the critical concentration of block copolymer are described. In contrast to the mostly planar alignment of the director in the dilute

regime, in the gelified state, the network formation yields a polydomain structure that strongly scatters light. Strong electric fields can be applied in order to realign the liquid crystal molecules and to switch from the opaque into a more transparent state. The electrically induced switching behavior and the rheological characteristics are used to identify the physical properties of the gel and to relate them with various block copolymer structures.

In the second part of this thesis, macroscopic granular systems are discussed. In particular, the orientational order in a monolayer of vertically agitated cylindrical rods is described, according to the investigations that are presented in the third publication. Dependent on the length to width ratio of the rods, the quasi-two-dimensional system displays two types of mesomorphic states. While short rods form a tetratic state with fourfold rotational symmetry, longer rods prefer uniaxial nematic ordering. The area density is identified as the crucial parameter for the occurrence of ordered states, while the frequency and the strength of the vertical agitation do not play a major role. A quantitative comparison between the experimental results of the agitated rods and the corresponding equilibrium Monte Carlo simulations can be drawn in terms of state diagrams for both systems. Strong similarities illustrate some kind of universality between the ordering of rod-shaped particles in nonequilibrium and equilibrium systems.

The last part of the thesis sheds light on the dissipative nature of granular matter. Apart from frictional forces and inelastic impacts, wet surfaces can cause additional dissipation of energy during the interaction of granular particles. Then, viscous damping, the formation and rupture of capillary bridges and the inertia of the liquid have to be taken into account. Within the framework of the fourth publication, the normal impact of a freely falling sphere on a wet flat surface has been investigated experimentally. The coefficient of normal restitution was used to detect the amount of dissipated energy due to the wetting. It is dependent on many parameters, like impact velocity, sphere size, film thickness and viscosity of the liquid layer. A scaling of the coefficient of restitution with the Stokes number was found. A variation of the material properties of the impacting sphere suggests an ubiquitous application of this scaling, dependent on the size ratio and the density ratio between the sphere and the liquid film.

Contents

Kurzdarstellung	3
Abstract	5
1 Mesophases in Molecular and Granular Systems	9
1.1 Introduction	9
1.2 Molecular Systems	14
1.2.1 Liquid crystals	14
1.2.2 Functionalized block copolymers in nematic liquid crystals . .	20
1.2.3 Director defects in a mixture of a block copolymer and a nematic liquid crystal	25
1.2.4 Liquid crystalline gels	32
1.3 Granular Systems	35
1.3.1 Anisotropic granular matter	36
1.3.2 Driven monolayers of granular rods	37
1.3.3 Dissipative mechanisms in granular matter	40
1.4 Conclusions and Outlook	45
2 Publications	49
2.1 Gel formation in a mixture of a block copolymer and a nematic liquid crystal	51
2.2 Structure-Property Relations of Liquid Crystalline Gels with ABA- Triblock Copolymers as Gelators	65
2.3 Ordering of Granular Rod Monolayers Driven Far from Thermodynamic Equilibrium	87
2.4 Scaling of the Normal Coefficient of Restitution for Wet Impacts . .	97
A Appendix	103
Bibliography	105

1 Mesophases in Molecular and Granular Systems

1.1 Introduction

A piece of ice placed in a pot on the hot plate of a stove seems to be no big mystery to the general public. Experience has taught everybody what is going to happen with the frozen substance during an increase of temperature. The ice will start to melt, the water will start to boil and finally, vapor will fill the area above. In a physical sense, H_2O undergoes transitions between the three classical states that matter can be found in: solid, liquid and gaseous. But what is the definition of such a state of matter? Are there any further states besides the three outlined above? And if so, can they be observed at ambient conditions in everyday life?

It was 500 to 600 B.C., when the ancient Greeks were starting to give an explanation of the physical world without referring to supernatural things. Philosophers like Thales, Anaximenes and Heraclitus suggested one fundamental material as the basis of everything. Later on, Empedocles came up with his theory of four classical elements: earth, water, air and fire. For example, a bucket inverted in water and a pocket of air remaining trapped inside the bucket was one of Empedocles' simple experiments, convincing him of the fact that air and water must be separate substances (Russel, 2004). His theory of four basic elements, sometimes extended to a fifth heavenly element called aether, persisted throughout hundreds of years until the Middle Ages.

In the 18th century, careful quantitative experiments on the transformation of matter were carried out by European scientists and a macroscopic theoretical description was introduced in a more consistent way. This was the time when Benjamin Thompson, Robert Mayer, James P. Joule and many others found empirical laws that are still the basis of today's thermodynamic descriptions. In the 1850s, William Thomson and Rudolf Clausius formulated their principles of thermodynamics. At the same time, John Dalton reasserted the concept of substructure of matter in terms of molecules and atoms. Although the idea that matter is consisting of discrete building blocks was already proposed by the Greek philosophers Leucippus and Democritus in the 4th and 5th century B.C., it was not followed up for hundreds of years (Olmsted & Williams, 1997; Wachter & Hoerber, 2005).

Nowadays, the specific properties of a state of matter can be described on a microscopical level by forces between the atoms or molecules. For example, in the solid state the molecular centers of mass have fixed equilibrium positions. Located in a three-dimensional periodic lattice with long range positional order, the molecules form a classical solid crystal, like ordinary ice. In a noncrystalline amorphous solid,

like conventional glass, such a long range order is missing. Generally in a solid state, the forces between the molecules are short-ranged and only vibrations around the fixed positions are possible. In contrast, in a liquid substance the molecules have enough energy for lateral movements against each other, but due to the relatively close packing, friction still limits their movement. In the gaseous state however, the thermal energy is very large. On average the molecules are far away from each other, the forces between them can be neglected and thus they can freely move around without exhibiting any positional order (Meschede, 2006; Khoo & Simoni, 1991).

With his principles of thermodynamics, the American physicist Josiah W. Gibbs laid the foundation of the theory about the phases of matter. His publication "On the Equilibrium of Heterogeneous Substances", which came up between 1876 and 1878, is certainly one of his most famous works. Gibbs considered each state of matter to be a phase, while each single substance of a system was defined as one component. Thus, a phase, classified by one state of matter, describes the homogeneous area within a macroscopic substance that is delimited by a well-defined boundary (Gibbs, 2015; Meschede, 2006). With this definition, a single-component system can simultaneously occur in various phases of unequal state of matter. Consequently, it is no contradiction that solid ice, liquid water and gaseous vapor can coexist simultaneously, if temperature and pressure are adjusted properly. In general, the number of coexisting phases in thermodynamic equilibrium can be described by Gibbs' phase rule, which he also published in 1878 (Lüders & von Oppen, 2008; Gibbs, 1878).

The interaction between a thermodynamic system and its environment can induce the transition of phases, for example by a change of temperature or pressure. An accurate study of phase transitions was triggered by the experimental discovery of a precise set of values of thermodynamic parameters where the liquid-gas transition occurs. Dutch scientists, like Johannes D. van der Waals and Hendrik W. B. Roozeboom, supported Gibbs' ideas with their experimental investigations (Schimank, 1960). In 1873, van der Waals presented his theory for the liquid-gas transition, which was the first understanding of phase transitions from a microscopic perspective (Lüders & von Oppen, 2008). With the liquidation of helium by Heike K. Onnes in 1908 and the observation of an unusual phase transition in liquid helium by Willem H. Keesom in 1932, the request of a clear classification was increasing more and more (Jaeger, 1998).

A general categorization was first introduced by Paul Ehrenfest in 1933, where he considered Gibbs free energy as a function of thermodynamic variables (Jaeger, 1998). In his definition, any order of phase transition was defined by the lowest order of derivative that offers a discontinuity (Nolting, 2005). In the following years, this classification was increasingly utilized in discussions of liquid-gas, order-disorder, paramagnetic-ferromagnetic and normal-superconducting phase transitions. However, with time, Ehrenfest's definition illustrated several inaccuracies leading to the adoption of a simplified version in the 1970s (Jaeger, 1998). In modern physics, a binary classification is used, where the type of transition is determined by the continuity of entropy as a function of temperature at the transition point (Nolting, 2005). In 1982, the Nobel prize in physics was awarded to Kenneth Wilson for

his theory on critical phenomena in connection with phase transitions. This gives evidence that the understanding of the physics behind phase transitions is still of fundamental interest and anything but a solved problem.

The three classical states of matter as well as the transitions between them are probably the most familiar ones. Thus, it is obvious that only liquid, solid and gaseous phases were known in former times. However, during many years of research, particular conditions have been found under which some substances display a variety of physical states, differing from a typical solid, liquid or gas. For example, nonclassical states like a superfluid or a Bose-Einstein condensate can be generated at very low temperatures. In contrast, at very high temperatures, a material in the gaseous state might reach a very high degree of ionization and show up in the so called plasma state. The lightning during a thunderstorm or the neon lights of billboards are two well known examples of such a plasma.

However, extreme conditions are not always necessary for the appearance of non-classical states. At ambient conditions, the liquid crystalline state is probably one of the most prominent examples with the highest technical relevance. Electronic display devices like smartphones, tablet computers, laptops or flat screen TVs certainly would have never found their way into everyday life without the development of materials showing such a nonclassical state. In liquid crystals, anisotropic molecules hold long range orientational order as well as a reduced or even no positional order. Thus, they have simultaneously features of a liquid and a crystalline state, classifying them to be in an intermediate state. Reminiscent to the ancient Greek word *mesos* ($\mu\epsilon\sigma\omicron\varsigma$) for intermediate, the liquid crystalline state or phase is therefore often called a mesomorphic state or mesophase, respectively (de Gennes & Prost, 2006). Figure 1.1 (a-c) shows a macroscopic view on a typical liquid crystalline substance in its mesomorphic state and a microscopic illustration of the molecular arrangement in the isotropic and the anisotropic state.

Theoretical descriptions of the formation of liquid crystalline states are often based on entropic excluded volume interactions. A decrease of rotational entropy goes along with the increase of translational entropy. In simple models, like the steric theories from Onsager (1949) and Flory (1956), the anisotropic molecules are often assumed as rigid rods and attractive intermolecular forces are not taken into account. Within these theories, the driving force for ordering is only dependent on geometrical aspects by means of a better packing of rods in the mesophase. In a molecular statistical theory of Maier & Saupe (1959, 1960), rigid rods were also found to be useful for the prediction of an order-disorder transition and the orientational properties of the nematic mesophase. Such purely geometrical aspects and packing problems confirm the search of similarities between systems with microscopic and macroscopic scale.

Granular matter, as a large conglomeration of discrete solid particles, represents a typical example of a physical macroscopic system. The particles are visible to the naked eye and cover dimensions of several orders of magnitude, ranging from simple grains of sand to big floes of ice drifting across the polar seas. Due to their size and mass, the physics of granular particles is not influenced by thermal energy. For example, a small grain of sand with a diameter of 100 micrometers and a mass in the

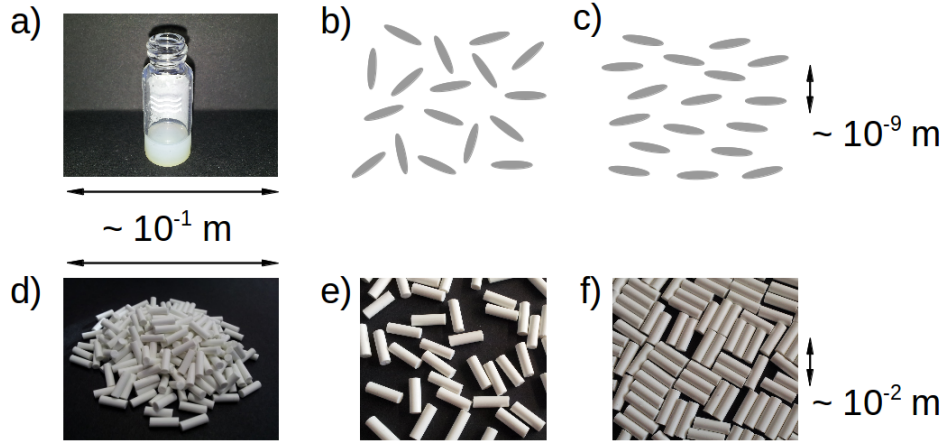


Figure 1.1: Comparison of anisotropic molecular and granular systems used for the experiments described in this thesis. Molecular system: a) a bottle with a portion of a liquid crystalline material; b) illustration of the molecular arrangement in the isotropic liquid phase; c) molecular arrangement in the uniaxial nematic mesophase. Granular system: d) conglomeration of granular rods; e) a granular rod monolayer in an isotropic-like state; f) a granular monolayer in a tetratic-like mesomorphic state.

order of micrograms, gains a potential energy in the order of 10^{-12} Joule when being lifted to a height of one particle diameter. In a thermal system, such an energy would correspond to a temperature of 10^{11} Kelvin. This illustrates that temperature cannot induce the motion of granular particles (Duran, 2000). In spite of being athermal, external agitation can be used to study the collective behavior of granular particles and to compare the granular movement with molecular dynamics.

The definitions and methods of thermodynamic systems are often used for the description of the collective behavior of granular matter. Due to the exhibition of both solid- and fluid-like features, granular systems are often related to an unusual state of matter (Mehta, 2007). As an example, one can consider a pile of sand at rest, where the single grains have fixed positions. Although gravitational forces create macroscopic stresses, the whole conglomerate of amorphous packing remains at rest, similar to a solid-like state. Tilting the pile might lead to the exceeding of the critical angle of repose, and consequently in a movement of particles. Then, a partial fluid-like behavior of grains can be observed on the surface of the pile.

From a technical point of view, both states are applied successfully in a universal robotic gripper, where individual fingers of conventional grippers are replaced by a certain amount of granulate inside of a flexible bag. The deformable liquid-like state is used to adopt the surface of an object, whereas the shift to a solid-like state after the adoption is used to grip the object (Brown *et al.*, 2010). A much older, but not minor important tool is an hourglass, which has already been studied in the middle of the 19th century by Hagen (1852). There, the flowing sand reminds of the

characteristics of conventional fluids, too. It was the poet and natural philosopher Lucretius who first compared the collective behavior of a granular material with a classical fluid:

"One can scoop up poppy seeds with a ladle as easily as if they were water and, when dipping the ladle, the seeds flow in a continuous stream." (Lucretius, ca. 98 - 55 B.C.)

Of course, there are plenty of differences between a granular flow and an ordinary fluid. For example, the avalanche flow on a pile of sand occurs in a narrow boundary layer, thus it is strongly non-Newtonian. But nevertheless, in huge systems of many particles, continuum theories are used successfully to describe the collective behavior of macroscopic particles (Hinrichsen & Wolf, 2004).

Besides of the gravity driven movement of particles, external vibrations can also unlock the solid-like packing of a granular system. In such a driven case, the mobility of the grains is often used to characterize a new effective temperature. If the collisions between the granular particles are infrequent and the effective temperature is high, a gas-like state can be observed. However, inelastic interactions between the grains cause the loss of energy during each collision. Thus, the theory for ideal gases, where purely elastic collisions and energy conservation are assumed, cannot be applied for the granular counterpart.

In spite of many discrepancies from conventional solids, fluids or gases, similarities to thermodynamic systems have been found in various granular systems (Jaeger *et al.*, 1996). Consequently, the occurrence of a mesophase is also expected in granular matter. For example, investigations of driven anisotropic granular particles reveal analogies to molecular liquid crystalline systems. Vibrated rigid rods can be used to generate a mesomorphic state with orientational order of rods under the absence of positional order. Figure 1.1 (d-f) shows typical snapshots of cylindrical granular rods, which were used for the experiments to be described in this thesis.

This work deals with both molecular and granular mesophases. Starting with some basic knowledge about molecular liquid crystalline systems in section 1.2, the influence of functionalized polymers on the properties of the mesophase will be discussed. Related to the results of the first publication (Khazimullin *et al.* (2011), reprint in section 2.1), additional long time studies and pattern formation will be presented. According to the second publication (Pettau *et al.* (2012), reprint in section 2.2), the influence of the polymer geometry on the gelation of a liquid crystalline component will be shown. In section 1.3, anisotropic granular matter will be introduced. The appearance of mesomorphic states during a periodic agitation will be discussed, according to the topic of the third publication (Müller *et al.* (2015), reprint in section 2.3). To capture the essential difference between the thermal liquid crystals and the athermal agitated granular rods, the energy dissipation mechanisms in granular systems will be considered. In particular, referring to the fourth publication (Müller *et al.* (2013b), reprint in section 2.4), a detailed analysis of the coefficient of restitution for wet granular matter will be delivered.

1.2 Molecular Systems

When in 1888 the Austrian botanist Friedrich Reinitzer was trying to determine the melting point of a cholesterol based substance, he recognized some cloudy state between the solid and the liquid phase (Reinitzer, 1888). Excluding effects of impurities and discussing his observations with the German physicist Otto Lehmann, they both came to the conclusion that this state of matter, occurring between "two melting points", must have a unique kind of order. Having both, mechanical properties of a liquid and symmetry properties of a crystal, Lehmann (1889) denominated this new and distinct state of matter as liquid crystal. Being intermediate between a liquid and a crystalline state, a new example of a mesophase was found.

The following sections will give a brief introduction into liquid crystalline systems and their electro-optical properties. Starting from a neat low molecular weight liquid crystal, an example of a side-chain liquid crystalline polymer will be described. The influence of this polymer on various properties of the mesophase will be analyzed for the case of dilute solutions. Finally, the formation of a gelified liquid crystal will be discussed for high concentrations.

1.2.1 Liquid crystals

In molecular systems, various building blocks have been found to induce the formation of a mesomorphic state. Typical examples of these so called mesogens are small organic molecules that are characterized by an anisotropic shape. Various designs are possible, ranging from simple disk-like shapes to more complex geometries such as cones or bananas (Tschierske, 2002; Achard *et al.*, 2003). However, the so-called calamitics (from the Greek word *kalamos* for tube), which have an elongated rod-like shape, are probably the most established liquid crystals.

In many organic systems, like in Reinitzers substances, the occurrence of a liquid crystalline phase is controlled by the adjustment of temperature. Thus, they are commonly denoted as thermotropic systems (de Gennes & Prost, 2006). However, also lyotropic systems are known, where a mixture of components exhibits a liquid crystalline phase, dependent on the concentration of the ingredients. Long helical rods suspended in a liquid substrate represent a typical example. The lengths of such rods can vary from several hundred nanometers, like the macromolecule of the tobacco mosaic virus, to several hundred micrometers, like glass or plastic fibers (Blinov & Chigrinov, 1996).

During the last decades, polymeric systems have been discovered as an additional class of liquid crystalline material. Both, thermotropic systems with the polymer being in a molten state, as well as lyotropic systems, where the polymer is dissolved in an appropriate solvent, can be fabricated. In the latter case, different geometries are possible. On the one side, the polymer chain itself can act as a mesogen. On the other side, mesogenic molecules can be attached to the monomers with spacer of appropriate length and flexibility (Khoo & Simoni, 1991). A particular example of such a functionalized polymer will be discussed in section 1.2.2 of this work. It was

also the subject of investigations in the first two publications, which can be found in section 2.1 and section 2.2 (Khazimullin *et al.*, 2011; Pettau *et al.*, 2012).

The nematic mesophase

In the first two publications (sections 2.1 and 2.2), polymeric liquid crystalline mixtures have been studied, which are based on the calamitic molecule 4-Cyano-4'-pentylbiphenyl (5CB). 5CB is one of the most investigated thermotropic liquid crystals. It is characterized by a simple chemical structure and a high stability against chemical, optical and thermal influences. Moreover, the thermal range of the mesophase includes room temperature, which made 5CB a suitable liquid crystal for the development of first-generation display devices (Gray *et al.*, 1973).

Below its melting temperature of $T_{\text{CN}} = 22.5^\circ\text{C}$ (Chandrasekhar, 1994), 5CB is in a classical solid state, where it exhibits a variety of crystalline structures dependent on the details of thermal treatment (Mansaré *et al.*, 2002). With increasing temperature, the material undergoes a first order phase transition at T_{CN} and turns into its mesomorphic state. In this state, the molecules have a strong tendency of parallel alignment along their long axis, while their centers do not exhibit any long range positional order (see Fig. 1.1 c). Due to the existence of a preferred direction, this mesophase is commonly denoted as uniaxial nematic. The Greek word *nêma* means thread and refers to thread-like structures that are frequently observed with polarizing microscopy. The absence of positional order reflects the fluid-like character of this mesophase and indeed, the nematic state of 5CB macroscopically behaves like an opaque viscous fluid (see Fig. 1.1 a). Further increase of temperature yields a continuous decrease of the orientational order. At the clearing temperature of $T_{\text{NI}} = 35^\circ\text{C}$ (Chandrasekhar, 1994), another weak first order phase transition can be observed, where the substance turns into the isotropic liquid state (see Fig. 1.1 b). Macroscopically, this clearing point can be detected very easily, as the opaque fluid of the nematic phase is becoming transparent (Khoo & Simoni, 1991).

Calamitic mesogens can display several other liquid crystalline phases, differing in the amount of positional and orientational order. While the uniaxial nematic phase has low symmetry and mostly resembles the classical liquid phase, cholesteric (like Reinitzers cholesterol benzoate) or smectic phases (like soap) feature a higher degree of order. They present partial positional order of the centers of mesogens in addition to their long range orientational order. Some thermotropic liquid crystals exhibit a variety of different mesophases. But, in contrast to the transition from the nematic to the isotropic state, the transitions between mesophases can be of second order due to the reduced amount of latent heat (de Jeu, 1980). A first classification of the different liquid crystalline phases was given by the French mineralogist and crystallographer Georges Friedel (1922) in the beginning of the 20th century. His work established much of the current terminology in mesophase physics and was mainly based on the symmetry properties of the individual phases (de Gennes & Prost, 2006).

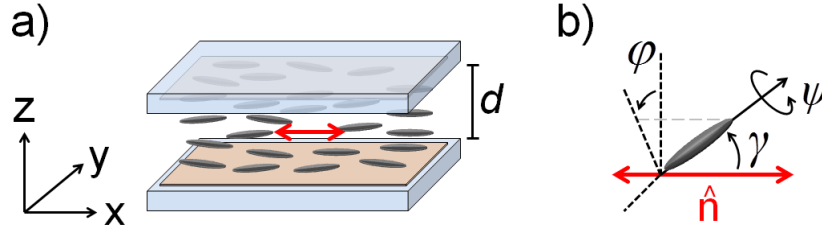


Figure 1.2: a) Sketch of a typical liquid crystal test cell and definition of the coordinate system. The rubbed polyimide coating of the glass induces a planar alignment of the mesogens, represented by the director \hat{n} (red double arrow). b) Illustration of the three Euler angles, defining the orientation of an individual mesogen with respect to the director \hat{n} .

The order parameter

As already mentioned, in a uniaxial nematic phase, the long axis of the cigar-shaped mesogens have a preference of parallel alignment. Thus, a unit vector can be identified that locally labels the mean orientation of mesogens and is commonly known as director \hat{n} . In most cases, the mesogens are geometrically symmetric. Even if they have an intrinsic dipole moment, they tend to align antiparallel, yielding the apolar property $\hat{n} = -\hat{n}$. For a nematic liquid crystal in a confined geometry, the equilibrium state of the director field $\hat{n}(\vec{r})$ is given as the configuration where the total elastic energy of the system is minimized (\vec{r} denotes the position within the volume of the liquid crystal layer). Of course, the liquid crystal interacts with the boundary and thus an additional anchoring has to be considered when calculating the free energy (Blinov & Chigrinov, 1996).

For experimental investigations of physical properties, the liquid crystalline material is typically filled into a transparent test cell. A sketch of this set-up is shown in Fig. 1.2 a. The cell consists of two parallel glass plates that are separated by a spacer of thickness d . The thickness of the liquid crystal layer is usually in the range of $d = 10 \mu\text{m}$ to $50 \mu\text{m}$. Without loss of generality, the plane of the glass corresponds to the x - y -plane of a Cartesian coordinate system. The inside surfaces of the glass are covered with a transparent layer of indium tin oxide in order to enable the application of a voltage and to generate an electric field along the z -direction. An additional polyimide coating on the inside surfaces and mechanical rubbing of this layer induces a planar configuration of the director, which is an alignment of the mesogens parallel to a well-defined direction in the x - y -plane. Further details on the arrangement and the set-up can be found in the first publication (section 2.1).

In a microscopic approach, the orientational distribution of the mesogens around the director \hat{n} can be used to determine the amount of order. In general, assuming a rigid molecule, it is a function of the three Euler angles with respect to \hat{n} . An illustration is shown in Fig. 1.2 b. Due to the uniaxial symmetry of the nematic

phase, the rotation φ around \hat{n} can be disregarded. Furthermore, rigid cylinders, spherocylinders or prolate spheroids with cylindrical symmetry are often a good approximation for the shape of the elongated molecules. Hence, the rotation angle ψ can also be ignored. As a consequence, the distribution function is only dependent on γ . In this case, the projection on \hat{n} can be used to identify a numerical order parameter S . In three dimensional systems, it is defined as

$$S = \frac{1}{2} \langle 3 \cos^2 \gamma - 1 \rangle, \quad (1.1)$$

where the brackets denote the statistical average. An order parameter of $S = 0$ characterizes the isotropic phase, where $\langle \cos^2 \gamma \rangle = \frac{1}{3}$; $S = 1$ represents the case of perfectly aligned molecules, where γ is always zero (de Jeu, 1980). More general and essential for the case of asymmetric molecules, a tensorial order parameter can be determined, which is a generalization of Eq. (1.1). It is a real, symmetric and traceless tensor, obtained from the angular distribution of mesogens. The tensor is always diagonalizable and its largest eigenvalue is also referred to as the uniaxial order parameter S . Moreover, the normalized eigenvector of the largest eigenvalue can be identified with the nematic director \hat{n} (de Gennes & Prost, 2006).

In practice, for molecular systems, the angular distribution function $h(\gamma)$ cannot be determined experimentally. However, the order parameter S is directly linked to measurable quantities like the diamagnetic or optical anisotropy. For typical nematic liquid crystals, S is in the order of 0.3 to 0.8 and decreases with rising temperature (Chandrasekhar, 1994).

In contrast to molecular systems, experiments with macroscopic particles often reveal the exact position and orientation of each individual particle, offering the angular distribution $h(\gamma)$. In this case, a direct calculation of S given $h(\gamma)$ is possible. An example of such a system can be found in the third publication (see section 2.3), where a monolayer of granular rod-like particles was investigated. In this paper, the uniaxial order parameter was used in its two-dimensional form, $S = \langle 2 \cos^2 \gamma - 1 \rangle$, to identify the amount of order. Additional details on the granular system will be discussed in section 1.3.2 of this thesis.

Dielectric properties of nematics

Typical organic liquid crystals, like pure 5CB, have a very low conductivity and are therefore often assumed to be perfect insulators. In general, the application of an external electric field \vec{E} leads to a dielectric displacement

$$\vec{D} = \epsilon_0 \epsilon \vec{E} \quad (1.2)$$

within the dielectric medium, where the static relative permittivity ϵ is a tensor of second rank, dependent on the director \hat{n} (note that all equations in this work are based on the SI-units system). Due to the symmetry of the uniaxial nematic phase, Eq. (1.2) can be simplified to

$$\vec{D} = \epsilon_0 [\epsilon_{\perp} \vec{E} + (\epsilon_{\parallel} - \epsilon_{\perp}) (\hat{n} \cdot \vec{E}) \hat{n}]. \quad (1.3)$$

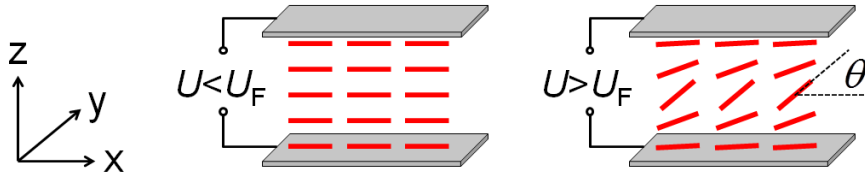


Figure 1.3: Illustrative sketch of the director (red dashes) between the conducting plates of the liquid crystal cell. For an undercritical voltage ($U < U_F$), the planar configuration parallel to the x -axis is stable. Above the Fréedericksz threshold ($U > U_F$) a rotation $\theta(z)$ of the director within the x - z -plane sets in, as $\epsilon_a > 0$.

The two dielectric constants ϵ_{\parallel} and ϵ_{\perp} are scalars and distinguish between an external electric field that is oriented parallel or perpendicular to the nematic axis, respectively (de Gennes & Prost, 2006). Thus, depending on the sign of dielectric anisotropy $\epsilon_a = \epsilon_{\parallel} - \epsilon_{\perp}$, the director \hat{n} will tend to orientate parallel ($\epsilon_a > 0$) or perpendicular ($\epsilon_a < 0$) to \vec{E} .

Consider the nematic liquid crystal 5CB with an initial planar configuration along the x -direction, like in the test cell described above (see Fig. 1.2 a). 5CB has a positive dielectric anisotropy, $\epsilon_a > 0$. Thus, the application of a sufficiently strong external electric field perpendicular to the nematic axis will induce a reorientation of the director. In an idealized model, which is valid in many cases, only elastic and dielectric torques are taken into account and strong anchoring at the boundary is assumed. For weak electric fields, the stabilizing elastic torque is larger than the dielectric torque and small fluctuations of the director are damped. But, above a critical strength, the undisturbed configuration becomes unstable and small fluctuations result in a deformation of the director field (de Jeu, 1980).

This so called Fréedericksz transition is named after the Russian physicist Vsevolod Fréedericksz, who was one of the first to study electro-optical effects in liquid crystals. It was initially observed for the application of magnetic fields. Indeed, its description can be easily converted between the magnetic and the electric case, considering the anisotropic magnetic susceptibility instead of the dielectric anisotropy. However, this work will concentrate on purely dielectric effects.

The critical electric field is dependent on the dielectric anisotropy ϵ_a , the layer thickness d and the elasticity of the system. For uniaxial nematics, a deformation of the director field can be described by three basic distortions: splay, twist and bend. They are characterized by three elastic constants, namely k_{11} , k_{22} and k_{33} , respectively. For an initially planar orientation of the director (parallel to the x -axis) and a perpendicular electrical field (parallel to the z -axis), only a polar rotation of the mesogens (within the x - z -plane) can be induced, described by a tilt angle θ (see Fig. 1.3 for a sketch). Thus, only the splay elastic constant k_{11} is relevant and the

critical Fréedericksz threshold voltage is found as (Blinov & Chigrinov, 1996)

$$U_F = \pi \sqrt{\frac{k_{11}}{\epsilon_0 |\epsilon_a|}}. \quad (1.4)$$

Figure 1.3 shows a sketch of the director for voltages below and above U_F . Due to symmetry reasons, both clockwise and counterclockwise rotations θ of the director are equivalent. Thus, at the critical voltage, the stability diagram bifurcates into two equivalent stable states.

The dielectric anisotropy ϵ_a can be measured experimentally. This was done for the liquid crystalline substances of the first publication (see section 2.1). For that purpose, the test cell is used as a plane capacitor and connected in series with an ohmic shunt resistor. An AC voltage is applied in order to prevent the liquid crystal from electro-chemical reactions that would possibly occur with DC. The frequency is chosen sufficiently low (e.g., 1 kHz) to essentially determine the static permittivities of the liquid crystal (de Jeu, 1980). The complex voltage drops can be measured at the cell and the ohmic resistor, using a lock-in technique. Knowing the exact resistance of the shunt, the complex conductivity and consequently the capacity of the cell can be determined.

At sufficiently small voltages below the Fréedericksz transition, the planar configuration is preserved ($\vec{E} \perp \hat{n}$) and the measurement reveals the capacity C_\perp . At very high voltages, the director in the bulk is expected to be rotated by 90 degrees ($\vec{E} \parallel \hat{n}$). Although the strong anchoring at the boundary prevents the whole liquid crystal layer from a perfect homeotropic alignment, an extrapolation to infinitely strong electric fields yields a good approximation of C_\parallel . Consequently, with the capacity C_0 of the empty cell, the dielectric anisotropy can be calculated as $\epsilon_a = (C_\parallel - C_\perp)/C_0$.

Optical properties of nematics

Due to the anisotropic nature of nematics, the refractive index is anisotropic, too. Thus, similar to several solids with asymmetric crystal structures, birefringence can be observed in the uniaxial nematic mesophase. Reminiscent to the description of the dielectric anisotropy, the optical properties of nematics are represented by two scalars. The refractive indices n_\perp and n_\parallel correspond to light with a linear polarization perpendicular or parallel to the optical axis, respectively. In the case of 5CB, this optical axis corresponds to the elongated axis of the rod-like molecules, described by the director \hat{n} .

In all experiments discussed in this thesis, the incident light is oriented along the z -direction, normal to the plane of the substrate (see also section 2.1). The transmitted light is split into an ordinary and an extraordinary part, described by the refractive indices n_o and n_e . As already mentioned above, the application of a sufficiently large external electric field along the z -axis does only induce a tilt $\theta(z)$ of the director field within the x - z -plane (see Fig. 1.3). Thus, the percentage of light with linear polarization perpendicular to the optical axis is constant and $n_o = n_\perp$. In

contrast, the rotation $\theta(z)$ of the mesogens strongly influences the amount of parallel polarization with respect to the optical axis. As a result, the refractive index of the extraordinary light ray is written as

$$n_e[\theta(z)] = \frac{n_\perp n_\parallel}{\sqrt{n_\perp^2 \cos^2 \theta(z) + n_\parallel^2 \sin^2 \theta(z)}}. \quad (1.5)$$

It varies between n_\parallel for a planar alignment with $\theta = 0$, and n_\perp for the perfectly homeotropic case with $\theta = \pi/2$. Reflecting the difference between n_o and n_e , the ordinary and the extraordinary ray are passing the medium with different velocities, yielding a phase difference of

$$\delta = \frac{2\pi}{\lambda} \int_0^d (n_e[\theta(z)] - n_o) dz, \quad (1.6)$$

where λ is the wavelength of the light and d the thickness of the nematic layer. In order to identify δ , the nematic layer is typically sandwiched between crossed linear polarizers. In this configuration, the intensity of the transmitted light is described by

$$I = I_0 \sin^2(2\phi) \sin^2 \frac{\delta}{2}, \quad (1.7)$$

where ϕ denotes the fixed azimuthal angle between the crossed polarizers and the projection of the director into the x - y -plane. Usually, ϕ is set to 45° to ensure the best dynamic range.

Equation (1.7) demonstrates that optical polarizing microscopy is a useful tool to determine variations of the director field. Dependent on the change of $\theta(z)$, the phase difference δ also changes and thus, a variation of transmitted intensity of light can be detected. Director deformations within a nematic layer can be generated electrically due to the Fréedericksz effect. But, also mechanically induced variations of θ are possible, for example by shearing the sample or by embedding colloids with certain boundary conditions (see section 1.2.3). Further details on the birefringence method can be found in the first publication (section 2.1).

1.2.2 Functionalized block copolymers in nematic liquid crystals

Mesomorphic properties can be incorporated into macromolecular systems by the synthesis of liquid crystalline polymers. They are classified by their characteristic phase behavior and their molecular structure. On the one side, main-chain liquid crystalline polymers can be produced by attaching monomer mesogenic units to each other. The polymers can form a liquid crystalline state if the rigidity of the monomers and the connection unit is chosen appropriately, the geometrical anisotropy of the polymer is sufficiently large and internal rotations are strongly restricted (Ciferri, 1991).

In the case of a thermotropic polymeric liquid crystal, the polymer itself can exhibit the mesomorphic state between the glass transition and the clearing temperature.

However, pure systems of rigid polymer chains often feature a reduced solubility and a melting temperature that is too high to generate a chemically stable mesophase (Khoo & Simoni, 1991). For such substances, an appropriate solvent can be used to generate the mesomorphic state, making the system lyotropic. The variation of the length to diameter ratio of the polymer chain can strongly influence the critical concentration for the development of the mesophase (Hermans, 1962). Macroscopic similarities were found in a granular system that will be discussed in section 1.3.2 and was the subject of investigations in the third publication (section 2.3).

In addition to main-chain polymers, the synthesis of liquid crystalline side-chain polymers is also possible, where mesogenic units are connected to conventional polymer chains. Both, the flexibility and the length of the spacer between the backbone of the polymer and the attached mesogen have a strong impact on the mechanical properties. Hence, the side-chain polymers can be used to tune the properties of organic molecular liquid crystals. Adapted to and mixed within a low molecular weight liquid crystal, physical parameters like the viscosity of the host can be influenced dramatically (Khoo & Simoni, 1991).

In the first publication (section 2.1), a binary mixture of the low molecular weight liquid crystal 5CB and a mesogenic side-chain ABA-triblock copolymer was investigated. The polymer was functionalized such that the middle block contained moieties that were structurally similar to 5CB. The cyanobiphenyl moieties were attached to the backbone via flexible alkyl spacers. As a consequence, the middle block was soluble both in the isotropic and in the nematic state of the host. In contrast, the polystyrene end blocks of the copolymer were not adapted. Thus, they were expected to be only soluble in the isotropic state of 5CB and to associate in the nematic state due to microphase separation.

At high concentrations of polymer, a gelified state could be observed, as the end blocks of the block copolymer formed the nodes of a physical network. Below the gelation concentration, the dilute solutions revealed a behavior similar to usual nematics. Consequently, a typical planar arrangement of the director appeared after filling the low concentrated mixtures into the conventional test cells. The order of the mesogenic side-chains is almost independent of the conformation of the polymer chain, which makes them adaptable to low molecular weight mesogens (Khoo & Simoni, 1991). However, the viscoelastic properties of the host may be strongly influenced by the polymer. The effect of concentration was investigated in the first publication (section 2.1) and will be briefly outlined in the following.

Influence of the polymer on the properties of the nematic host

In principle, the Fréedericksz threshold U_F of a homogeneous mixture of 5CB with a small amount of liquid crystalline polymer can be determined with a polarizing microscope using the quasi-static birefringence technique. Starting from a subcritical voltage and increasing the voltage in small steps, the onset of an intensity variation, induced by a rotation of the director field, displays the threshold. However, such a quasi-static experiment was not suitable for the investigation of the block copolymer

mixtures, as the response times to an electric field were dramatically longer compared to pure 5CB (see section 2.1). Thus, a strong increase of waiting times between the single voltage steps would have been necessary for a proper determination of U_F . Consequently, dynamical measurements were performed in order to determine U_F and other material parameters.

In the dynamical measurements the voltage was switched between zero and a slightly overcritical value and the temporal development of the intensity variation was recorded. From that, the corresponding development of the phase difference $\delta(t)$ between the ordinary and the extraordinary ray was extracted using Eq. (1.7). This led to characteristic time constants τ_{on} and τ_{off} for the sudden voltage increase and decrease, respectively. With the knowledge of the layer thickness d and the dielectric anisotropy ϵ_a of the nematic mixture, a proper and fast determination of the Fréedericksz threshold U_F and the rotational viscosity γ_1 was possible.

For mixtures with block copolymer mass concentrations c of up to 2.5%, the Fréedericksz threshold U_F was found to remain essentially the same as for pure 5CB. Furthermore, measurements of the dielectric anisotropy ϵ_a , as described in section 1.2.1, showed a large scattering that was probably caused by the strong dependency of the permittivity on impurities of the liquid crystalline material (Bogi & Faetti, 2001). However, no explicit dependency of ϵ_a on c could be found. As a consequence, the splay elastic constant k_{11} , which is only dependent on U_F and ϵ_a , did not exhibit a dependency on the addition of a low amount of block copolymer, either. In contrast, the rotational viscosity γ_1 was found to increase strongly with increasing polymer concentration.

In addition to the block copolymer, corresponding side-chain homopolymers were investigated, where the polymer was only consisting of the 5CB-functionalized middle blocks. Due to the lack of polystyrene end blocks, no self-assembly of polymer chains and no gelation at high concentrations was expected in these homopolymer systems. The material parameters U_F and ϵ_a revealed similar results compared to the block copolymer system, which means no significant dependency on c . Besides, in the homopolymer mixtures, γ_1 was increasing with c , too. But, for the highest investigated concentration, this increase was about a factor of 50 less pronounced than for the mixtures with block copolymer.

The Brochard theory (Brochard, 1979) for the dynamics of independent polymer chains in a nematic solvent (diluted solution) was used to discuss the increase of the rotational viscosity $\delta\gamma_1$. In the theory, $\delta\gamma_1$ is given by the number of monomers per unit volume, the degree of polymerization, the rotational relaxation time of the polymer and the dimensions of the individual polymer chains parallel and perpendicular to the director. The model predicts a linear increase of $\delta\gamma_1$ with increasing polymer concentration as long as the polymer chains have an anisotropic shape. Indeed, an almost linear dependency of $\delta\gamma_1$ on c was found for the homopolymer mixtures. With an estimation of the aspect ratio of the polymer, this yielded an estimation of the rotational relaxation time of the homopolymer chains. In the small concentration range ($c < 1\%$) the increase of $\delta\gamma_1$ was similar for both the block copolymer and the homopolymer. However, at higher concentrations, the block copolymer mixtures

exhibited a strong deviation from a linear dependency. This was attributed to the formation and growth of larger chains or clusters, enforced by the polystyrene end blocks.

The comparison of $\delta\gamma_1$ for block copolymer and homopolymer solutions yielded an estimation of the effective cluster size of the self-assembled block copolymer chain segments and of the critical concentration c_{gel} for the sol-gel transition. The estimation of $c_{\text{gel}} = 2.7\%$ was very close to the value of 3.0% which has been determined by rheological measurements. Thus, the dynamic electro-optical measurements of the rotational viscosity manifested an alternative approach for the determination of the critical concentration. Furthermore it could be used to detect and characterize the aggregation of the end blocks and the shape anisotropy of the clusters.

Aging effects

Physical aging is an undesirable effect in many synthetic materials. For example, in solid polymers the thermodynamically stable state is slowly recovered by spontaneous densification of the structure, resulting in a time dependent change of physical properties (Cangialosi *et al.*, 2013). Keeping the above described low concentrated mesogenic side-chain polymer mixtures in the nematic state, they also showed a dramatic change of the electro-optical response. Several months after filling the substances into the test cells, the response times τ_{on} and τ_{off} exhibited a significant decline. Consequently, the rotational viscosity γ_1 was also decreasing strongly, whereas U_F and k_{11} were again not affected.

Figure 1.4 reveals a comparison of γ_1 when measured shortly after filling the material into the test cell and half a year after that. The former values correspond to the data that are also published in the first article (section 2.1). It is obvious that for both block copolymer and homopolymer mixtures, γ_1 is significantly lower after the waiting time of several months. For block copolymer mixtures of high concentrations, γ_1 still exceeds the corresponding value of the homopolymer. But, while the values of block copolymer and homopolymer coincide up to $c \approx 1\%$ for measurements performed immediately after the preparation, this range extends up to $c \approx 2\%$ for the later investigations.

It is also remarkable, that the electro-optical measurements could be performed on the mixture with 4% of block copolymer. According to the previous findings, at this concentration a gelified state is expected (see section 1.2.4). Indeed, no homogeneous alignment of the director has been observed immediately after the filling procedure. At the early stage, such a polydomain structure indicated the presence of a gelified state. However, six months later the sample was well aligned and measurements revealed γ_1 in the range of samples with $c = 2\%$ half a year before.

Different chemical reactivities of the blocks and different solubilities in the solvent have been found to influence the adsorption of block copolymers on metallic surfaces (Hershkovits *et al.*, 2008). Thus, the decay of the rotational viscosity in our samples might be attributed to adsorption effects at the inner surface of the test cells. This adsorption could lead to a reduction of the effective concentration in the bulk and

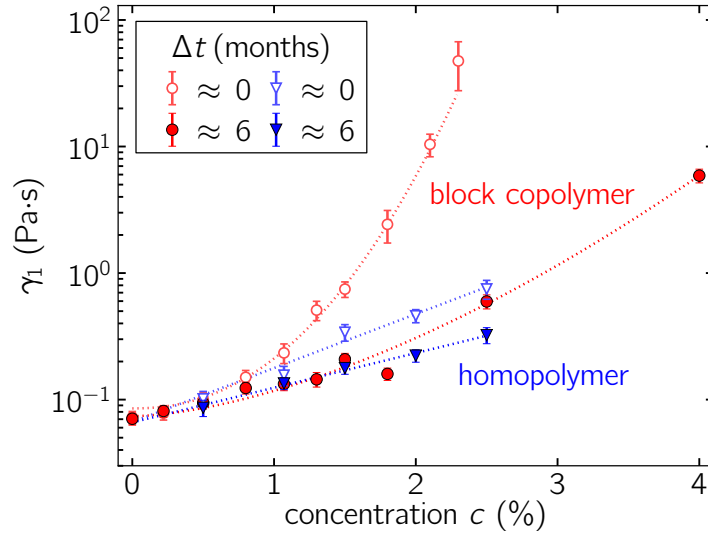


Figure 1.4: Rotational viscosity γ_1 for mixtures of 5CB with a concentration c of block copolymer (red) or homopolymer (blue). Open symbols show the data measured a few hours after filling the test cells (values of section 2.1). Closed symbols are measurements of the same cells approximately six months later. The dotted lines are a guide to the eye.

consequently to a decrease of the response times of the director. Indeed, scaling the concentration of the later measurements with a factor of 0.55 results in an agreement of γ_1 between both datasets and indicates a reduction of the effective concentration in the bulk of about 45%.

Examples of the temporal development of $\gamma_1(t)$ for concentrations of $c = 1.0\%$ and 1.5% of block copolymer and homopolymer are shown in Fig. 1.5. Within one year, all mixtures exhibit a strong decrease of γ_1 to a relatively low value that is near the rotational viscosity of the neat nematic host ($\gamma_1^{5\text{CB}} = 0.08 \text{ Pa}\cdot\text{s}$). The decline can be approximated by an exponential decay

$$\gamma_1(t) = \Delta\gamma_1 \cdot \exp\left(-\frac{t}{\tau}\right) + \gamma_{1,\infty}, \quad (1.8)$$

where $\Delta\gamma_1$ specifies the total decrease and $\gamma_{1,\infty}$ describes the limit for infinitely long waiting times. Note that except for the block copolymer mixture with $c = 1\%$, the initial values $\gamma_1(0)$ are all below the ones described in the first publication. Furthermore, for a concentration of $c = 1\%$ of block copolymer, $\gamma_1(0)$ exceeds the value of the corresponding homopolymer mixture. This is also in contradiction to the above described equality of block copolymer and homopolymer samples for $c \leq 1\%$.

The quantitative discrepancy might arise from the re-preparation of the mixtures. The polymer was anew dissolved in 5CB before performing the longtime measurements

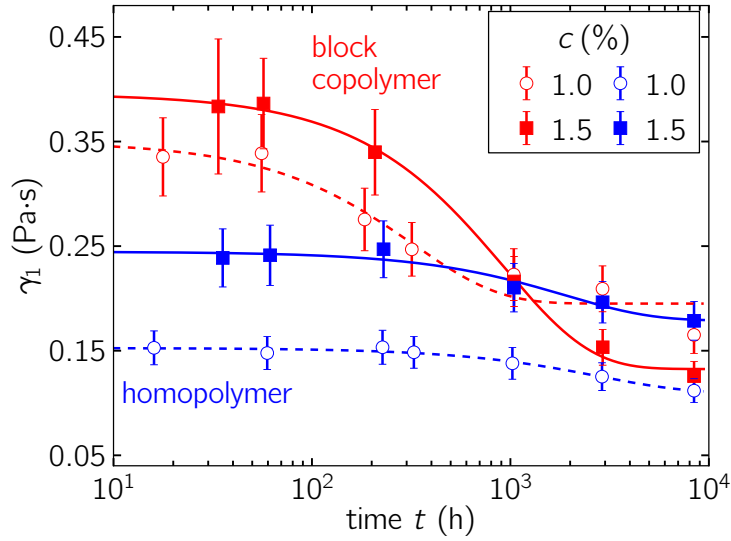


Figure 1.5: Temporal decrease of the rotational viscosity γ_1 for dilute solutions of functionalized polymer in 5CB. The red (blue) data points correspond to mixtures with block copolymer (homopolymer) of concentration c . The dashed (solid) lines are exponential fits corresponding to the open (closed) symbols.

presented in Fig. 1.5. Aging effects in the undissolved polymer could already have taken place during a time span of several months between the synthesis and the dissolution in 5CB. Some of the samples featured strong inhomogeneities after filling them into the test cells by means of big polymer aggregates in the size of several microns. Although expected to be soluble in both isotropic and nematic state of the solvent, even the homopolymer exhibited such local impurities. Size-exclusion chromatography indicated that parts of the polymer are shifted to a higher molecular weight, indicating a reaction of the side groups in addition to the adsorption effects described above.

Due to the strong inhomogeneities in the cell, an accurate quantitative measurement of $\gamma_1(0)$ is not guaranteed anymore. Nevertheless, the qualitative decrease of γ_1 as shown in Fig. 1.5 and also in Fig. 1.4 is obviously a dramatic effect which has to be kept in mind when dealing with liquid crystalline polymeric systems.

1.2.3 Director defects in a mixture of a block copolymer and a nematic liquid crystal

When colloidal particles are suspended in a nematic solvent, local director disturbances can occur. As an example, spherical particles, like water droplets or gas bubbles injected into a nematic liquid crystal host, have already been investigated intensively (Stark, 2001). In general, the director field in the surrounding of the bounding surface depends on the relative strength of elastic forces, the strength of the interfacial

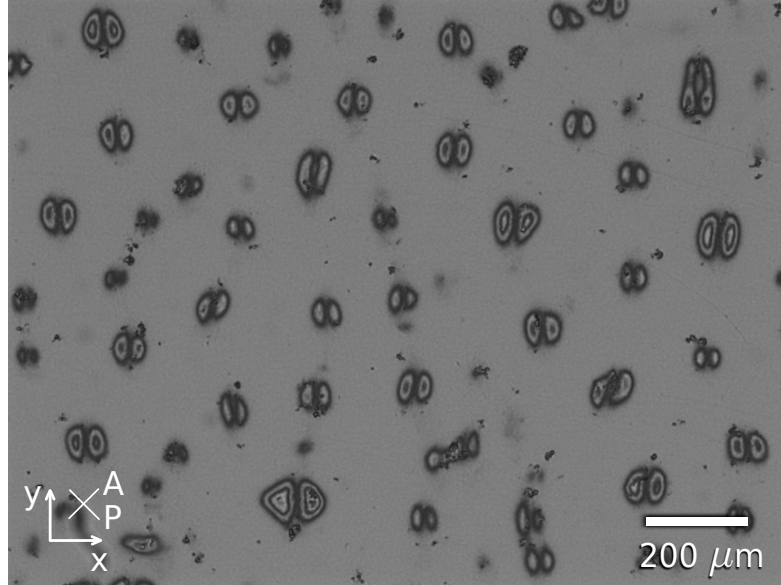


Figure 1.6: Typical snapshot of the director defects in a liquid crystalline block copolymer mixture of concentration $c = 1.5\%$, at a temperature of $T = 25^\circ\text{C}$. The sample is mounted between crossed polarizers and illuminated with monochromatic light. Polarizer (P) and analyzer (A) are oriented at an angle of $\phi = 45^\circ$ with respect to the main director that is preferably aligned along the x -axis.

interaction and an optionally applied external electric or magnetic field (Kralj & Žumer, 1992).

There are two basic possibilities of the director anchoring at the surface of the colloid. On the one side, the colloid might induce a normal anchoring, where the director is aligned perpendicular to its surface. When such a colloid is embedded into a uniformly aligned nematic host, depending on the size of the colloid, a dipolar director configuration with a hyperbolic hedgehog or a quadrupolar Saturn-ring configuration can be observed (Völtz *et al.*, 2006). On the other side, also planar anchoring can be induced by modifying the surface of the particle, for example by adding polyvinyl alcohol to the water phase of droplets (Poulin & Weitz, 1998). If such a colloid is embedded in a homogeneously aligned nematic host, the director of the liquid crystal will continuously adapt tangential to the surface except for two surface defects.

The aggregation of mesogenic side-chain block copolymers into big clusters is an alternative method to induce such a colloid-like behavior in a nematic host. New mixtures of the block copolymer samples described above were generated by performing the polymer analogous reaction from the polystyrene-block-poly(4-hydroxystyrene)-block-polystyrene backbone to a cyanobiphenyl-functionalized block copolymer once again (details on the synthesis can be found in section 2.2). Due to the new synthesis,

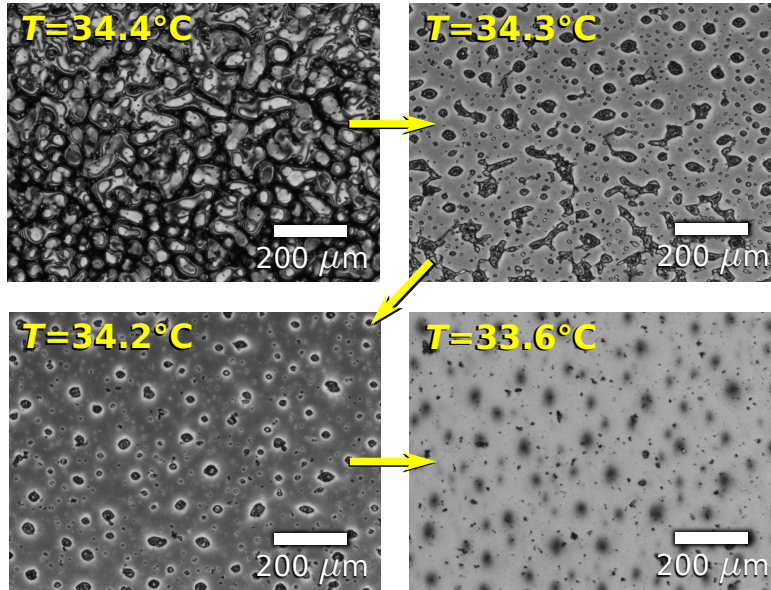


Figure 1.7: Typical snapshots (sample between crossed polarizers) of the formation of director defects when cooling with a relatively low speed of $dT/dt = -0.05$ K/min. The nematic-isotropic transition takes place at $T_{NI} \approx 35$ °C. Above T_{NI} , the isotropic phase between crossed polarizers yields black images. Further cooling to room temperature leads to structures as illustrated in Fig. 1.6.

differences in the degree of conversion and the solubility of the polymer are possible compared to the mixtures described so far. After the standard filling procedure of the test cells (see section 2.1 for further details), optical polarizing microscopy uncovered regular patterns instead of a completely uniform state for the sample with $c = 1.5$ % of the new synthesized block copolymer.

Figure 1.6 shows a typical snapshot of such a cell ($d \approx 25$ μm), mounted between crossed polarizers ($\phi = 45^\circ$) and illuminated with monochromatic light. While the homogeneous gray background illustrates a planar alignment of the director parallel to the x -axis, as induced by the preparation of the cell, well distributed structures of an oval to kidney-like shape indicate locally strong disturbances of the director field, which might be caused by big aggregates of nonsoluble block copolymer. Most of the structures have a symmetry axis along the y -direction that is perpendicular to the main orientation of the undisturbed director.

Dependency on thermal treatment

A variation of the thermal treatment revealed a strong influence on the formation of the structures. Figure 1.7 demonstrates the occurrence of microphase separation during a cooling process from the isotropic to the nematic range at a moderate cooling

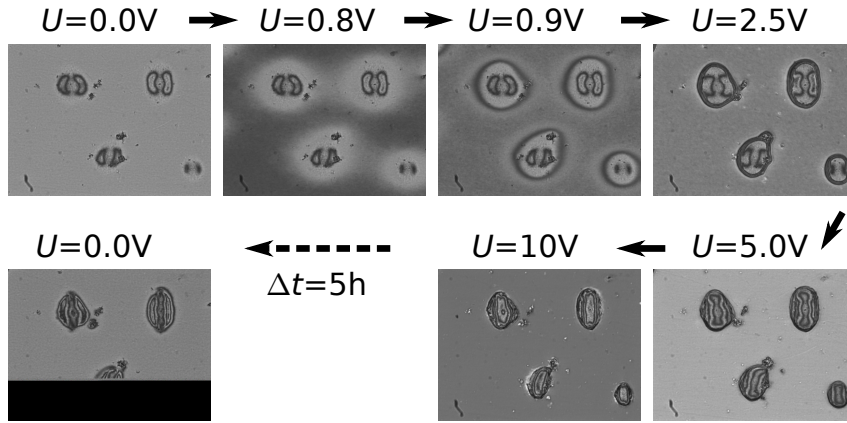


Figure 1.8: Snapshots (sample between crossed polarizers) of the director defects during increasing voltage U . Note that the critical Fréedericksz voltage for pure 5CB is $U_F = 0.73$ V. Even several hours after switching off the voltage, the initial structure of the defect does not reappear.

rate of $dT/dt = -0.05$ K/min. If the cooling speed was chosen too fast, the formation of regular shaped patterns could not be observed. Instead, irregular shaped defects were visible when reaching ambient temperature.

Such a dependency on the cooling rate can be compared to experiments performed by Roth *et al.* (2010), where the gelation of a suspension of poly(methyl methacrylate) colloids in 5CB was investigated during the isotropic-nematic phase transition. With decreasing cooling rate, Roth *et al.* (2010) observed an increase of size of nematic droplets between a network that was formed by the colloidal particles. This is similar to the findings in our block copolymer mixtures, where a low cooling rate also leads to the formation of bigger domains of homogeneously aligned 5CB. When cooling slowly, small domains of 5CB have more time to coalesce into bigger ones forcing the compression and aggregation of the polymer. Strong interaction between the neat liquid crystal and the mesogenic side-chains of the polymer aggregate leads to the final director configuration with minimized free energy.

Electro-optical response

As discussed above, the application of an overcritical electric field along the z -axis causes a director deformation in an initially planar nematic liquid crystal (Fréedericksz effect). Figure 1.8 shows the intensity distribution around the colloids at different voltages. Below the Fréedericksz transition, $U < U_F$, the initial configuration is stable. Above U_F , the director changes its orientation resulting in an intensity variation around the defects (see Fig. 1.8 at 0.8 V). However, at relatively low voltages above U_F , there is no intensity variation in the near proximity of the defects. This indicates

a strong anchoring of the director on the surface of the colloid. With further increase of the voltage, the boundary between the undistorted and the distorted region tightens towards the defect until the kidney-like shape is getting destroyed (see Fig. 1.8 at 5 V and 10 V).

After switching off the voltage, outside of the defects the initial gray level degenerates very quickly, indicating that the main part of the director reorients back to the planar state. In contrast, the initial director configuration around the colloid does not reappear completely, even after waiting times of several hours (see lower left image in Fig. 1.8). Possibly, a reformation of the polymer chains and the director field might occur on much larger timescales. However, the kidney-shaped structures can be regenerated by heating the sample above T_{NI} and slowly cooling down again.

Empirical description of the director distribution

It has been shown that liquid crystalline side-chain polymers with a sufficiently large degree of polymerization form an oblate configuration in a planar nematic host. The symmetry axis of this oblate object is expected to be parallel to the director (Kempe *et al.*, 2004). Thus, as a raw approximation, the director defect generating aggregate of polymer can be modeled by an ellipsoid-like shape.

Due to their nonsolubility in the nematic phase, the end blocks of the block copolymer are assumed to build the core of the agglomeration, whereas the middle blocks with the attached mesogens are expected to be preferably on the surface. In addition, due to a relatively short spacer length between backbone and mesogen, a normal director orientation on the surface of the agglomerate is assumed. Furthermore, the agglomerate is expected to be penetrated by the liquid crystal, thus the director field will be considered for the inner and the outer region. Crossed polarizers with orientation along the x - and the y -direction ($\phi = 0^\circ$ instead of $\phi = 45^\circ$) did not demonstrate any spatial intensity variation. Therefore, a strong azimuthal rotation of the director (twist) within the x - y -plane can be excluded.

The three-dimensional director field is constructed iteratively along the y -direction (see Fig. 1.9 a). At $y = 0$, the boundary of the colloid is assumed to have the shape of an ellipse with half axis of length a in the x -direction and c in the z -direction (see Fig. 1.9 b). In experimental observations, the positions of the defects were found to be very stable, leading to the assumption that the polymer agglomerations have a strong connection to the upper and the lower boundary of the cell. Thus, we use truncated ellipses, implying that the distance d between upper and lower boundary of the liquid crystal layer is smaller than $2c$. In the x - z -plane, the two-dimensional analytical form of the ellipse is described by $f(x) = \pm c\sqrt{1 - \frac{x^2}{a^2}}$, with positive and negative sign for $z > 0$ and $z < 0$, respectively.

With increasing distance from the center ($y \neq 0$) the short half axis of the ellipse is assumed to decrease iteratively until it reaches zero at $y = \pm b$. In contrast, the long half axis is assumed to be independent of y . This yields a three-dimensional

description of the whole surface as

$$f(x, y) = \pm c \sqrt{1 - \frac{x^2}{\left(a\sqrt{1 - \frac{y^2}{b^2}}\right)^2}}. \quad (1.9)$$

Assuming that the director is normal to the surface of the single ellipses and that there is no rotation in the x - y -plane, the director field in the outer region of the agglomerate is then described by its rotation angle of

$$\theta_{\text{out}}(x, y) = \arctan\left(\frac{\partial f(x, y)}{\partial x}\right) + \frac{\pi}{2}, \quad \text{for } x < 0, \quad (1.10)$$

$$\theta_{\text{out}}(x, y) = \arctan\left(\frac{\partial f(x, y)}{\partial x}\right) - \frac{\pi}{2}, \quad \text{for } x > 0, \quad (1.11)$$

whith the first derivative

$$\frac{\partial f(x, y)}{\partial x} = \mp \frac{xc}{\sqrt{1 - \frac{x^2}{\left(a\sqrt{1 - \frac{y^2}{b^2}}\right)^2}} \cdot \left(a\sqrt{1 - \frac{y^2}{b^2}}\right)^2}. \quad (1.12)$$

The inner part is constructed such that the director is continuously reorienting back towards a planar alignment. The deflection from this planar orientation is supposed to be maximum at the surface of the colloid, without any discontinuity to θ_{out} , and to be zero at $x = 0$ and $z = 0$. This can be guaranteed by the factor $\frac{|x|}{a\sqrt{1 - \frac{y^2}{b^2}}} \cdot \frac{z}{f(x, y)}$ which leads to the director distribution of

$$\theta_{\text{in}}(x, y, z) = \frac{|x|}{a\sqrt{1 - \frac{y^2}{b^2}}} \cdot \frac{z}{f(x, y)} \cdot \theta_{\text{out}}(x, y) \quad (1.13)$$

in the inner part of the colloid (i.e., for $|z| < |f(x, y)|$).

Figure 1.10 illustrates the distribution of the director field, applying Eqs. (1.10), (1.11) and (1.13) with parameters $a = 20 \mu\text{m}$, $b = 15 \mu\text{m}$, $c = 18 \mu\text{m}$ and a cell height of $d = 26 \mu\text{m} < 2c$. The intensity is calculated by numerical integration of the phase difference δ according to Eqs. (1.5) - (1.6) and applying this to Eq. (1.7). The refractive indices $n_{\parallel} = 1.71$ and $n_{\perp} = 1.53$ were chosen according to the literature values for pure 5CB (Blinov & Chigrinov, 1996). The wavelength of light $\lambda = 637 \text{ nm}$ was used with respect to the experimental illumination. Although this model is only a raw approximation and does not take any anchoring strength into account, the comparison of Fig. 1.6 and Fig. 1.11 illustrates a qualitative agreement. This reinforces the idea of a penetrated block copolymer agglomerate and the uniform distortion of the director field.

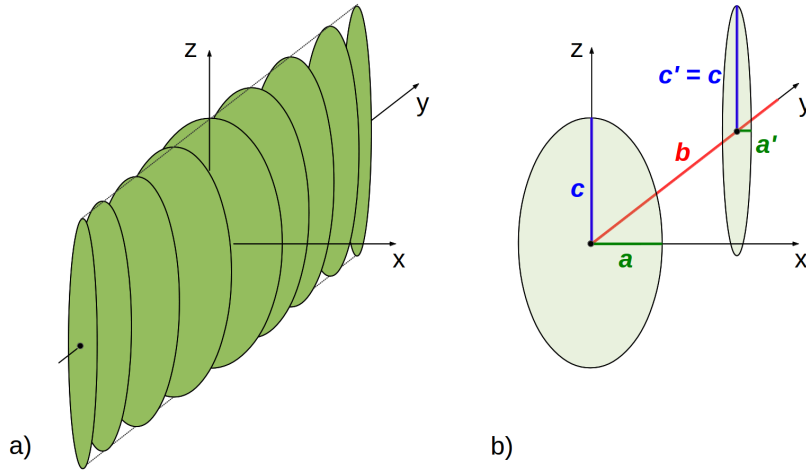


Figure 1.9: Sketch of the idealized shape of the director defect generating agglomeration of polymer. a) Illustration of the iterative construction along the y -direction via two-dimensional ellipses. b) Definition of the relevant parameters: The short axis a is decreasing along the positive and negative y -direction, while the long axis c is constant. The whole agglomerate is assumed to have a length of $2b$ along the y -direction.

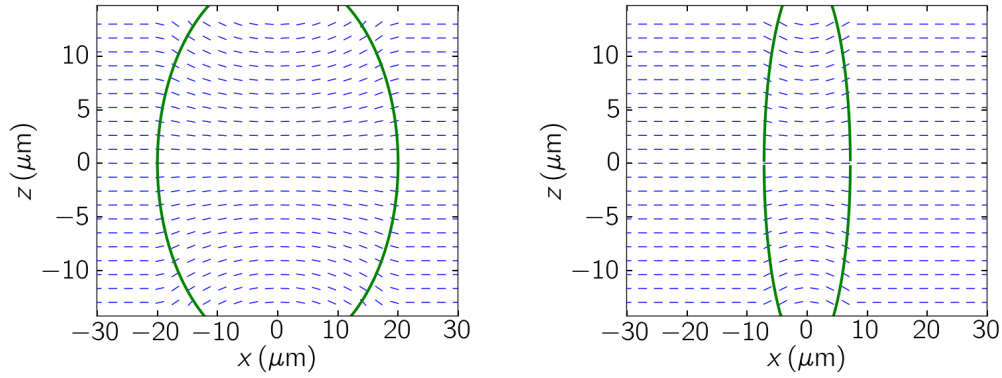


Figure 1.10: Theoretical distribution of the director according to Eqs. (1.10), (1.11) and (1.13) for parameters $a = 20 \mu\text{m}$, $b = 15 \mu\text{m}$, $c = 18 \mu\text{m}$ and a cell height of $d = 26 \mu\text{m}$. The green line indicates the surface of the agglomerate $f(x)$ while the blue dashes represent the director field. The left panel shows the distribution at $y = 0$, the right one corresponds to $y = \pm \frac{14}{15}b$.

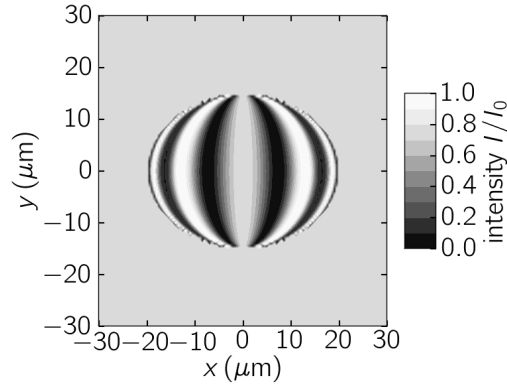


Figure 1.11: Theoretical intensity distribution according to the model described in the text. The intensity distribution is calculated by applying Eqs. (1.5) - (1.7) to the director distribution that is shown in Fig. 1.10 and described in the text.

1.2.4 Liquid crystalline gels

The occurrence of a gelified state in the here described liquid crystalline block copolymer system is strongly dependent on two parameters. First, it is influenced by the concentration c of block copolymer in the nematic host. Below a critical concentration c_{gel} the mixture can be regarded as a dilute solution. In the nematic state of 5CB the end blocks are aggregating because of their nonsolubility in the nematic host. Simultaneously, the soluble middle blocks are forming loops surrounding the aggregation core and leading to flower-like conformations of the polymer chains. However, as the concentration is low, the aggregates are expected to be only in the range of several chains and uniformly distributed over the whole sample. Hence, a strong influence on the parallel alignment of the director, like it was discussed in the section above, should not be visible by applying methods of optical polarizing microscopy. Indeed, for the investigations with $c < c_{\text{gel}}$ as described in the first publication (section 2.1), a planar alignment of the director was always fulfilled. With increasing concentration, the possibility of connections between single aggregates is also increasing. Consequently, the aggregation cores of the end blocks can form the nodes of a physical network, with the middle blocks acting as connections in-between.

Apart from the concentration of the polymer, the temperature is the second fundamental parameter, controlling the occurrence of the gelified state. In the isotropic phase of 5CB, the middle blocks as well as the end blocks are soluble and no aggregation should occur. When cooling the mixture and exceeding the isotropic-nematic transition of the solvent, a microphase separation of the now poorly soluble polystyrene end blocks sets in (Scruggs *et al.*, 2009). Accordingly, if the temperature of the system is too high, even for $c > c_{\text{gel}}$, the end blocks do not aggregate and no network forms.

Due to the thermal controllability of the gel state and the electro-optical response,

such thermoreversible liquid crystalline gels are a good example of functional soft materials. In the last decades, these systems have been investigated intensively. Their technical relevance can be found in devices like liquid crystalline semiconductors with high mobility or rewritable memories of bistable states (Kato *et al.*, 2007). One of the most prominent applications is the so called smart glass, a window that is switchable between a transparent and an opaque state. In such devices, tiny liquid crystal droplets are enclosed in a polymeric matrix and sandwiched between two conductive glass plates. Without any electric field, the orientation of mesogens in the single droplets are uncorrelated, leading to a strong scattering of incident light. Under the application of a sufficient voltage, the mesogens tend to align parallel due to their dielectric anisotropy, resulting in a shift of the substance into a transparent state (Mizoshita *et al.*, 2002).

In such smart glasses, the structure of the network has a strong influence on the contrast between the transparent and the opaque state (Mizoshita *et al.*, 2002). In addition, the response times are also an important feature that can be influenced by the properties of the network. Hence, in order to identify the optimal block copolymer gelator, the structure-property relations at $c > c_{\text{gel}}$ were studied in the second publication of this work (section 2.2).

In the investigations, the lengths of the middle block and the end blocks were varied by means of a variation of the repeating units. In temperature dependent rheological measurements, the temperature T_{gel} of the sol-gel transition was detected (section 2.2). For high temperatures, the storage modulus is lower than the loss modulus, being characteristic for liquids and indicating the isotropic state of the mixture. Lowering the temperature of the system, both moduli are increasing, although with different rate. Consequently, at the gelation temperature T_{gel} , a crossover between storage modulus and loss modulus is found. With further decrease of temperature, the storage modulus remains above the loss modulus, indicating the solid-like behavior of the gel state.

Although expected to coincide with the nematic-isotropic transition temperature T_{NI} of 5CB, the rheological measurements indicated a shift of T_{gel} to lower temperatures. Investigating various block lengths of the copolymer, the deviation $T_{\text{NI}} - T_{\text{gel}}$ was found to increase with decreasing length of the end blocks. As the existence of the biphasic region, where a nematic and an isotropic phase can coexist, is dependent on the molecular weight of the polystyrene (Ballauff, 1986), it is reasonable that shorter end blocks can lead to a smaller thermal range of the gelified state.

For the detection of the electro-optical response, the substances were filled into test cells, similar to the ones described in section 1.2.1. But in contrast to the regime with $c < c_{\text{gel}}$, a perfectly planar alignment of the mesogens did not emerge when reaching temperatures below T_{NI} . Instead, a polydomain structure has been observed, macroscopically appearing as an opaque state.

The positive dielectric anisotropy ϵ_a of 5CB forces the mesogens to realign parallel to an external electric field. Hence, the conversion between the opaque and the transparent state could be induced by the application of a sufficient electric field, oriented parallel to the direction of light. The magnitude of scattering was determined

with a photodetector by recording the transmittance of unpolarized monochromatic light. The transmitted intensity was low in the strong scattering opaque state and high in the transparent state.

When switching between an almost zero voltage U_{off} and a relatively high AC voltage of U_{on} , the temporal evolution of the transmitted light was measured. In general, for all investigated block lengths of the polymer, the transmission was found to be strongly dependent on the strength of the electric field. Increasing the values of U_{on} led to an increase of transparency. At high enough voltages, even transmission rates similar to the clear isotropic state were reached. In addition, switching to higher voltages yielded a faster response. Regarding the variation of block lengths, a longer middle block and a shorter end block were identified to reduce the required voltage U_{on} for a high transmitting state.

In the ideal case of a completely reversible process, switching back to U_{off} should lead to the degeneration of the initially opaque state. However, such a reversibility was found to be strongly dependent on the rigidity of the network (see section 2.2). In the gelified system, the rotation of the mesogens is always coupled with an elastic distortion of the polymer chains. But, if the physical crosslinks of the polystyrene end blocks are weak, strong electric fields can cause a rearrangement of the network structure and an adaption to an alignment of mesogens, persisting even after the release of the voltage.

In publication two (section 2.2), a fully reversible switching behavior with a relaxation back to the initial strong scattering state was only found for the block copolymer with the longest end blocks. The increased length of the end blocks presumably maintain stronger entanglements and result in stronger physical crosslinks. Furthermore, in experiments this type of block copolymer revealed the biggest thermal range of a gelified state, assigning it as a good candidate for electro-optical switching devices.

The investigations on the liquid crystalline gels illustrate the possibility of embedding mesomorphic materials into a polymeric network. However, the formation of the network strongly suppresses a global homogeneous alignment of the mesogens. Nevertheless, the tendency of uniaxial nematic alignment is still existent and can be found locally in small micron-sized domains. External electric fields or mechanical shearing can be used to convert such a polydomain into a monodomain state.

1.3 Granular Systems

Granular media are large accumulations of discrete particles where the single constituents are typically visible to the naked eye. With the size of the individual particles ranging on a macroscopic scale, they represent a classical example of a macroscopic system.

First investigations on granular media presumably have been executed far before Johannes Kepler, who formulated his conjecture about the closest packing of monodisperse spheres in the beginning of the 17th century (Hardie, 1966). Since Kepler's time, continuous explorations of granular matter have taken place and many famous scientists like Coulomb, Faraday or Reynolds have contributed to the understanding of the collective behavior of macroscopic particles.

However, in the second half of the 20th century, the amount of granular studies started to increase dramatically. It is the strong occurrence of granular constituents in automated industrial processes like food production, pharmaceutical technology, civil engineering or industrial farming that encouraged many engineers to investigate granular properties. Besides engineers, physicists have also raised their interest in granular matter in the last decades, as it reveals a system of unique static and dynamic properties (Hinrichsen & Wolf, 2004). Although much research has been done so far, granular matter is still far from being well understood. Even the simple problem of the packing of hard spheres, initiated by Kepler hundreds of years ago, still raises many open questions. As an example, a clear mathematical definition of random close packing, characterizing the maximum volume fraction for randomly packed particles, is still lacking (Torquato & Stillinger, 2010).

In contrast to microscopic, molecular systems, the influence of thermal energy can be neglected due to the size and mass of the single grains, even for the smallest granular particle size of hundreds of microns. Such an athermal nature of granular matter implies that external perturbations like vibration or shear are necessary to maintain the motion of grains and to modify a static granular configuration (Mehta, 2007). In contrast to the Brownian motion, which forces the mixing of the single components on a molecular scale, agitation does not necessarily induce a mixing of granular particles. Instead, the interacting particles exhibit unique phenomena like demixing, size segregation, pattern formation or convection (Ball, 2004; Knight *et al.*, 1996). In the case of such effects, it is crucial to consider the discreteness of the grains (Jaeger *et al.*, 1996).

The following sections will focus on two different aspects that are both relevant for a deeper understanding of the collective behavior of granular particles. In the first part, the effect of an elongated particle shape will be discussed. Reminiscent to mesophases in thermal liquid crystals, the ordering of cylindrical rods under external agitation will be described. Referring to the third publication of this thesis, which is reprinted in section 2.3 (Müller *et al.*, 2015), similarities and dissimilarities between thermal and athermal anisotropic systems will be shown. Concerning the dissimilarities, the second part of this chapter focuses on the dissipative effects that are ubiquitous in granular systems. Especially the influence of cohesive effects due to additional wetting

will be discussed. This was subject of the fourth publication that can be found in section 2.4 (Müller *et al.*, 2013b).

1.3.1 Anisotropic granular matter

In thermal systems, like the ones described in section 1.2, the anisotropic geometry of the molecules is a crucial ingredient for the development of a mesomorphic state. In a similar way, the shape of macroscopic grains does also play an important role for the collective behavior of granular media. Physical parameters like friction and the dissipation of energy during an impact are strongly dependent on the surface geometry and the texture of the single grains (Mehta, 2007). Experiments and theoretical studies are often performed with spherical particles. However, natural objects and industrial products illustrate the necessity for the inclusion of anisometric forms into granular studies. Rice, noodles, cereal grains, walnuts, pharmaceutical pills and wood dowels are only few examples of natural and engineered granular objects that feature an elongated shape. Because most of these materials have to be handled and packed in automated processes, the understanding of the physics behind their collective behavior is a strongly relevant task.

In the static case, a detailed investigation of the packing yields much information about structure, symmetries and various macroscopic physical properties of the bulk. In the case of elongated particles, the length to width ratio is known to be a crucial parameter that strongly influences the mechanical response of the granular conglomeration on stress (Börzsönyi & Stannarius, 2013). In particular, elongated objects have a preference to offer some kind of orientational order. On the one side, the order can be induced by the preparation of the system, for example due to a reorientation of the particles during flow. On the other side, the boundary of a container can also influence the arrangement of the single grains, like the matchbox induces an alignment of matches parallel to the wall (Buchalter & Bradley, 1992).

However, in less dense systems and with careful preparation, a random like packing of elongated particles is also feasible. Then, external energy input can be used to induce the reorganization into an ordered state. For example, Börzsönyi & Stannarius (2013) showed that shear can create the alignment of rod-like particles with initially random orientations. In contrast to molecules, ideal dry granular objects do not experience attractive forces like dipole-dipole interactions or van der Waals forces. Nevertheless, it was found that the shear alignment of the particles is comparable to simple molecular systems, even on a quantitative level. Similar to nematic liquid crystals, the alignment angle under shear was found to be independent on the shear rate (Börzsönyi *et al.*, 2012).

External vibration can also cause the reorganization of anisotropic granular particles. As an example, discrete vertical taps of granular rods lead to the development of orientational order and the compaction of the whole conglomerate (Villarruel *et al.*, 2000). Subjected to a sufficiently continuous mechanical agitation, a conglomeration of particles will change from its solid-like behavior at rest to a more fluidized state (Jaeger *et al.*, 1996). But, the coupling between the vibration source and the dynamics

of the granulate is very complex, as driving forces are not transmitted independently to individual particles. Instead, collective structural reorganizations are stimulated over the length scale of many particles (Mehta & Barker, 1994). Moreover, an elongation of particles introduces additional features into such complex nonequilibrium systems.

1.3.2 Driven monolayers of granular rods

The collective behavior of a three-dimensional system of rod-like particles under continuous vertical agitation was recently studied by Yadav *et al.* (2013). In their system, a formation of domains with horizontal and vertical alignment of the rods was observed. With increasing aspect ratio of the particles, even a predominantly vertical alignment was demonstrated. The strong influence of the aspect ratio on the ordering of granular rods was also shown in quasi-two-dimensional investigations by Narayan *et al.* (2006). In vertically driven horizontal monolayers, uniaxial nematic, smectic and even tetratic correlations with fourfold rotational symmetry were found. Moreover, a strong impact of the detailed shape of the cylindrical particles was traced in these two-dimensional experiments. Thus, rice grains with rounded tails and strictly circular cylinders with flat tails behave completely different despite their similar aspect ratio (Narayan *et al.*, 2006).

In the third publication of this thesis (section 2.3), experiments were focused on particles with a circular cylindrical geometry, as shown in Fig. 1.1. Aim of the work was the investigation of the phase behavior for this particular type of granular rods. The rods were confined to a circular container of limited height to ensure a real monolayer of particles. The whole confinement was agitated with a vertically orientated sinusoidal stimulation to generate the self-organization of particles. In order to detect deviations from the harmonic movement of the shaking device, the acceleration was monitored with an accelerometer. For typical frequencies and amplitudes of the experiments, the total harmonic distortion in the case of an empty container was found to be below 6% (see Appendix A). A comparison with typical signals for a filled container shows that this can be neglected compared to the distortion generated by the bouncing particles. More details on the set-up and the experimental procedure can be found in the third publication (section 2.3).

The boundary can have a pronounced impact on the phase behavior of a driven granular system. Compared to the three-dimensional case, the influence of bounding walls is even stronger in quasi-two-dimensional experiments (Börzsönyi & Stannarius, 2013). For example, a rectangular geometry of the container enhances the alignment of granular rods in directions parallel and perpendicular to the border (Sánchez & Huerta, 2014). To reduce such effects, the experiments described in publication three (section 2.3) were performed in a circular container. Moreover, the influence of the boundary was checked by the determination of the angular correlation between the rods and the wall. The correlation was found to decrease with increasing distance from the border of the container. Consequently, further investigations on the orientation of the anisometric grains were restricted to the center of the container, where the wall-rod-correlation was small enough to assume a bulk-like behavior.

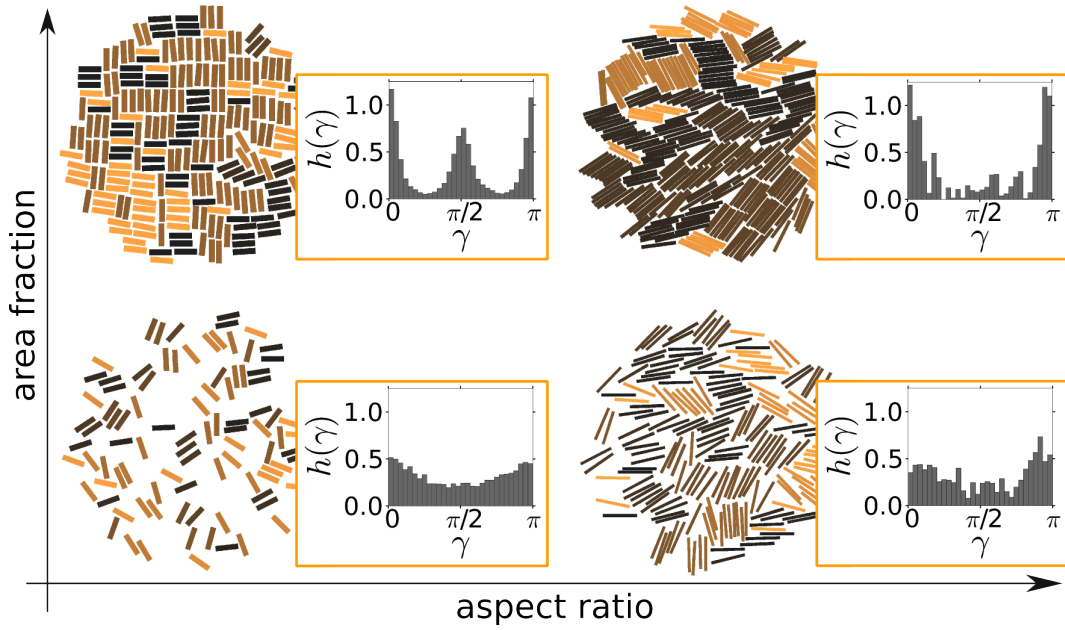


Figure 1.12: Illustration of isotropic (lower left and lower right), tetratic (upper left) and uniaxial nematic (upper right) states as found in an agitated granular monolayer system. The particles are color coded according to their orientation. The corresponding diagrams show examples of the angular distribution $h(\gamma)$ with respect to the director \hat{n} .

In the central region of interest, definitions similar to molecular systems were used to identify the order within the granular monolayer. After calculating the director \hat{n} , indicating the preferred direction of the rods, the orientational distribution $h(\gamma)$ was determined, where γ is the angle of the rods with respect to \hat{n} (see also section 1.2.1). Experiments with different area fractions (packing density of particles) and numerous aspect ratios (length to width ratio of the rods) revealed various configurations of rods in the bulk. A schematic diagram of the possible states and the corresponding orientational distribution $h(\gamma)$ is shown in Fig. 1.12.

On the one hand, an isotropic state was observed for dilute situations with few particles, where the orientations γ of all rods were distributed equally. On the other hand, at higher area fractions, a fluidized state of rods with positional disorder of the centers but simultaneous orientational order was found, reminiscent to liquid crystals. For short rods, a tetratic state with fourfold rotational symmetry arose, where the particles had both, a preferred alignment along the director \hat{n} as well as perpendicular to it. In contrast, longer rods offered uniaxial nematic correlations with a preferred alignment parallel to the director.

The exhibition of the mesomorphic states was detected by using the uniaxial

nematic order parameter q_2 and the tetratic order parameter q_4 , which are defined as

$$q_k = \int_0^\pi d\gamma h(\gamma) \cos(k\gamma), \quad k = \{2, 4\}. \quad (1.14)$$

In consideration of both parameters, a quantitative discrimination of the isotropic state ($q_2 \approx 0, q_4 \approx 0$), the tetratic state ($q_2 \approx 0, q_4 > 0$) and the uniaxial nematic state ($q_2 > 0, q_4 > 0$) is possible. Further details on the determination of the order parameters are provided in the publication (section 2.3).

Investigations on the driving of the system indicated that the details of the energy input do not play a crucial role for the formation of ordering. A variation of the amplitude and the frequency of the sinusoidal shaking revealed similar critical area fractions where the transition from an isotropic into an ordered state is taking place. Thus, the aspect ratio of the rods and the local area fraction were found to be the key parameters for the ordering in such quasi-two-dimensional vertically vibrated systems. Consequently, a systematic study yielded a state diagram, illustrating the range of isotropic, tetratic and uniaxial nematic states (see section 2.3).

In general, computer simulations have shown to be a suitable tool for testing the applicability of microscopic theories on granular dynamics and for modeling granular processes. In particular, Monte Carlo techniques, based on classical statistical mechanics, have often revealed a proper description of the arrangement of grains in a real granular system (Mehta, 2007). Thus, equilibrium Monte Carlo simulations with periodic boundary conditions were also performed for a comparison with the experimental state diagram of the agitated cylindrical rods. The particles were modeled as two-dimensional hard rectangles that interact only through excluded volume interactions. Further details on the simulation method are provided in the third publication (section 2.3).

The state diagrams of simulation and experiment exhibited strong qualitative similarities. At high enough area fractions, an ordering of the two-dimensional rectangles was found in both simulation and experiments. Furthermore, the simulations indicated a tetratic state for small aspect ratios and a uniaxial nematic state for bigger aspect ratios, which is also in consistency with the experimental results. For the aspect ratio where the order changes from a tetratic into a uniaxial nematic type, even quantitative agreement was found. This observations suggest some universality of the self-organization of rod-shaped particles across equilibrium and nonequilibrium systems.

However, the comparison of the nonequilibrium experiments with the equilibrium Monte Carlo simulations also illustrated some nonuniversal aspects. The critical area fraction of the transition offered an increasing deviation with increasing aspect ratio of the rods. Thus, in experiments, a much higher area fraction was necessary to generate a uniaxial nematic ordering. The reason for this quantitative discrepancy might be attributed to various mechanisms that are only existing in the experimental system. Strong fluctuations in the nonequilibrium steady states of the shaken rods, as well as a not negligible frustration of orientational order by the container are possible explanations. Furthermore, dissipative interactions in the experimental system can

lead to additional effects like clustering of the rods, which is not the case in Monte Carlo simulations.

1.3.3 Dissipative mechanisms in granular matter

The dissipative nature is one of the fundamental properties of granular matter. As a consequence, continuous energy injection, for example by strong enough external agitation, is necessary to keep an accumulation of grains in a moving state. With the stoppage of energy input, the grains almost instantaneously stop their collective motion and the whole system stays at rest.

During agitation, the individual particles are gliding and rotating on top of each other, frictional forces resist their relative motion and kinetic energy is converted into heat. Thus, surface properties like shape and roughness of the individual constituents can strongly influence the amount of dissipation. Furthermore, frictional movement might cause the generation of electrostatic charges on the surface of the material. Then, additional attractive or repulsive forces can affect the collective motion, especially if the mass of the individual grains is very small. Besides of these frictional effects, collisions of particles imply the second important dissipative process in granular media.

Inelastic impacts and the coefficient of normal restitution

Consider the idealized case of a frontal elastic collision of two rotationless solid spheres. Macroscopically, the situation can be analyzed very quickly with the application of the two principles of classical mechanics, namely conservation of momentum and kinetic energy. From a more microscopic point of view, slight deformations of the particles due to the imposed loads have to be considered. In 1882, the German physicist Heinrich Hertz devised a quasi-static elastic theory and calculated the penetration of two colliding spheres (Hertz, 1882). He calculated the stored elastic energy during the penetration, dependent on the elastic moduli and the Poisson's ratios of the interacting particles. Furthermore, integrating over the penetration depth, he could estimate the duration of the collision (Duran, 2000).

However, in real solid bodies, purely elastic collisions will never be observed. Instead, dissipative effects like viscoelasticity or plastic deformations have to be taken into account. Additional loss of energy can arise from sound waves propagating through the interior of the colliding substances. By heating up the mass, the acoustic waves or phonons will relax. Moreover, inhomogeneities of material parameters like the elastic modulus can also influence real collisional events. Even though appearing macroscopically smooth, the surfaces of the colliding objects are typically laced with microscopic scratches, cracks or oxidation, resulting in experimental deviations from the idealized theoretical descriptions (Duran, 2000).

In experimental studies of granular impacts the microscopic details are very difficult to access. Therefore, a simplified macroscopic description of rigid body collisions is often appropriate. The coefficient of restitution is commonly used to identify the

loss of momentum and kinetic energy during the collision. Its definition is a result of Isaac Newton's laws of motion from the year 1687, where he compared the speed of separation for two spherical objects with their speed of approach (Motte, 1729). According to Newton, the coefficient of normal restitution e_n for a one-dimensional frontal collision is defined as the ratio between the total momentum of the two-particle system before and after the impact (Duran, 2000),

$$e_n = -\frac{u_1 - u_2}{v_1 - v_2}. \quad (1.15)$$

Here, v_i and u_i denote the velocity of particle $i \in \{1, 2\}$ immediately before and after the collision, respectively. The negative sign in front of the fraction stems from considering the direction of movement in the definition of v_i and u_i . The coefficient of normal restitution ranges between $e_n = 1$ for a perfectly elastic collision and $e_n = 0$ for the completely inelastic case, where the kinetic energy is dissipated completely.

Although it is only a phenomenological approach and details of the kind of dissipation mechanism are ignored, the coefficient of normal restitution remains a proper tool for the description of experimental results or the implementation of dissipative effects into granular dynamics simulations. With the additional consideration of a tangential coefficient of restitution, even oblique collisions can be described. But, frictional effects and gliding or rolling motions have to be taken into account for this nonfrontal case (Duran, 2000).

For the particular example of a sphere that is bouncing normally on a heavy and perfectly elastic plate at rest, the massive plate is expected to receive no kinetic energy. Then, Eq. (1.15) simplifies to $e_n = -\frac{v_{\text{reb}}}{v_{\text{imp}}}$, the ratio between rebound and impact velocity of the rotationless sphere. Nevertheless, such a reduced system is far from being trivial as the coefficient of restitution is more than a material property.

Ramírez *et al.* (1999) found that a constant e_n can only be observed for cubic particles with surfaces normal to the direction of collision. In contrast, the bouncing of spherical particles on fixed flat surfaces reveals a dependency on the impact velocity v_{imp} of the sphere. Theoretical considerations for viscoelastic, smooth spheres indicated that $1 - e_n$ can be expressed as a series in powers of $v_{\text{imp}}^{1/5}$ (Schwager & Pöschel, 1998). Recently, an oscillating superposition with this decay was found and explained by vibrations of the colliding bodies (Müller *et al.*, 2013a). Moreover, the above mentioned microscopic surficial imperfections were identified through non-Gaussian fluctuations in $e_n(v_{\text{imp}})$ (Montaine *et al.*, 2011). Thus, for the case of plastic deformations, fractures or adhesion, the dependency of $e_n(v_{\text{imp}}) \approx 1 - v_{\text{imp}}^{1/5}$ may not hold (Ramírez *et al.*, 1999).

Wet impacts

If the surfaces of the interacting solids are covered with some liquid material, additional dissipative mechanisms gain in importance. Figure 1.13 shows some exemplary snapshots for the impact and rebound of a spherical particle on a wet surface. During such a wet impact, the kinetic energy of the particle is reduced by the action of

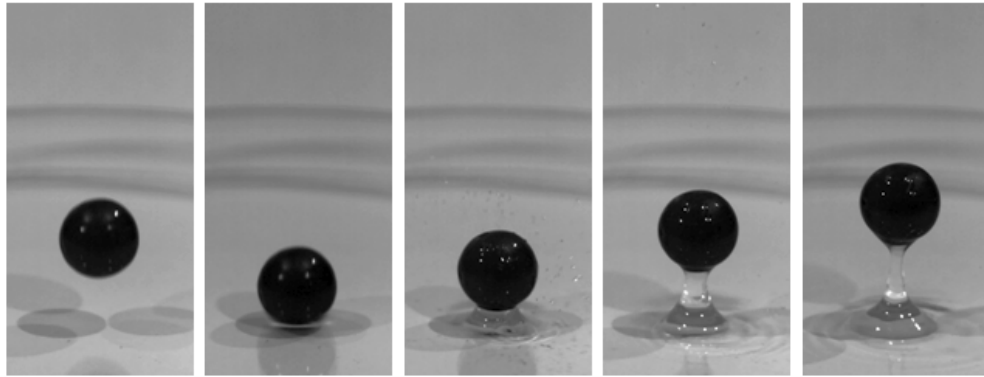


Figure 1.13: Impact and rebound of a spherical particle on a plane wet surface. Viscous damping, acceleration of the liquid and the rupture of the liquid bridge cause the dissipation of energy.

viscous forces, when traveling through the liquid layer. While this viscous damping is dominating in the low Reynolds number regime, especially for lower viscosities and higher impact velocities, inertia effects may become more prominent. Some amount of liquid is always pushed aside and kinetic energy from the sphere is transferred into the acceleration of the liquid. In addition, the deformation and rupture of liquid bridges are connected with capillary forces that will also cause the loss of kinetic energy during the rebound from a wet surface (Gollwitzer *et al.*, 2012).

At ambient conditions, a certain amount of humidity is always present and can already cause the clump of small granular particles. In industrial processes, this is often an undesirable effect, as a blockage can hinder the continuous flow of dry granular particles. However, it can also be the other way round, like in the pharmaceutical industry, where the agglomeration of powders through liquid binders is used to produce granular pills. Regardless of being desirable or not, the detailed understanding of wet granular impacts is of fundamental interest. Thus, experimental investigations on the wet coefficient of normal restitution were performed and discussed in the fourth publication (section 2.4).

In the experiments, freely falling spheres with diameters of several millimeters were bouncing on a flat and heavy surface that was covered with a thin film of viscous liquid. Silicone oil of low surface tension was chosen as liquid material in order to avoid a dewetting of the surfaces. The thickness of the liquid layer was monitored optically and typically varied in the range of several hundred micrometers. However, in consideration of future investigations, an extension of the optical film thickness measurement up to several millimeters was demonstrated. The optical monitoring revealed many advantages in comparison to an estimation via the volume of the liquid. For example, interfering factors like meniscus forming at the boundary of the confinement and a possible loss of liquid could be detected. Besides, the

optical monitoring revealed real-time information about the stability of the liquid film. Publication number four (section 2.4) provides more details on the liquid layer measurement.

Using high-speed imaging, the position of the sphere was traced and the velocities of impact, v_{imp} , and rebound, v_{reb} , were determined. A variation of the falling height of the sphere yielded the coefficient of normal restitution e_n for various impact velocities. Due to the above mentioned additional dissipative effects, wet collisions display a different trend of $e_n(v_{\text{imp}})$ compared to the dry counterpart. First of all, a sticking criterion is found by means of a lower limit of the impact velocity. Below the critical velocity v_c , the viscous and cohesive effects are too strong and no rebound of the sphere is possible. Secondly, the raise of v_{imp} above v_c results in an increase of e_n up to a maximum value of e_{inf} for infinitely large impact velocities. As a first approximation, the velocity dependency of the wet coefficient of restitution can be described by

$$e_n(v_{\text{imp}}) = e_{\text{inf}} \left(1 - \frac{v_c}{v_{\text{imp}}} \right). \quad (1.16)$$

Former experiments on wet impacts of glass spheres demonstrated that many parameters affect the individual values of v_c and e_{inf} (Gollwitzer *et al.*, 2012). In general, a reduction of the sphere diameter as well as an enlargement of the liquid film thickness results in a reduction of e_n . A higher viscosity of the liquid causes a lowering of e_n , too. Gollwitzer *et al.* (2012) described that a scaling of e_n with dimensionless numbers is possible, at least for the particular case of glass spheres. The Stokes number St , defined as the ratio between the inertia of the particle and the viscosity of the liquid, was identified as a crucial parameter. As long as the ratio between the liquid film thickness and the particle diameter was kept constant, the dependency of e_n on impact velocity, thickness and viscosity of the liquid film could be characterized by St . More precisely, a linear dependency between e_n and St^{-1} was found.

In order to shed light on the universality of this scaling, a variation of material properties like density or elasticity of the spheres is necessary. Thus, the experiments described in the fourth publication (section 2.4) were performed with beads made of polyethylene instead of glass, yielding a different density ratio between particle and liquid substance. Due to the reduced elasticity, the dry coefficient of restitution of the polyethylene spheres was found to be around ten percent below the corresponding value for glass. Wet impacts of various particle sizes and liquid film thicknesses manifested the general relationship between e_n and v_{imp} according to Eq. (1.16). Moreover, the linear dependency between e_n and St^{-1} for a fixed size ratio of liquid film thickness and particle diameter was also reproduced for the polyethylene spheres.

Hence, the results of the fourth publication (section 2.4) reinforced the possibility of scaling e_n with the Stokes number. Such an application was initially introduced in the low Reynolds number regime, where the liquid is highly viscous or the film thickness is small and therefore viscous forces are dominant. Nevertheless, the two dimensionless quantities, Stokes number and size ratio of liquid and sphere, offer

1 Mesophases in Molecular and Granular Systems

a good approximative description of the wet coefficient of restitution even beyond this limit. Hence, this scaling indicates to be a proper candidate for the modeling of wet granular matter in computer simulations. However, additional investigations on various ratios between liquid film thickness and particle diameter as well as on further density ratios between solid and liquid are necessary to deepen the understanding of wet impact mechanics.

1.4 Conclusions and Outlook

This thesis and the corresponding publications highlighted some examples of mesophase forming physical systems, where the size of the anisotropic constituents was ranging from the order of Ångström to several centimeters. To begin with, a thermotropic low molecular weight liquid crystal has been described. In this molecular system, the temperature was the leading parameter for controlling the transition into a mesophase, designated by an orientational order of the elongated molecules. Besides, the addition of a functionalized liquid crystalline block copolymer has been discussed, as it revealed various manipulations of the nematic host.

In the dilute regime, the mixtures could be treated as usual nematic liquid crystals with modified viscous properties. In particular, a deceleration of the electro-optical response has been observed. The nonlinear increase of the rotational viscosity with increasing polymer concentration was attributed to the formation of polymer loops and small clusters, induced by the nonsoluble block copolymer end blocks. Other than the dynamical properties, the splay elasticity and the critical voltage of the liquid crystal were not affected by the addition of the polymer.

The first observations in the dilute regime indicated no dramatic disturbance of the global nematic alignment by the existence of the flexible polymer chains. However, on long timescales, an alteration of the liquid crystal polymer mixtures has been observed. Apart from an overall decrease of the rotational viscosity, the passing of time led to detectable local impurities in the nematic host. Polarizing microscopy depicted regular patterns in an otherwise well aligned nematic surrounding. The electro-optical response and a phenomenological estimation of the director field indicated that the defects were presumably generated by local agglomerations of polymer chains into big clusters.

In contrast to such molecular systems, where thermal energy was playing an important role, the effect of temperature could be confidently neglected in the subsequent investigation of centimeter-sized particles. In spite of the absence of intermolecular forces that are classically necessary for the explanation of states of matter in thermal systems, the appearance of mesomorphic states has also been demonstrated in these granular systems. Due to the dissipative character of granular matter, a sufficient external vibration was necessary to generate a motion of particles. In a monolayer of cylindrical rods, such a "thermalization" resulted in a reorientation of the particles and orientational ordering with various symmetries. Contrary to the thermotropic liquid crystals, where the formation of a mesomorphic state was controlled by adjusting the temperature, a variation of the agitation strength was found to play a minor role for the ordering of the fluidized particles.

The macroscopic character of the granular system facilitated the easy modification of the size of the rods and a systematic study on the length-to-width ratio. As a result, this ratio was found to be the crucial parameter to determine the type of order. While long rods displayed a uniaxial nematic arrangement with twofold rotational symmetry, shorter rods presented a tetratic order with fourfold rotational symmetry. A sufficiently high area fraction was proven as a necessary precondition

for the appearance of orientational order. Such a dependency on the bulk density of particles strongly reminds of lyotropic systems. There, elongated molecules in solution are often delineated by hard rods, only interacting through excluded volume interactions. The concentration dependent transition into mesomorphic states is described by a maximization of configurational entropy.

A comparison of the nonequilibrium granular rod experiments with equilibrium Monte Carlo simulations of the corresponding two-dimensional hard rectangle system demonstrated strong qualitative agreement. For the critical length-to-width ratio, where the transition from the tetratic into the uniaxial nematic order is taking place, even quantitative accordance between simulation and experiment was found. But still, further investigations are necessary to clarify the limits of such a comparison and to understand the dissimilarities between anisotropic thermal and athermal systems.

For example, in the experimental studies, the orientational order of rods was only analyzed in small regions of interest, far away from the border of the container. However, due to the reduced size of real granular systems, a potential influence of the boundary always has to be considered. Similar to boundary effects in molecular liquid crystals, director deformations and local defects can also take place on a granular scale. Former experiments with vibrofluidized granular rods in a quasi-two-dimensional system have already demonstrated such imperfections of the nematic alignment, induced by the competition between boundary and bulk (Galanis *et al.*, 2010*b*). Moreover, a continuum liquid crystal free energy functional could be adopted to estimate the "elasticity" of the granular mesophase. While in molecular systems, special coatings and chemical treatments of the boundary are established to modify the alignment of the director, the granular analog is not yet explored in detail. Hence, a closer view on anchoring effects at macroscopically rough or undulated boundaries could uncover further similarities or dissimilarities between granular and molecular anisotropic systems.

Moreover, the specific shape of the grains is also known to strongly influence the appearance and the type of the granular mesophase (Narayan *et al.*, 2006). In thermal liquid crystalline systems, a classification of liquid crystalline phases has already been worked out for plenty of molecular geometries. In contrast, in driven granular media, such a classification is only at the beginning. Hence, a systematic variation of the granular shape is an important topic for future experimental investigations.

The existence of mesophases is not the only illustration of similarities between thermal and athermal systems. Another approach of comparison bears upon the last part of the microscopic studies in this thesis, where the gelation of a liquid crystal has been described. In this thermal system, at sufficiently high concentrations of the functionalized triblock copolymers, the self-assembly of the polymer end blocks led to the formation of a physical network. Such a formation of network-like structures can also be detected in granular systems. Self-assembly has recently been observed in a binary mixture of vibrofluidized rods and spheres (Galanis *et al.*, 2010*a*). There, the spheres induced the aggregation of rods into finite sized clusters, reminding of linear polymer-like structures.

Besides, the wetting of sparsely packed granular particles can also induce an

aggregation into chains or clusters (Huang *et al.*, 2012). In such wet systems, the formation of network-like structures relies on the formation of liquid bridges between the individual particles. Thus, an additional wetting of the driven granular rods will certainly influence the relevant parameters for the occurrence of orientational ordering and probably include new features due to the anisotropy of the contact surfaces. In a horizontally driven system of wet granular spheres, the surface melting and breakage of clusters has been demonstrated to be dependent on the movement of the confinement (May *et al.*, 2013). Hence, in contrast to the dry experiments, the driving frequency and strength would certainly influence the orientational order and the formation and destruction of anisotropic granular clusters in the wet case.

In the gelified liquid crystalline system described in this thesis, the polymer network hindered the liquid crystal solvent from forming a monodomain nematic state. With some modification of the wetting properties of the particles, a similar behavior might be also conceivable in a driven granular system. A mixture of hydrophobic and hydrophilic rod-like particles in a wet environment might result in small areas of mesomorphic states, separated by a network that is built by the hydrophilic particles. Amongst others, the amount of kinetic particle energy and the wet coefficient of restitution will strongly affect the collective behavior in such a granular system.

This reinforces the detailed analysis of the dissipative mechanisms during wet granular impacts as discussed in the last part of this thesis. For the impact of spherical particles on flat surfaces, plenty of parameters like impact velocity, sphere size, film thickness and viscosity of the liquid have been found to determine the amount of dissipated energy. At least for the special case of a bouncing sphere, a scaling of the coefficient of normal restitution with the Stokes number could be confirmed. A variation of the material even demonstrated that this scaling is applicable for different materials of the impacting sphere. However, investigations on more complex geometries are required in order to increase the understanding of the collective behavior of driven wet granular matter. For example, the accurate analysis of capillary bridges between more than two particles could deepen the understanding of transient agglomerates in agitated wet granular particles. Furthermore, apart from the material properties, a variation of the particle shape is expected to manipulate the strength of a wet granular network.

In summary, this thesis inspected particular examples of mesophases on a molecular and on a granular scale. The formation of orientationally ordered states in both thermal and athermal systems can be used as a starting point for further investigations and comparisons of liquid crystalline systems and agitated granular matter. Because properties of molecular systems are often difficult to probe directly on the nanometer scale, a changeover into the appropriate granular model system can yield a useful macroscopic instrument to shed light on molecular patterning.

2 Publications

2.1 Gel formation in a mixture of a block copolymer and a nematic liquid crystal

Authors: Maxim Khazimullin, Thomas Müller, Stephan Messlinger, Ingo Rehberg, Wolfgang Schöpf, Alexei Krekhov, Robin Pettau, Klaus Kreger, and Hans-Werner Schmidt

Journal: Physical Review E

Volume: 84

Article: 021710

Pages: 1–11

Date of publication: August 29, 2011

DOI: <http://dx.doi.org/10.1103/PhysRevE.84.021710>

© 2011 American Physical Society

Gel formation in a mixture of a block copolymer and a nematic liquid crystalMaxim Khazimullin,^{*} Thomas Müller, Stephan Messlinger, Ingo Rehberg, and Wolfgang Schöpf[†]
*Experimentalphysik V, Universität Bayreuth, DE-95440 Bayreuth, Germany*Alexei Krekhov[‡]
*Theoretische Physik I, Universität Bayreuth, DE-95440 Bayreuth, Germany*Robin Pettau, Klaus Kreger, and Hans-Werner Schmidt[§]
Makromolekulare Chemie I, Universität Bayreuth, DE-95440 Bayreuth, Germany
(Received 14 March 2011; published 29 August 2011)

The viscoelastic properties of a binary mixture of a mesogenic side-chain block copolymer in a low molecular weight nematic liquid crystal are studied for mass concentrations ranging from the diluted regime up to a liquid crystalline gel state at about 3%. In the gel state, the system does not flow, exhibits a polydomain structure on a microscopic level, and strongly scatters light. Below the gelation point, the system is homogeneous and behaves like a usual nematic, so the continuum theory of liquid crystals can be applied for interpreting the experimental data. Using the dynamic Fréedericksz transition technique, the dependence of the splay elastic constant and the rotational viscosity on the polymer concentration have been obtained. Comparing the dynamic behavior of block copolymer solutions with the respective homopolymer solutions reveals that, above a mass concentration of 1%, self-assembling of the block copolymer chain segments in clusters occurred, resulting in a gel state at higher concentrations. The effective cluster size is estimated as a function of the concentration, and a scaling-law behavior near the sol-gel transition is confirmed. This technique may serve as an alternative method for determining the gelation point.

DOI: [10.1103/PhysRevE.84.021710](https://doi.org/10.1103/PhysRevE.84.021710)

PACS number(s): 42.70.Df, 83.80.Kn, 64.70.mj, 82.70.Gg

I. INTRODUCTION

Gels are systems that consist of at least two components: the minor component forms an elastic network (e.g., by means of cross-linked polymer molecules), which prevents the major component, a liquid, from flowing out [1,2]. As a consequence, a gel is solid in the sense that it keeps its shape, but is easily deformed by mechanical forces. Liquid crystals are anisotropic fluids with a long-range orientational order, resulting in a very sensitive response to external fields [3]. Using a low molecular weight liquid crystal as a solvent, liquid crystalline gels can be prepared that combine the soft-solid nature of the gel with the anisotropy of the liquid crystal [4,5]. Due to the weak resistance of the gelator network to mechanical forces and the high susceptibility of liquid crystals to external fields, the shape of the liquid crystalline gel can be easily changed by a low electrical voltage [6,7], thus permitting the creation of microactuators or artificial muscles [8]. It has been shown recently that, in a liquid crystalline gel, the electro-optical response can be fast due to the elastic interaction between the liquid crystal and the network [9]. Because of the polydomain structure forming in nonaligned liquid crystalline gels, such displays can be operated in scattering mode and, thus, do not require polarizers. From a fundamental point of view, one of

the most interesting issues in these gels is the consequence of the coupling between the elastic network and the liquid crystal ordering.

Liquid crystalline gels can be prepared in different ways by mixing low molecular compounds or various polymers (gelators) with a liquid crystal. In chemical gels, an extended network is formed due to chemical or photochemical reactions between the gelator molecules [4,10]. A typical feature of such a system is irreversibility: once formed, the network can not be destroyed easily. In a physical gel, on the other hand, the network is formed due to intermolecular interactions between the gelator molecules that lead to the thermoreversibility of the physical cross links in the network. The physical properties of such systems can be changed relatively easily, e.g., by temperature, which makes them attractive for the study and the implementation of new device operation principles [4].

An interesting approach is the creation of physical liquid crystalline gels where triblock copolymers are used as a gelator [9,11]. The block copolymers consist of a middle block with attached liquid crystal mesogens so that it is miscible with a liquid crystal, and of end blocks that are well soluble in the isotropic phase but not in the nematic phase of the solvent. Due to microphase separation, the end blocks are aggregating in the nematic solvent, creating the nodes of a supramolecular network. By heating the gel above the nematic-isotropic transition temperature (the clearing point), the network is disassembled, showing the reversible nature of the system [9,12]. Such gels typically form a polydomain structure at room temperature that scatters light intensively. It is also possible to create monodomain samples by shearing or by applying a strong magnetic field while cooling the

^{*}Permanent address: Institute of Physics of Molecules and Crystals of the Ufa Scientific Center, Russian Academy of Science, Ufa, Russia.

[†]wolfgang.schoepf@uni-bayreuth.de

[‡]alexei.krekhov@uni-bayreuth.de

[§]hans-werner.schmidt@uni-bayreuth.de

sample down from the isotropic state [9]. The peculiarities of the rheological behavior near the clearing point have been attributed to changes in the network structure of the liquid crystalline gel and are not yet fully understood [12]. Dynamic light scattering shows two different time scales [13]: a fast scale that has been related to the orientational relaxation and a slow scale arising from the network rearrangement process.

While the investigations of the viscoelastic and optical properties of physical liquid crystalline gels are currently only at the beginning, much more effort has been invested to understand the structure of individual polymer chains and the dynamic properties of dilute solutions of various polymers in nematic solvents [14]. The main feature is that the conformation of a single polymer chain in a nematic environment is anisotropic [15–17]. The shape of the polymer chain strongly depends on the chemical structure of the polymer and also changes with temperature [9,14,18–20]. Typically, main-chain polymers, where mesogens are part of the backbone, develop a strong prolate conformation with the long axes being parallel to the nematic director [14]. For a side-chain polymer, a prolate conformation is observed for side-on attachment and an oblate conformation for end-on attachment of the mesogenic units [9,21].

The flow properties of polymer solutions in nematics are characterized by an anisotropic viscous tensor, with the viscosity coefficients strongly depending on the chain conformation leading to remarkable effects. In particular, the addition of liquid crystalline side-chain polymers to a vertically aligned liquid crystal reduces the backflow effect, which arises during the director reorientation and is undesirable in displays [18]. Depending on the viscosity coefficients, nematic liquid crystals are oriented at a certain angle relative to the direction of the flow, so-called flow-aligning nematics, or show a tumbling behavior. The addition of a main-chain polymer with a prolate conformation changes the rheology from a tumbling behavior to a flow-aligning behavior [22]. The opposite effect is observed when using a side-chain polymer with oblate chain shape [22,23].

Despite numerous studies of a polymer dissolved in a liquid crystal, most of them were done in diluted solutions, or for polymers that do not form a liquid crystalline gel [14]. In this paper, we study the transition from the diluted regime to the gel state of triblock copolymer solutions in a nematic liquid crystal by varying the polymer concentration. We use the Fréedericksz transition technique, which is based on the optical detection of the reorientation of the liquid crystal in an electric field [24,25]. The optical response to a slowly changing electric field allows us to study the elastic properties, while switching the field on and off yields information about the viscous properties. Previously, this technique has been successfully applied to investigate dilute solutions of a polymer in a liquid crystal [18,26] and to liquid crystalline gels [27–29]. Our results on the orientational dynamics of the block copolymer solutions approaching the gel point allow to identify the self-assembling of individual chains in clusters. Based on the Brochard model [15], we find a scaling-law behavior of the cluster sizes as well as the critical concentration for the sol-gel transition.

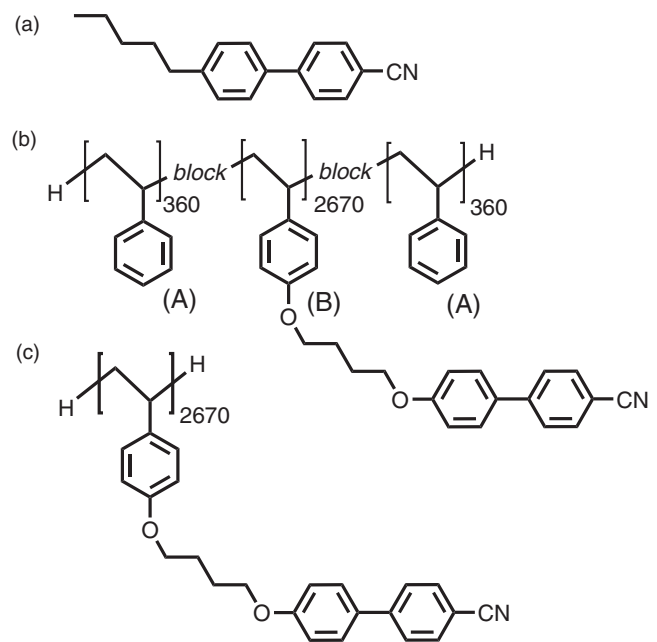


FIG. 1. (a) Nematic liquid crystal 4-cyano-(4'-pentyl)biphenyl, 5CB. (b) Cyanobiphenyl functionalized block copolymer. (c) Corresponding homopolymer. The average number of repeating units of each segment is given.

II. SAMPLE PREPARATION AND EXPERIMENTAL SETUP

A. Sample preparation

We use the low molecular weight liquid crystal 4-cyano-(4'-pentyl)biphenyl [5CB; see Fig. 1(a)], which is commercially available from abcr GmbH. 5CB is nematic at room temperature with a nematic-isotropic transition (clearing point) at 35 °C.

The chemical structure of the mesogenic side-chain block copolymer (MSCBCP) used for our mixtures is shown in Fig. 1(b). This block copolymer was specifically designed to act as a gelator for low molecular weight liquid crystals. To achieve this, the middle block (B) was functionalized with moieties that are structurally similar to 5CB so that this segment is soluble in the isotropic and in the nematic phase of 5CB. In contrast, the polystyrene end blocks (A) of the MSCBCP are insoluble in the nematic phase but soluble in the isotropic phase of 5CB. Dissolution of the end blocks in a nematic solvent is unfavorable because it drastically decreases the enthalpy of the dissolved polymer. Upon cooling below the clearing temperature, the middle block remains dissolved, whereas the end blocks phase separate from the nematic solvent. Above a critical block copolymer concentration, a physical network is formed when the end blocks of different block copolymer chains self-assemble and form the nodes of the network [9].

This ABA-triblock copolymer comprises a poly(4-hydroxystyrene) middle block (B) functionalized with 4-cyanobiphenyl moieties, which is covalently linked to polystyrene end blocks (A) and was prepared by a polymer-analogous approach [30–33]. The polymer backbone was prepared by sequential anionic polymerization of 4-tert-butoxystyrene and styrene in tetrahydrofuran with sodium naphthalene as initiator. Prior to the polymer-analogous

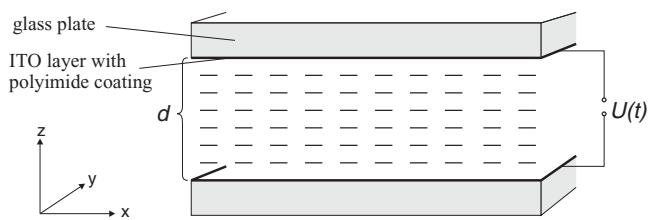


FIG. 2. Sketch of the liquid crystal cell and definition of the coordinate system.

functionalization, the tert-butoxy protection group was removed by acidic cleavage. 4-(4-bromobutoxy)-4'-cyanobiphenyl moieties, which were prepared separately, were subsequently attached to the middle block in a polymer-analogous etherification reaction. The degree of conversion of the polymer-analogous reaction was determined by $^1\text{H-NMR}$ to 84%. The molecular weight was analyzed by size exclusion chromatography (SEC). The number-average molecular weight M_n of the MSCBCP was determined to 1560 kg/mol with a polydispersity index of 1.29. The repeating units were determined from the results of $^1\text{H-NMR}$ and SEC from the precursor polymer to be 360 in the A block and 2670 in the B block. Details regarding the synthesis and characterization of the block copolymer and of the respective homopolymer (see below) can be found in the Supplemental Material [34].

Mixtures of the block copolymer and 5CB were prepared by weighing the solvent and the respective amount of polymer in a 1.5-mL vial. The closed vial was placed in a tumble mixer at a temperature of 50°C for three days to ensure homogeneous mixing. For our experiments, mixtures with block copolymer mass concentrations c ranging from 0.2% to 5% have been used. Rheology measurements revealed that the critical mass concentration of the block copolymer, at which the system is gellified, is around 3% [35].

For the dynamic and static measurements, the different MSCBCP-5CB mixtures were filled into commercially available liquid crystal cells (see Fig. 2 for a sketch).¹ They consist of two parallel, transparent electrodes [glass plates with an indium tin oxide (ITO) layer on the inside], which are separated by spacers. The ITO surfaces of the electrodes are coated with polyimide and rubbed in one direction in order to produce a planar alignment. When this probe is filled with a nematic material, the director is aligned along the rubbing direction in the layer plane. This direction defines the x axis, with the y axis being perpendicular to x in the layer plane. The thickness d of the cell is determined by the spacer that separates the two glass plates in the z direction. We have measured the thickness with an accuracy of $\pm 0.5 \mu\text{m}$, using an interferometric method [36]. For the cells we used, the typical thickness was about $27.5 \mu\text{m}$.

Before filling the cells, the mixtures were heated to and kept at a temperature of 60°C for 2 h. Then, the isotropic solution was filled into the cell by capillary forces. In order to remove concentration gradients that may have formed inside the cell during filling, the system was kept at this temperature for

another 2 h and was allowed to cool to the ambient temperature within 12 h. For block copolymer mass concentrations below 2.5%, the samples were homogeneously aligned directly after filling [Fig. 3(a)]. Above 2.5%, some misalignment of the liquid crystal layer has occurred [Fig. 3(b)], but after keeping the samples for a few weeks at room temperature, monodomain samples were observed. For a block copolymer mass concentration of 5%, the gel network has already formed, therefore, the sample images exhibit a polydomain texture, even after keeping it for several weeks at room temperature [Fig. 3(c)].

To compare the results of the 5CB-block copolymer mixtures with liquid crystal-polymer mixtures where no self-assembly of polystyrene end blocks can occur, we also prepared the respective mesogenic side-chain homopolymer of the middle block of the above-described triblock copolymer. The homopolymer has the same chemical structure as the block copolymer, but without the polystyrene end blocks (A) [see Fig. 1(c)]. The number-average molecular weight was determined to be $M_n = 1637 \text{ kg/mol}$ with a polydispersity index of 1.16. The degree of conversion was 97%. Solutions of the homopolymer in 5CB were prepared in similar concentrations as for the block copolymer. The mixing and filling procedures were performed in the same manner as described above. Due to the missing end blocks, no gel is formed in the homopolymer solutions.

B. Experimental setup

We use the standard experimental setup as described, e.g., in Refs. [37,38] and sketched in Fig. 4. An ac voltage $U(t) = U_{\text{rms}}\sqrt{2}\cos(2\pi ft)$ was applied across the cell by means of a waveform generator (Agilent Technologies, 33220A) and an amplifier with a maximum output voltage $U_{\text{rms}} = 120 \text{ V}$. The voltage at the liquid crystal cell was measured by a digital multimeter (Prema, 5017 DMM) and the frequency was kept constant at $f = 1 \text{ kHz}$ for all measurements. The cell was mounted on a thermostage. The temperature of the cell was kept constant at $T = (25.0 \pm 0.2)^\circ\text{C}$ by means of a circulation thermostat (Lauda, RE305) and was measured with a PT100 platinum temperature sensor with an accuracy of $\pm 0.1 \text{ K}$. The thermostage was fixed to a polarizing microscope (Olympus, BX41). All measurements were done between crossed polarizers. As a light source, a red LED (LedEngin, LZ4-00R115, wavelength $\lambda = 638 \text{ nm}$) was used.

The microscopic images of the samples were captured by a digital USB camera (Lumenera Corporation, LU135M-IO) that has a spatial resolution of 1280×1024 pixels and 256 gray scales. The time intervals between images were provided by a high-precision pulse generator. Depending on the sampling speed, resolutions ranging from 128×128 pixels for the fastest experiments to the full range for slower experiments have been used. The sampling rate was in the range between 0.1 and 25 Hz, depending on the respective experiment. From the acquired images, the transmitted light intensity was determined in different areas of the sample. The experimental setup allows us to measure the dependence of the light intensity on the applied voltage (static measurements) as well as the temporal evolution of the light intensity (dynamic measurements).

¹E.H.C. Co. Ltd., 1164 Hino, Hino-shi, Tokyo, Japan 191.

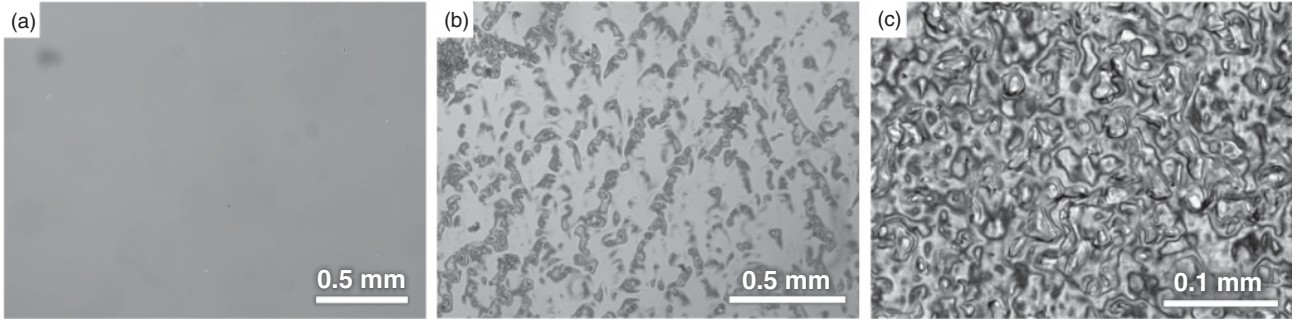


FIG. 3. Images of cells filled with samples of different concentrations c of the block copolymer taken between crossed polarizers. (a) $c = 1.1\%$; (b) $c = 3.0\%$; (c) $c = 5.0\%$. Note the different scales.

For measuring the dielectric anisotropy ϵ_a of the polymer solutions in the liquid crystal, we used a conductivity lock-in amplifier to determine the capacities of the cells as, for example, described in Ref. [39]. ϵ_a can then be calculated by $\epsilon_a = \frac{C_{\perp} - C_{\parallel}}{C_0}$, where C_{\perp} is the capacity of the cell measured at a small ac voltage well below the Fréedericksz threshold, C_{\parallel} is the extrapolated limit of the capacity for high voltages, and C_0 is the capacity of the empty cell.

III. STATIC MEASUREMENTS

A. Birefringence method

The measurement of the critical Fréedericksz voltage U_F is well suited to determine the elasticity in our system, as U_F is determined by the dielectric anisotropy ϵ_a and by the splay elastic constant k_{11} [40,41]:

$$U_F = \pi \sqrt{\frac{k_{11}}{\epsilon_0 \epsilon_a}}. \quad (1)$$

Thus, from the measurements of U_F and ϵ_a , we can detect the influence of the polymer concentration on the elasticity.

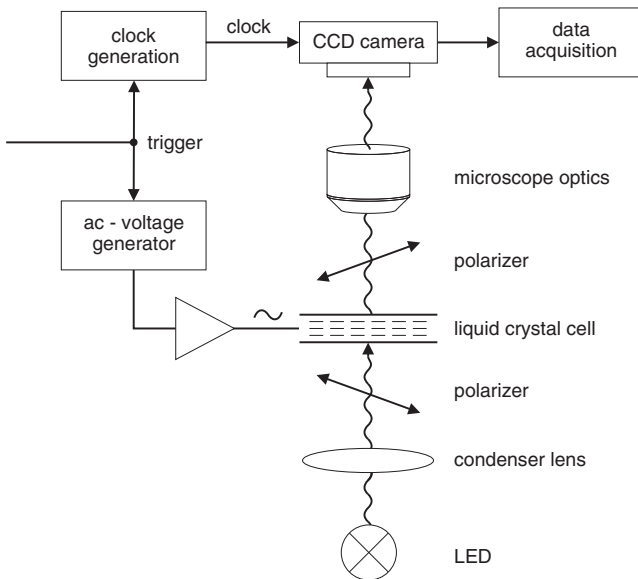


FIG. 4. Sketch of the experimental setup.

For determining the Fréedericksz threshold, we use the birefringence technique [25,41]. The refractive index of a nematic liquid crystal is anisotropic with n_{\perp} being the refractive index for light polarized perpendicular to the nematic director and n_{\parallel} for light polarized along the director. The refractive index for the ordinary light ray n_o is always given by $n_o = n_{\perp}$, even if the director deviates from the original orientation along the x axis, as long as it remains perpendicular to the y axis. The refractive index for the extraordinary light ray n_e , however, depends on the director angle θ , i.e., the angle between the director and the x axis. If θ varies along the z axis, n_e depends on the vertical location inside the cell:

$$n_e = \frac{n_{\perp} n_{\parallel}}{\sqrt{n_{\perp}^2 \cos^2 \theta(z) + n_{\parallel}^2 \sin^2 \theta(z)}}, \quad n_o = n_{\perp}. \quad (2)$$

The birefringence $\Delta n = n_e - n_o$ is 0 for a homeotropic director orientation ($\theta = \frac{\pi}{2}$) and maximal at $n_a = n_{\parallel} - n_{\perp}$ for the initial planar orientation ($\theta = 0$). The birefringence leads to a phase difference δ between the ordinary and the extraordinary ray, where δ is found by integrating Δn over the layer height d :

$$\delta = \frac{2\pi}{\lambda} \int_0^d \{n_e[\theta(z)] - n_o\} dz. \quad (3)$$

In our experimental procedure, we can determine δ from measuring the transmitted light intensity I as a function of the applied voltage U_{rms} , and subsequently the critical voltage U_F from $\delta(U_{\text{rms}})$, as shown in the following.

By using the setup described in Sec. II B with crossed polarizers and an angle of 45° between the polarizers and the x direction, the ordinary and the extraordinary rays are brought to interference. Thus, the intensity of the transmitted light is ideally given by $I = I_0 \sin^2 \frac{\delta}{2}$, when I_0 is the maximally transmitted light intensity. In the experiment, we rather observe

$$I(U_{\text{rms}}) = I_b + I_0 \sin^2 \frac{\delta(U_{\text{rms}})}{2} \quad (4)$$

for a certain voltage U_{rms} above the Fréedericksz transition. I_b is an intensity offset due to stray light and other influences and has to be extracted from the experimental data. Below the Fréedericksz transition, corresponding to the homogeneous planar orientation ($\theta = 0$), the measured intensity $I(U_{\text{rms}})$ is

constant and δ is given by the maximal phase difference $\delta_0 = \delta(U_{\text{rms}} < U_F)$ with

$$\delta_0 = \frac{2\pi d}{\lambda}(n_{\parallel} - n_{\perp}) = \frac{2\pi d}{\lambda}n_a. \quad (5)$$

The minimal phase difference of $\delta = 0$ is reached when the liquid crystal layer is almost homeotropically aligned, i.e., for very high voltages ($U_{\text{rms}} \approx 120$ V in our case). Between these two extrema, the light intensity undergoes a number of minima and maxima, depending on the value of δ_0 and thus on d , λ , and n_a . In order to extract δ and thus δ_0 from the experiment, Eq. (4) has to be inverted, which can only be done piecewise, starting from $\delta = 0$:

$$\delta = 2\pi M + (-1)^N \times 2 \arcsin \sqrt{\frac{I - I_b}{I_0}}. \quad (6)$$

N is the number of intensity extrema and M the number of intensity maxima already encountered. I_b is determined by the nearest minimum and I_0 by the difference between the nearest extrema. Below the Fréedericksz transition, δ remains constant at δ_0 .

The phase difference δ is determined by the director field $\theta(z)$ inside the cell [see Eq. (3)]. Obviously, Eq. (3) can not be inverted, so that $\theta(z)$ can not be determined unambiguously from δ . However, assuming a harmonic director profile slightly above the Fréedericksz transition (see, e.g., Ref. [3]), $\theta(z) = \theta_m \sin(\pi \frac{z}{d})$, where θ_m is the director deflection in the middle of the cell, one finds

$$\delta(\theta_m) = \delta_0 - \delta_2 \theta_m^2 + O(\theta_m^4) \quad \text{with} \quad \delta_2 = \frac{\pi d}{2\lambda} \left(\frac{n_{\parallel}^3}{n_{\perp}^2} - n_{\parallel} \right). \quad (7)$$

Inserting the stationary overcritical director amplitude

$$\theta_m(U_{\text{rms}}) \propto \sqrt{\frac{U_{\text{rms}} - U_F}{U_F}}, \quad (8)$$

as resulting from the pitchfork bifurcation behavior near the Fréedericksz transition [see Eq. (11) below], we expect the supercritical phase difference to decrease linearly from δ_0 :

$$\frac{\delta(U_{\text{rms}})}{\delta_0} - 1 \propto U_F - U_{\text{rms}}, \quad (9)$$

so that U_F is given by the point, where δ deviates from the constant value δ_0 .

B. Results

In order to calculate δ , the intensities have been measured up to $U_{\text{rms}} = 120$ V, where the samples are almost homeotropic with $\delta \approx 0$. We can find δ and thus δ_0 by using Eq. (6). We will use δ_0 , which for our cells is found to be around $\delta_0 \approx 49$ rad, for normalization purposes, so that we can compare the results for different samples. Slightly above the Fréedericksz transition, the orientation of the director changes very slowly so that quasistatic measurements can only be done with very long waiting times between the voltage changes. Figure 5 shows the phase difference δ , normalized by the respective δ_0 , as a function of the applied voltage near the critical point U_F for pure 5CB and for the block copolymer solution with a mass

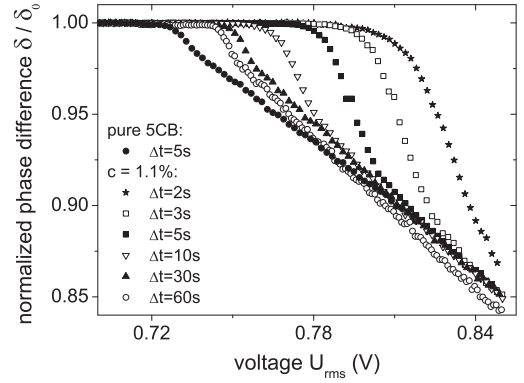


FIG. 5. Voltage dependence of the optical phase difference near the Fréedericksz transition for pure 5CB and for the block copolymer solution with a mass concentration of 1.1%. The voltage steps are always $\Delta U = 2$ mV with different time delays Δt between the voltage steps.

concentration of 1.1% for different waiting times. For pure 5CB, we find $U_F^{5CB} = 0.73$ V, and the Fréedericksz transition leads to a sharp linear decrease of δ as described by Eq. (9). This indicates that the cells provide a planar alignment with no or very small pretilt, which is also confirmed by the observation of domain walls in the sample during the transition.

For the block copolymer solutions, we commonly observe an inhomogeneous Fréedericksz transition, which again we believe is due to domains of opposing director elongations forming in the nonpretilt cells. After switching off the voltage, the samples relax back to the initial state, so that the results can be reproduced. We have used different delay times between the voltage steps of $\Delta U = 2$ mV, varying from $\Delta t = 2$ to 60 s. With increasing delay time, the deviation from the horizontal line $\delta/\delta_0 = 1$ occurs for smaller voltages, misleadingly indicating a successively lower critical value. Even for the largest delay time, we could not reach the same critical value U_F as for pure 5CB, although we will show later in Sec. IV B that the thresholds indeed coincide. It should be noted that, for pure 5CB, all measurement curves coincide already for $\Delta t = 3$ s.

A further increase of the block copolymer concentration leads to prohibitively long waiting times, so that this static method is not convenient for the determination of U_F for our polymer solutions. Nevertheless, we will use the extraction of the phase difference δ for the dynamical measurements described in the next section.

IV. DYNAMICAL MEASUREMENTS

A. Method

By performing dynamical measurements, we can derive the influence of the polymers on the elasticity and on the viscosity of the system. If the applied electrical field is suddenly changed to or from an overcritical voltage $U > U_F$, the director field will reorient with a characteristic time scale. We consider two processes: changing the voltage from a value below the critical point U_F to a target value U_{on} slightly above U_F (the “on” process); and switching the voltage off from a supercritical value (the “off” process).

The orientational behavior near the onset of the Fréedericksz transition is described in the framework of a weakly nonlinear analysis of the nematohydrodynamic equations [3]. For small distortions from the planar ground state, the deformation of the nematic director can be approximated by a single harmonic mode

$$\theta(z, t) = \theta_m(t) \sin\left(\frac{\pi z}{d}\right). \quad (10)$$

Up to third order in θ_m , the resulting dynamic equation for the director amplitude then takes the form [25]

$$\tau_0 \frac{\partial \theta_m}{\partial t} = \varepsilon \theta_m - \beta \theta_m^3, \quad (11)$$

where

$$\tau_0 = \frac{d^2 \gamma_1}{k_{11} \pi^2} \quad (12)$$

is the director relaxation time, $\varepsilon = U^2/U_F^2 - 1$ is the reduced driving voltage, and β is the saturation parameter that determines the final supercritical director amplitude. For the interpretation of our results, the value of β is not important. The director relaxation time τ_0 depends on the rotational viscosity γ_1 . When taking into account the backflow effect, γ_1 should be replaced by $\gamma_1 - \alpha_3^2/\eta$, where $\eta = (\alpha_3 + \alpha_4 + \alpha_6)/2$ and α_i are the Leslie viscosity coefficients. For typical rod-shaped nematics $\alpha_3^2/(\eta\gamma_1) \approx 10^{-3}$, so that the correction to γ_1 can be neglected [25].

For subcritical voltages ($\varepsilon < 0$), all deformations of the director relax to the planar ground state $\theta_m = 0$. For supercritical voltages ($\varepsilon > 0$), the planar state becomes unstable, so that any initial fluctuation θ_i will grow exponentially in time. Caused by the nonlinear term in Eq. (11), the growth will eventually saturate to the stable equilibrium value $\theta_f = \pm\sqrt{\varepsilon/\beta}$, where the sign is determined by the direction of the initial deformation. Note that, in all practical situations, there will always be a small initial deviation from the ideal director alignment along x due to thermal fluctuations.

The saturation behavior of the ‘‘on’’ process is described by the solution of Eq. (11):

$$\theta_{\text{on}}^2(t) = \frac{\theta_f^2}{1 + (\theta_f^2/\theta_i^2 - 1)e^{-2t/\tau_{\text{on}}}} \quad \text{with} \quad \tau_{\text{on}} = \frac{\tau_0}{\varepsilon}. \quad (13)$$

For the ‘‘off’’ process ($\varepsilon = -1$), the nonlinear term in Eq. (11) can be neglected, leading to a simple exponential decay

$$\theta_{\text{off}}(t) = \theta_f e^{-t/\tau_{\text{off}}} \quad \text{with} \quad \tau_{\text{off}} = \tau_0. \quad (14)$$

The combination of τ_{on} and τ_{off} yields the material parameters of the nematic. From $\tau_{\text{off}}/\tau_{\text{on}} = \varepsilon = U_{\text{on}}^2/U_F^2 - 1$, we find the critical Fréedericksz voltage U_F as

$$U_F = \frac{U_{\text{on}}}{\sqrt{\tau_{\text{off}}/\tau_{\text{on}} + 1}}, \quad (15)$$

and the splay elastic constant and rotational viscosity as

$$k_{11} = \frac{\varepsilon_0 \varepsilon_a}{\pi^2} U_F^2 = \frac{\varepsilon_0 \varepsilon_a}{\pi^2} \frac{U_{\text{on}}^2}{\tau_{\text{off}}/\tau_{\text{on}} + 1}, \quad (16)$$

$$\gamma_1 = \frac{\pi^2}{d^2} k_{11} \tau_{\text{off}} = \frac{\varepsilon_0 \varepsilon_a}{d^2} \frac{\tau_{\text{off}} \tau_{\text{on}}}{\tau_{\text{off}} + \tau_{\text{on}}} U_{\text{on}}^2. \quad (17)$$

The optical response of the sample with respect to the birefringence method has already been derived in Sec. III A. Inserting Eqs. (13) and (14) into Eq. (7), we find for the time dependence of the phase difference during the switching process

$$\delta_{\text{on}} = \delta_0 - \frac{D}{1 + C e^{-2t/\tau_{\text{on}}}}, \quad (18)$$

$$\delta_{\text{off}} = \delta_0 - D e^{-2t/\tau_{\text{off}}}. \quad (19)$$

Here, $D = \delta_2 \theta_f^2$ is the total change of the phase difference and $C = \theta_f^2/\theta_i^2 - 1$. By fitting Eqs. (18) and (19) to the measured data, the time constants τ_{on} and τ_{off} can be determined.

B. Results

In order to measure the transmittance of the samples after a sudden voltage switch, images were captured at well defined time intervals and the light intensity was calculated from the gray levels of the images. Due to the spatially inhomogeneous transition, the intensity was analyzed at 1000 random locations for each time step. In order to reduce noise, the intensity at each location was averaged over an area of 3×3 pixels, which is much smaller than the typical size of the domains observed. Typical time dependencies of the transmitted light intensity $I(t)$ and the resulting phase difference $\delta(t)$ at one such location are shown in Fig. 6 for pure 5CB and for samples with a concentration of the block copolymer of 1.1% and 2.1%. The voltage has been switched from a subcritical to a slightly supercritical value between $U_{\text{on}} = 0.85$ and 1 V, depending on the time scale of the experiment. We show here the phase

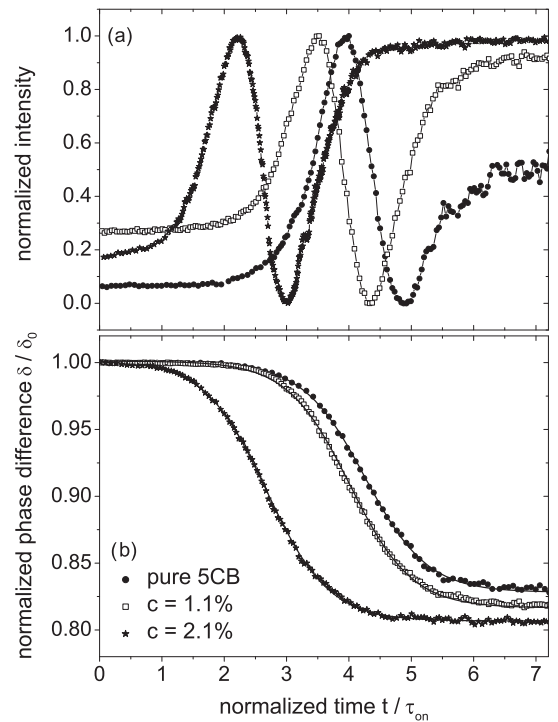


FIG. 6. Typical time dependencies of (a) the transmitted light intensity I and (b) the phase difference δ for pure 5CB and for samples with block copolymer concentrations of 1.1% and of 2.1%. The solid lines in (b) are fits of Eq. (18) to the experimental data.

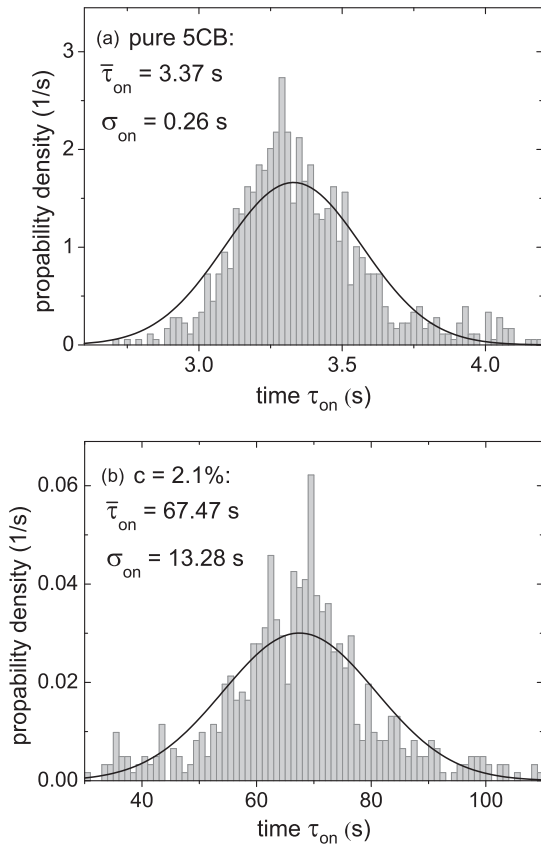


FIG. 7. Histograms of the τ_{on} distribution over the sample area (a) for pure 5CB and (b) for a block copolymer concentration of 2.1%. $\bar{\tau}_{\text{on}}$ is the mean value obtained from fitting a normal distribution (solid line) and σ_{on} is the respective standard deviation.

difference normalized with the value corresponding to the undistorted planar state δ_0 in order to avoid different starting levels of the curves due to slightly different cell thicknesses. The solid lines are obtained by using a nonlinear fitting procedure for Eq. (18), thus yielding τ_{on} as a fit parameter. In a similar procedure, Eq. (19) was fitted to the data obtained when switching off the voltage from a supercritical value, which gives τ_{off} .

For each of the 1000 areas, the phase difference was calculated and fitted as just explained, so that τ_{on} and τ_{off} were obtained for each small area of the sample. From histograms of these data, the mean value and its standard deviation was derived by fitting a normal distribution. Typical distributions of the “on” times τ_{on} are shown in Fig. 7(a) for pure 5CB and in Fig. 7(b) for a block copolymer solution with $c = 2.1\%$. The solid lines are fits of a normal distribution, which is typical for all our samples. It should be noted that for the “off” process, the distribution is narrower, while increasing the polymer concentration leads to a wider distribution. Since we can not assess the statistical independence of the sample areas chosen for evaluation, we characterize the uncertainties of the averaged time constants by twice the corresponding standard deviation. Thus, the bars in the following figures [except Fig. 8(a)] are not usual error bars but rather a measure for the distribution of the values in our measurements.

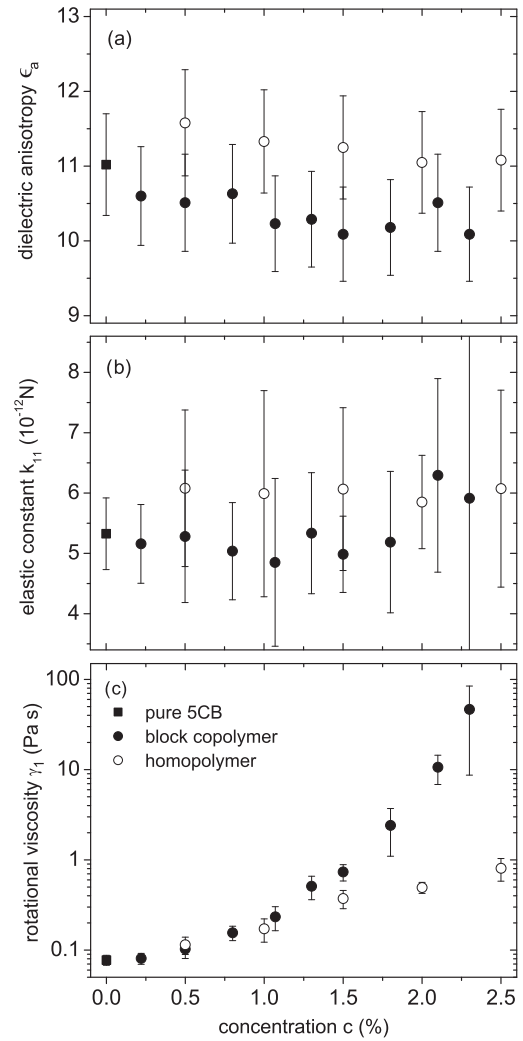


FIG. 8. As functions of the polymer concentration c are shown (a) the dielectric anisotropy ϵ_a , (b) the splay elastic constant k_{11} , and (c) the rotational viscosity γ_1 . In (b) and (c) and in the following figures, the vertical bars represent the distribution of the values within our samples.

The dielectric anisotropy ϵ_a was measured as described in Sec. II B, with the results being shown in Fig. 8(a). ϵ_a remains constant for solutions with block copolymer mass concentrations up to 4%. For the homopolymer solutions, the dielectric anisotropy is slightly larger by about 0.8 compared to the block copolymer solution. Using Eqs. (16) and (17), the splay elastic constant k_{11} and the rotational viscosity γ_1 have been calculated for all samples. The results are shown in Figs. 8(b) and 8(c). The results for γ_1 are also listed in Table I. Obviously, the splay elastic constant k_{11} of the system remains essentially the same over this concentration range. On the other hand, the rotational viscosity increases rapidly with increasing block copolymer concentration, but less pronounced for the homopolymer solutions. For pure 5CB, we measured the values $\epsilon_a = 11$, $k_{11} = 5.3 \times 10^{-12}$ N and $\gamma_1 = 0.08$ Pa s, which are comparable with the literature data [41,42].

TABLE I. Measured rotational viscosity γ_1 with the corresponding standard deviation 2σ for all polymer samples. For pure 5CB, we found $\gamma_1 = 0.078$ Pa s with $2\sigma = 0.010$ Pa s.

c (%)	Block copolymer		c (%)	Homopolymer	
	γ_1 (Pa s)	2σ (Pa s)		γ_1 (Pa s)	2σ (Pa s)
0.2	0.081	0.011	0.5	0.114	0.025
0.5	0.10	0.02	1.0	0.17	0.05
0.8	0.16	0.03	1.5	0.37	0.09
1.1	0.23	0.07	2.0	0.49	0.07
1.3	0.51	0.15	2.5	0.81	0.23
1.5	0.73	0.15			
1.8	2.4	1.3			
2.1	11	3.8			
2.3	47	38			

V. DISCUSSION AND INTERPRETATION

We have found that the cells with mesogenic side-chain block copolymer and homopolymer solutions in 5CB with mass concentrations c up to 2.5% are well aligned and behave like usual nematics. The anisotropy of the dielectric permittivity ϵ_a and the splay elastic constant k_{11} of the solutions do not exhibit any pronounced dependence on concentration within the accuracy of the measurements [see Figs. 8(a) and 8(b)]. Note that for solutions of a different side-chain polymer in 5CB, which do not demonstrate a gel state at high concentrations similar to our homopolymer solutions, the bend elastic constant k_{33} was also found to be independent of the polymer concentration [18]. Nevertheless, the large scatter of the values of k_{11} for the block copolymer solutions especially at higher concentrations already indicates that their elastic properties can be very different from the corresponding homopolymer solutions.

Compared to the elastic properties, the dynamic response characterized by the rotational viscosity γ_1 was found to be much more influenced by the addition of the polymer: γ_1 is increased by a factor of about 500 for a block copolymer concentration of $c = 2.3\%$ and by a factor of about 10 for a homopolymer concentration of $c = 2.5\%$. For concentrations below 1%, the rotational viscosities γ_1^c and γ_1^h for the block copolymer and for the homopolymer, respectively, are increased with c and their values are almost the same. We conclude that the presence of short end blocks in the block copolymer chains in comparison with the homopolymer chains does not influence the rotational viscosity of the solution at low concentrations.

Our most intriguing result is a different concentration dependence of γ_1^c and γ_1^h for solutions with $c > 1\%$, where γ_1^c starts to increase sharply [see Fig. 8(c)]. Note, that, according to rheological measurements and observations in the block copolymer solutions, a fully gelified state is formed for concentrations above $c \approx 3\%$. As already mentioned in Sec. II A, at such concentrations of the ABA-triblock copolymer with polystyrene end blocks (A) and a long middle block (B) with attached mesogenes, a physical network (physical gel) is formed due to the end block interactions [9]. In the nematic phase of 5CB, the end blocks are aggregated in micelles leading to “junctions” between the individual block copolymer

chains. The homopolymer does not have the polystyrene end blocks and its solutions do not demonstrate the formation of a network.

The increase of the rotational viscosity with concentration can be interpreted in the framework of the Brochard theory for the dynamics of polymer chains in a nematic solvent [15]. This model has been developed for diluted polymer solutions where the polymer chains can be considered as independent, neglecting any interactions between them. The increase of the rotational viscosity $\delta\gamma_1 = \gamma_1(c) - \gamma_1(0)$ with the polymer concentration is given by [15]

$$\delta\gamma_1 = \frac{c_m}{N} k_B T \tau_R \frac{[1 - (R_{\parallel}/R_{\perp})^2]^2}{(R_{\parallel}/R_{\perp})^2}. \quad (20)$$

Here, c_m is the monomer concentration (the number of monomers per unit volume) and directly proportional to the polymer concentration, N is the degree of polymerization, k_B is the Boltzmann constant, T is the temperature, τ_R is the rotational relaxation time of the polymer chain, and R_{\parallel} , R_{\perp} are the chain dimensions parallel and perpendicular to the director, respectively, which characterize the anisotropy of the chain shape (aspect ratio). Note that, in the case of an isotropic chain shape ($R_{\parallel} = R_{\perp}$), the rotational viscosity of the polymer solution is independent of the polymer concentration. This is in distinct contrast to “hydrodynamic” viscosities (Miesowicz coefficients) determined from shear flow experiments, where the coefficients are proportional to the polymer concentration for any chain shape [14,15]. It has been shown that, for the case of $R_{\parallel} \approx R_{\perp}$, a modification of the Brochard theory by including an additional coupling between the side-chain mesogens of the side-chain liquid crystalline polymers with the nematic solvent leads to an improved agreement with experiments [19,20].

The rotational relaxation time of the polymer chain, τ_R , is given as a combination of two relaxation times associated with motions of the chain parallel and perpendicular to the director

$$\tau_R = \tau_{\perp} \frac{\tau_{\parallel}/\tau_{\perp}}{1 + \tau_{\parallel}/\tau_{\perp}}, \quad (21)$$

with

$$\tau_{\parallel} = \frac{\lambda_{\parallel}}{k_B T} R_{\parallel}^2, \quad \tau_{\perp} = \frac{\lambda_{\perp}}{k_B T} R_{\perp}^2. \quad (22)$$

Here, λ_{\parallel} , λ_{\perp} are the friction coefficients of the polymer chain parallel and perpendicular to the director, respectively. There are two limiting cases for λ_{\parallel} and λ_{\perp} [15,43]. In the free draining limit (a flexible chain freely penetrable by the solvent), one has

$$\lambda_{\parallel} = N z_{\parallel}, \quad \lambda_{\perp} = N z_{\perp}, \quad (23)$$

where z_{\parallel} and z_{\perp} are the monomer friction coefficients in the directions parallel and perpendicular to the director, respectively. In the nondraining limit, corresponding to the approximation of a polymer chain by a rigid sphere impenetrable by the solvent, the friction coefficients are given by

$$\lambda_{\parallel} \propto R_{\parallel}, \quad \lambda_{\perp} \propto R_{\perp}. \quad (24)$$

To summarize, the rotational viscosity increases linearly with the concentration for polymer chains of anisotropic shape

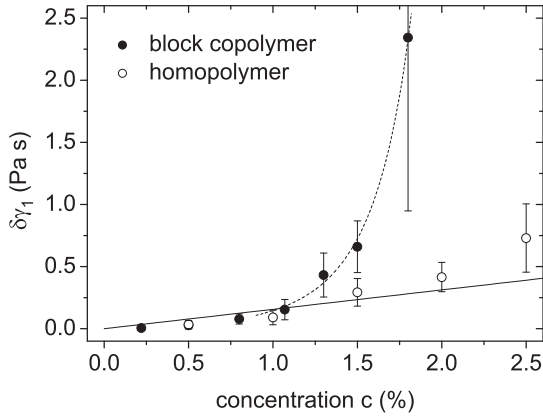


FIG. 9. Increase of the rotational viscosity for the homopolymer ($\delta\gamma_1^h$) and for the block copolymer ($\delta\gamma_1^c$) solutions. The solid line is a linear fit with $\delta\gamma_1^h = 0.156c$, while the dashed line is a guide to the eye.

($R_{\parallel}/R_{\perp} \neq 1$) and $\delta\gamma_1$ depends on the four microscopic parameters R_{\parallel} , R_{\perp} , λ_{\parallel} , and λ_{\perp} . The experimental determination of these parameters is a highly complicated task.

Our results for $\delta\gamma_1(c)$ are shown in Fig. 9. We have found that, for the homopolymer solutions, $\delta\gamma_1^h$ increases almost linearly with concentration for $c < 2\%$. Using the coefficient obtained from a linear fit of $\delta\gamma_1^h$, the rotational relaxation time of the homopolymer chain τ_R can be estimated from Eq. (20). Assuming that the density of the solution is approximately equal to the density ρ of pure 5CB, which should be valid for small concentrations, one has $c_m/N = c\rho N_A/M_n$, where N_A is the Avogadro constant and M_n is the molecular mass of the homopolymer. Taking for the geometrical factor in Eq. (20) the value $[1 - (R_{\parallel}/R_{\perp})^2]^2/(R_{\parallel}/R_{\perp})^2 \approx 1$, which corresponds to $R_{\parallel}/R_{\perp} \approx 0.6$ as found in Ref. [12], we find $\tau_R \approx 0.01$ s. For higher concentrations, $\delta\gamma_1^h$ starts to deviate from the predictions of the Brochard theory. Unfortunately, a theory for the next order corrections ($\propto c^2$) is unavailable at present.

For $c < 1\%$, the increase of the rotational viscosity of the block copolymer solutions is almost the same as for the homopolymer solutions, while for $c > 1\%$, $\delta\gamma_1^c$ starts to increase much more rapidly than $\delta\gamma_1^h$. We suggest that such a sharp increase of $\delta\gamma_1^c$ compared to $\delta\gamma_1^h$ can be related to the formation and growth of larger chains or clusters consisting of individual block copolymer chains attached through the end blocks. The resulting increase of the effective size of the polymer chains can lead to an additional increase of $\delta\gamma_1^c$, taking into account that in Eq. (20) the “effective” degree of polymerization in a block copolymer solution depends on the concentration. As it was shown in Refs. [9,21], side-chain polymers with a sufficiently large degree of polymerization form an oblate configuration and the aspect ratio $R_{\parallel}/R_{\perp} < 1$ is independent of N . Therefore, both R_{\parallel} and R_{\perp} scale with N in a similar way:

$$R_{\parallel} \propto N^{\beta}, \quad R_{\perp} \propto N^{\beta}, \quad (25)$$

where the value of the exponent β can vary between $1/3$ for a bad solvent and $3/5$ for a good solvent.

For block copolymer concentrations not too close to the gel point, we assume that preferably free end blocks will join,

so that the evolving clusters take the form of almost linear chains without side branches. In this case, the ratio R_{\parallel}/R_{\perp} can be regarded as independent of N , as in the case of side-chain polymers with a large degree of polymerization [9,21]. In other words, we assume that a cluster assembled of multiple chains behaves just like one long chain. According to Eqs. (22)–(25), the ratio $\tau_{\parallel}/\tau_{\perp}$ can also be considered as independent of N . In addition, the aspect ratios R_{\parallel}/R_{\perp} for the block copolymer and for the homopolymer should be the same due to the almost identical chemical structure. Thus, the ratio $\delta\gamma_1^c/\delta\gamma_1^h$ of the change of the rotational viscosity of the block copolymer and the homopolymer solutions can be expressed in terms of the ratio $R_{\perp}^c/R_{\perp}^h = R_{\parallel}^c/R_{\parallel}^h$ of the chain dimensions. In the following, we use R_{\perp}^c/R_{\perp}^h because, in our case, $R_{\perp} > R_{\parallel}$. All other microscopic parameters related to the monomers are canceled out since they are identical for both the block copolymer and the homopolymer, and we find

$$\frac{\delta\gamma_1^c}{\delta\gamma_1^h} = \left(\frac{R_{\perp}^c}{R_{\perp}^h}\right)^{2+\alpha-1/\beta}, \quad (26)$$

where $\alpha = 1/\beta$ corresponds to the free draining limit [see Eq. (23)] and $\alpha = 1$ to the nondraining limit [see Eq. (24)]. Thus, the increase of the ratio $\delta\gamma_1^c/\delta\gamma_1^h$ with concentration yields a measure for the effective size of the attached block copolymer chains in units of a single chain size. This relation is still valid when taking into account the correction to the Brochard model as proposed in Ref. [19].

The fully gelified state of the block copolymer solution occurs above $c \approx 3\%$. Below this point, the value of R_{\perp}^c/R_{\perp}^h should obey a scaling law [44,45]

$$\frac{R_{\perp}^c}{R_{\perp}^h} \propto (c_{\text{gel}} - c)^{-\nu}, \quad (27)$$

where c_{gel} is the critical concentration when the fraction of the solution is equal to the fraction of the gel (sol-gel transition) and ν is the critical exponent. Although the exponent ν in Eq. (27) can hardly be related to the appropriate critical exponents that appear in various models of percolation theory of chemical gels [1,44,45], the scaling behavior should nevertheless hold.

Using Eqs. (26) and (27), we fitted the experimental ratio $\delta\gamma_1^c/\delta\gamma_1^h$ as

$$\frac{\delta\gamma_1^c}{\delta\gamma_1^h} = a(c_{\text{gel}} - c)^{-b}. \quad (28)$$

For the data of $\delta\gamma_1^c(c)$ at a given c , interpolated values of $\delta\gamma_1^h$ were used to find the desired ratio. Our results as a function of the block copolymer concentration are shown in Fig. 10 together with the fit. From the fitting procedure, we find

$$c_{\text{gel}} = 2.7\% \quad \text{and} \quad b = \nu(2 + \alpha - 1/\beta) = 3.45. \quad (29)$$

Up to now, no assumption has been made on the draining behavior and on the solubility of the polymer chains in the solvent.

Since the mesogenic side-chain moieties of the block copolymer are structurally similar to 5CB, and the middle block is soluble in the nematic phase as well as in the isotropic phase of 5CB, it is quite reasonable to suggest that we are dealing with flexible polymer chains in a good solvent. Then,

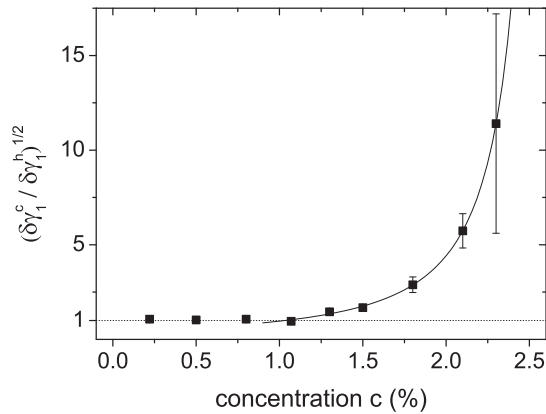


FIG. 10. Dependence of $(\delta\gamma_1^c/\delta\gamma_1^h)^{1/2}$ and, thus, R_{\perp}^c/R_{\perp}^h on the block copolymer concentration c . The solid line is obtained by fitting Eq. (28) to the data above $c = 1\%$.

the properties of such chains should be close to the free draining limiting case where $\alpha = 1/\beta$. This yields $\nu = 1.7$ for the critical exponent. The values of $(\delta\gamma_1^c/\delta\gamma_1^h)^{1/2}$ should then give the measure for the effective size of the attached block copolymer chains in units of a single chain size R_{\perp}^c/R_{\perp}^h [see Eq. (26) for $\alpha = 1/\beta$]. The values of $(\delta\gamma_1^c/\delta\gamma_1^h)^{1/2} = R_{\perp}^c/R_{\perp}^h$ look quite plausible, indicating that, for $c > 1\%$, the block copolymer chains start to join and the effective size of the chains increases by up to 10 individual chain sizes at the highest concentration that has been studied.

Most importantly, the value for the critical concentration $c_{\text{gel}} = 2.7\%$ for the sol-gel transition obtained from Eq. (28) is independent of the chain model and is very close to the concentration $c \approx 3\%$, above which the fully gelified state was identified from rheological measurements [35]. Note that the value of c_{gel} obtained from fitting the experimental data by Eq. (28) is less sensitive to the accuracy of the measurements of $\delta\gamma_1^c$, $\delta\gamma_1^h$ than the value of b . Thus, the scaling behavior of the rotational viscosity can be useful to determine the critical concentration for the sol-gel transition.

VI. SUMMARY AND CONCLUSION

We found that, for the homopolymer solutions, which do not form a gel state, the splay elastic constant k_{11} remains constant. In the case of the block copolymer solutions, we found a large scatter of k_{11} when approaching the gel point, so that we can not assert unambiguously that the elasticity changes. However, the coupling between the reorientation of the director and the elastic deformations of the polymer

network clusters can lead to an effective renormalization of the elastic properties of the solution. The characterization of the interplay between the elastic properties of the polymer network and the nematic liquid crystal in the fully gelified state is a key question for the application of various theoretical models to liquid crystalline gels [46,47]. Thus, more accurate measurements of the dependencies of all three elastic constants on the polymer concentration could be useful to identify the anisotropy of the interactions between the liquid crystal and the network clusters forming near the gel point.

The most significant difference in the behavior of the block copolymer and the homopolymer solutions has been found in their dynamical properties characterized by the rotational viscosity γ_1 . For small concentrations $c < 1\%$, the rotational viscosities of both solutions increase with c and are almost equal to each other. For larger concentrations $c > 1\%$, however, the rotational viscosity of the block copolymer solutions sharply increases and tends to diverge, while γ_1 for the homopolymer solutions exhibits an almost linear dependence on c . Comparing the results obtained for both solutions, we were able to attribute the critical scaling-law behavior of the rotational viscosity of the block copolymer solutions with the formation of network clusters when approaching the gel point. The critical concentration of the block copolymer for the sol-gel transition obtained from the rotational viscosity data is very close to the value found from rheological measurements. Thus, the dynamic Fréedericksz transition technique can serve as an alternative approach for the determination of the critical concentration and has apparent advantages in comparison with rheological and dynamic light scattering measurements. We have also estimated the dependence of the effective cluster size on the block copolymer concentration. In principle, combining these results with the measurements of the flow-alignment angle or the Miesowicz viscosities would allow us to determine in addition the shape anisotropy of the clusters. The information about the cluster size growth with polymer concentration and their shape anisotropy is of great importance to understand the structure of the network formed in the gel state, and also to validate the relevant models for the sol-gel transition.

ACKNOWLEDGMENTS

We gratefully acknowledge the financial support of the Deutsche Forschungsgemeinschaft (DFG), FOR608, project ‘‘Thermoreversible liquid crystalline gels under the influence of electric fields’’. One of us (M.Kh.) wishes to thank the University of Bayreuth for its kind hospitality.

-
- [1] J. E. Martin and D. Adolf, *Annu. Rev. Phys. Chem.* **42**, 311 (1991).
 - [2] K. Almdal, J. Dyre, S. Hvidt, and O. Kramer, *Polym. Gels Networks* **1**, 5 (1993).
 - [3] P. G. de Gennes and J. Prost, *The Physics of Liquid Crystals* (Clarendon, Oxford, 1993).
 - [4] T. Kato, Y. Hirai, S. Nakaso, and M. Moriyama, *Chem. Soc. Rev.* **36**, 1857 (2007).
 - [5] K. Urayama, *Macromolecules* **40**, 2277 (2007).
 - [6] R. Zentel, *Liq. Cryst.* **1**, 589 (1986).
 - [7] Y. Yusuf, J. H. Huh, P. E. Cladis, H. R. Brand, H. Finkelmann, and S. Kai, *Phys. Rev. E* **71**, 061702 (2005).
 - [8] R. Pelrine, R. Kornbluh, Q. Pei, and J. Joseph, *Science* **287**, 836 (2000).
 - [9] M. D. Kempe, N. R. Scruggs, R. Verduzco, J. Lal, and J. A. Kornfield, *Nat. Mater.* **3**, 177 (2004).

- [10] K. Kajiwara, S. Kohjiya, M. Shibayama, and H. Urakawa, in *Polymer Gels*, edited by D. DeRossi, K. Kajiwara, Y. Osada, and A. Yamauchi (Plenum Press, New York, 1991), p. 3.
- [11] M. H. Li, P. Keller, J. Yang, and P. A. Albouy, *Adv. Mater.* **16**, 1922 (2004).
- [12] M. D. Kempe, R. Verduzco, N. R. Scruggs, and J. A. Kornfield, *Soft Matter* **2**, 422 (2006).
- [13] R. Verduzco, N. R. Scruggs, S. Sprunt, P. Palfy-Muhoray, and J. A. Kornfield, *Soft Matter* **3**, 993 (2007).
- [14] A. Jamieson, *Prog. Polym. Sci.* **21**, 981 (1996).
- [15] F. Brochard, *J. Polym. Sci., Polym. Phys. Ed.* **17**, 1367 (1979).
- [16] X. J. Wang and M. Warner, *J. Phys. A: Math Gen.* **20**, 713 (1987).
- [17] A. Matsuyama and Y. Kushibe, *J. Chem. Phys.* **132**, 104903 (2010).
- [18] E. E. Pashkovsky and T. G. Litvina, *Macromolecules* **28**, 1818 (1995).
- [19] N. Yao and A. M. Jamieson, *Macromolecules* **31**, 5399 (1998).
- [20] P.-Y. Liu, N. Yao, and A. M. Jamieson, *Macromolecules* **32**, 6587 (1999).
- [21] M. D. Kempe, J. A. Kornfield, and J. Lal, *Macromolecules* **37**, 8730 (2004).
- [22] D. F. Gu and A. M. Jamieson, *Macromolecules* **27**, 337 (1994).
- [23] M. D. Kempe and J. A. Kornfield, *Phys. Rev. Lett.* **90**, 115501 (2003).
- [24] P. Pieranski, F. Brochard, and E. Guyon, *Le J. de Phys.* **33**, 681 (1972).
- [25] P. Pieranski, F. Brochard, and E. Guyon, *Le J. de Phys.* **34**, 35 (1973).
- [26] F.-L. Chen, A. M. Jamieson, M. Kawasumi, and V. Percec, *J. Polym. Sci., Part B: Polym. Phys.* **33**, 1213 (1995).
- [27] C. C. Chang, L. C. Chien, and R. B. Meyer, *Phys. Rev. E* **56**, 595 (1997).
- [28] A. de Lózar, W. Schöpf, I. Rehberg, O. Lafuente, and G. Lattermann, *Phys. Rev. E* **71**, 051707 (2005).
- [29] M. Müller, W. Schöpf, I. Rehberg, A. Timme, and G. Lattermann, *Phys. Rev. E* **76**, 061701 (2007).
- [30] J. Adams and W. Gronski, *Makromol. Chem., Rapid Commun.* **10**, 553 (1989).
- [31] G. Mao, J. Wang, S. R. Clingman, C. K. Ober, J. T. Chen, and E. L. Thomas, *Macromolecules* **30**, 2556 (1997).
- [32] C. Frenz, A. Fuchs, H.-W. Schmidt, U. Theissen, and D. Haarer, *Macromol. Chem. Phys.* **205**, 1246 (2004).
- [33] T. Breiner, K. Kreger, R. Hagen, M. Haeckel, L. Kador, A. H. E. Mueller, E. J. Kramer, and H.-W. Schmidt, *Macromolecules* **40**, 2100 (2007).
- [34] See Supplemental Material at <http://link.aps.org/supplemental/10.1103/PhysRevE.84.021710> for details regarding the synthesis and characterization of the block copolymer and of the respective homopolymer.
- [35] R. Pettau *et al.* (unpublished).
- [36] H. Mada and S. Kobayashi, *Mol. Cryst. Liq. Cryst.* **33**, 47 (1976).
- [37] I. Rehberg, B. L. Winkler, M. de la Torre Juárez, S. Rasenat, and W. Schöpf, *Adv. Solid State Phys.* **29**, 35 (1989).
- [38] A. de Lózar, W. Schöpf, I. Rehberg, Ó. Lafuente, and G. Lattermann, *Phys. Rev. E* **71**, 051707 (2005).
- [39] A. Bogi and S. Faetti, *Liq. Cryst.* **28**, 729 (2001).
- [40] S. A. Pikin, *Structural Transformations in Liquid Crystals*, 1st ed. (Gordon and Breach, New York, 1991).
- [41] L. M. Blinov and V. G. Chigrinov, *Electrooptic Effects in Liquid Crystal Materials* (Springer, New York, 1994).
- [42] G. Ahlers, in *Pattern Formation in Liquid Crystals*, edited by A. Buka and L. Kramer (Springer, New York, 1996), p. 127.
- [43] W. Graessley, *Polymeric Liquids & Networks: Dynamics and Rheology* (Garland Science, London, 2008).
- [44] D. Stauffer, *Phys. Rep.* **54**, 1 (1979).
- [45] P. G. De Gennes, *Scaling Concepts in Polymer Physics*, 1st ed. (Cornell University Press, Ithaca, NY, 1980).
- [46] M. Warner and E. Terentjev, *Liquid Crystal Elastomers* (Oxford University Press, Oxford, 2003).
- [47] H. Brand, H. Pleiner, and P. Martinoty, *Soft Matter* **2**, 182 (2006).

2.2 Structure-Property Relations of Liquid Crystalline Gels with ABA-Triblock Copolymers as Gelators

Authors: Robin Pettau, Thomas Müller, Maxim Khazimullin, Ingo Rehberg, and Hans-Werner Schmidt

Journal: Zeitschrift für Physikalische Chemie

Volume: 226

Pages: 645–664

Date of publication: August 13, 2012

DOI: <http://dx.doi.org/10.1524/zpch.2012.0284>

© 2012 Oldenbourg Wissenschaftsverlag, München

Structure-Property Relations of Liquid Crystalline Gels with ABA-Triblock Copolymers as Gelators

By Robin Pettau¹, Thomas Müller², Maxim Khazimullin³, Ingo Rehberg², and Hans-Werner Schmidt^{1,4,*}

¹ Macromolecular Chemistry I, University of Bayreuth, 95440 Bayreuth, Germany

² Experimental Physics V, University of Bayreuth, 95440 Bayreuth, Germany

³ Institute of Physics of Molecules and Crystals, Ufa Research Center, Russian Academy of Science, Ufa, Russia

⁴ Bayreuth Institute of Macromolecular Research and Bayreuth Center for Colloids and Interfaces, University of Bayreuth, 95440 Bayreuth, Germany

Dedicated to Matthias Ballauff on the occasion of his 60th birthday

(Received June 1, 2012; accepted in revised form July 15, 2012)

(Published online August 13, 2012)

Block Copolymer Gelator / Liquid Crystalline Gel / Rheology / Electro-Optical Response

This paper reports on the influence of the structure of tailored ABA-triblock copolymers on physical gelation of the nematic liquid crystal 4'-n-pentyl-4-cyanobiphenyl (5CB), rheological properties, and the electro-optical response of the gels. The block copolymer gelators, comprised of two polystyrene A-blocks connected to a cyanobiphenyl-functionalized polyhydroxystyrene B-block, were synthesized by living anionic polymerization and functionalized by polymer analogous reactions. These block copolymers feature selective solubility. The B-block is soluble in the nematic and isotropic state of 5CB, whereas the polystyrene A-blocks are only soluble in the isotropic state. Consequently, upon cooling liquid crystalline gels are formed due to the controlled microphase-separation of the A-blocks. We show that the polymer composition and the different block lengths are important to vary the gel properties and the electro-optical response. It is confirmed that the gel formation correlates to the isotropic to nematic transition of 5CB for block copolymer gelators with sufficiently long A-blocks. Higher gel elasticity is obtained if gelators with short B-blocks are employed. The influence of the polymer network on the switching behavior of these liquid crystalline gels is investigated with respect to the electro-optical response in light scattering experiments. Intriguingly, these indicate a rearrangement of the nodes formed by the A-blocks under a strong electric field for block copolymers with short A-blocks.

1. Introduction

In his early work, Matthias Ballauff investigated mixtures of thermotropic nematics and flexible, non liquid crystalline polymers [1–4]. While isotropic polymers may be

* Corresponding author. E-mail: hans-werner.schmidt@uni-bayreuth.de

soluble in the isotropic state of low molecular weight liquid crystals (LC), their dissolution in the liquid crystalline phase is generally unfavorable because of the associated loss of configurational entropy. Consequently, upon cooling such binary systems from the isotropic state into the nematic state, the LC component expels the coiled polymer with very high efficiency. Ballauff extended Flory's lattice model [5–10] to successfully describe the phase behavior of polymer/LC mixtures, predicting a widening of the biphasic region in their phase diagram with increasing polymer chain length [1]. Later on, he further studied the strong demixing tendency that arises upon formation of an ordered phase for the swelling equilibria of isotropic polymer networks in nematic solvents [3]. While the network can be swollen with liquid crystal in the isotropic state in a linear fashion, the swelling curve exhibits a strong anomaly at the nematic to isotropic transition temperature (T_{ni}). Similar to isotropic polymers, below T_{ni} the network shrinks by continuously expelling the nematic solvent and at temperatures far below T_{ni} nearly reaches the dimensions of the dry network [4].

In contrast to flexible, non liquid crystalline polymers, side-group liquid crystalline polymers can be soluble in the isotropic state as well as in the nematic state of a liquid crystalline solvent, as firstly reported by Ringsdorf *et al.* [11]. High similarity of the chemical structures of the mesogenic side-groups of these polymers and the liquid crystalline solvent ensures compatibility resulting in a complete miscibility in the nematic phase. Subtle structural changes can lead to an incomplete miscibility with co-existence of two nematic phases. In this biphasic system the selective addressing of the low molecular weight liquid crystal is possible [11].

In general, block copolymers are capable of featuring the properties of the respective homopolymers. AB-block copolymers comprising a flexible A-block and a liquid crystalline B-block were first reported by Adams and Gronski [12]. Later on, Finkelmann *et al.* have shown that the block copolymer segment containing the mesogenic moieties feature a selective solubility in the low molecular weight liquid crystals, whereas the isotropic block is not soluble in the LC solvent [13]. As a result, the flexible segments of an AB-diblock copolymer associate and form a micelle core that is surrounded by a corona of soluble liquid crystalline blocks [14–16].

Extending this concept to ABA-triblock copolymers, Kornfield *et al.* demonstrated that these polymers are suited as gelators for low molecular weight liquid crystals. This ABA-triblock copolymer system was based on two polystyrene A-blocks and a B-block based on poly(1,2-butadiene) functionalized with mesogene side-groups. Above a critical concentration of the polymer in the LC solvent, physical gelation was achieved by the microphase-separation of the poorly soluble A-blocks [17–19].

In detail, in a liquid crystalline solvent, the B-segments of the ABA-triblock copolymers are assumed to adopt different conformations depending on the polymer concentration. At low concentration mostly flower-like conformations exist, in which the B-chains form loops with both of the linked A-blocks located in the same aggregate. At higher concentration, the B-segments can additionally form a bridge conformation where the respective A-blocks are incorporated in two different aggregates (see Fig. 1) [17]. Only the latter configuration contributes to the formation of a physical, space filling network that results in the gelation of the solvent. Hence, the length of the A-block is thought to determine the diameter of the nodes while the length of the B-chain determines the maximal distance between them and, thus, the network span.

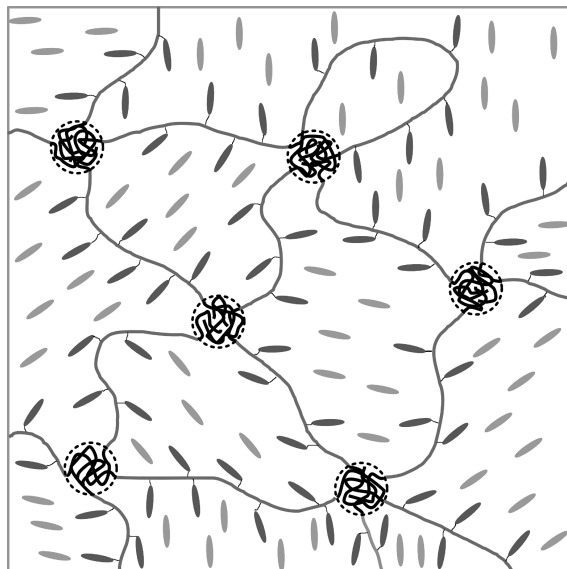


Fig. 1. Schematic representation of the polydomain gel of a liquid crystal with an ABA-triblock copolymer. The phase-separated, insoluble A-blocks form crosslinks while the soluble, mesogenic B-segments form bridges.

These liquid crystalline gels are functional soft materials that combine the soft solid state with stimuli-responsive properties. Up to now, most studies have been conducted on LC gels obtained by the self-assembly of fibrous solid networks of low molecular weight gelators [20]. It has been demonstrated that in such gels the electro-optical response can be influenced by the elastic interaction between the liquid crystalline solvent and the polymer network; hence, they can show faster responses in twisted nematic mode than the respective neat liquid crystals [20]. These gels also have potential as elements in a light scattering electro-optical switching display medium because of the effective formation of LC polydomains resulting in high contrast switching in light scattering mode [16]. The contrast between the scattering intensity with or without an applied electric field as well as the critical voltage was shown to depend on the structure of the gelating network in this type of electro-optical element [21].

Recently, we have demonstrated that the rotational viscosity of a liquid crystal in mixtures with ABA-triblock copolymers can be used to detect and characterize the aggregation of the A-block and to determine the critical gelator concentration [22]. However, less is known about the influence of the gelator on the properties of liquid crystalline gels formed by ABA-triblock copolymers.

Here we present a comprehensive study on the influence of the polymer backbone of ABA-triblock copolymers on their gelation properties for the low molecular weight liquid crystal 4'-n-pentyl-4-cyanobiphenyl (5CB). This investigation uses a polymer system comprised of two polystyrene A-blocks and a B-block based on poly(4-hydroxystyrene) functionalized with 4-cyanobiphenyl moieties. We employ a series of ABA-triblock copolymers featuring distinct variations. This includes the

length of the B-block containing mesogenic side-groups, the lengths of the A-blocks, and the polymer architecture. Gel properties were characterized by means of rheological and light scattering experiments to reveal structure-property relations with respect to these variations.

2. Experimental part

2.1 Materials

The block copolymer backbones **1–5** were synthesized by anionic polymerization. Functionalization with cyanobiphenyl moieties was performed in a subsequent polymer analogous reaction resulting in the block copolymer gelators **1a–5a**. The synthesis was conducted according to [22]. Further details can be found in the supporting material.

5CB/polymer mixtures were prepared by weighing 5CB and the respective amount of polymer in a 1 ml vial. Homogenization was achieved by rotating the closed vial in a tumble mixer at 50 °C for 48 h.

2.2 Methods

Oscillatory rheological measurements were performed on an Anton-Paar MCR301 rheometer using a cone-plate geometry with a diameter of 50 mm and an angle of 1°. The temperature was adjusted by Peltier devices in the plate. For loading a sample, the plate as well as the sample were heated to 45 °C. The liquid was transferred onto the plate with a syringe and the cone was lowered to the measurement position. For temperature-dependent measurements, a heating/cooling rate of 1 K min⁻¹ was used at a frequency of 1 Hz. All measurements were performed within the linear viscoelastic regime, which was determined by strain dependence measurements of the dynamic shear storage modulus G' and loss modulus G'' . Typically, strain in the range of 0.1 % or 1 % was used depending on the concentration and temperature of the solution.

For *electro-optical measurements*, samples were filled in commercial liquid crystal test cells (E.H.C Co., Ltd Tokyo, Japan) with a cell gap of $d = 22 \mu\text{m} \pm 1 \mu\text{m}$. Except for a 4 mm × 4 mm ITO-layer, for the application of an electric field, the cells had no further inner coating (for example a polyimide coating that forces the orientation of the liquid crystal director). Before filling, samples and empty cells were heated to 50–70 °C for two hours. Subsequently, the cells were filled by capillary forces in the isotropic state and kept at this temperature for another two hours. Finally, the filled cells were slowly cooled down to ambient temperature (with a cooling rate of around 0.01 K min⁻¹ below 35 °C). For samples with **4a** and **5a**, we also prepared cells with a faster cooling. At room temperature, a polydomain structure could be observed for all samples under the microscope, independent of the cooling rate.

After the filling procedure, the test cells were mounted on a thermostage to control the temperature with a water based circulation thermostat (Lauda E300). The temperature was measured with a PT1000 platinum temperature sensor with an accuracy of ± 0.1 K. The thermostage was fixed on a microscope (Olympus, BX41) with an illumination unit of a red LED (LedEngin, LZ4-00R115, wavelength $\lambda = 638$ nm) to

register the electro-optical response of a small area ($\approx 10 \text{ mm}^2$) of the cell. The transmitted intensity I was measured with a photodetector, whose signal was collected with an AD-converter (Labjack UE9) with a sampling rate of 1500 Hz at a resolution of 12 bit.

In preparation for each measurement, the cell was heated up and kept at $60 \text{ }^\circ\text{C}$ for 30 min and the transmitted intensity I_{iso} was recorded in this isotropic state. Consequently it was cooled down to $25 \text{ }^\circ\text{C}$ within 35 min or 15 min, dependent on the desired cooling rate in the anisotropic regime (0.01 K s^{-1} or 0.05 K s^{-1}). This heating and cooling process was done to achieve equal scattering states before each measurement. Next, at $t_{\text{on}} = 0$, a sinusoidal ac voltage U_{on} with a frequency of 1 kHz was applied for a duration of 20 min and the temporal evolution of the transmitted light $I(t_{\text{on}})$ was recorded via the photodetector. Afterwards (at $t_{\text{off}} = 0$) the voltage was switched back to subcritical $U_{\text{off}} = 1 \text{ V}$ and the development of intensity was registered for another 20 min. In the timescales of hours, a voltage of 1 V did not have a detectable influence on the polydomain structure and the transmittance of light and it could therefore be used as a characteristic subcritical value. In order to detect the influence of the strength of the electric field, measurements were conducted in 10 V steps of U_{on} ranging from 40 V to 100 V. As the thickness of our test cells was similar for all of our studies, we are able to compare the behavior of different samples with the same applied electric voltage U_{on} .

3. Results and discussion

3.1 Block copolymer synthesis

In order to investigate the influence of the different block lengths of the functionalized ABA-triblock copolymers on their gelation properties, we synthesized a series of four different, well-defined linear triblock copolymer backbones as well as a star block copolymer by anionic polymerization that were subsequently functionalized with mesogenic side-groups. This general synthetic approach to functional block copolymers combining anionic polymerization with polymer analogous functionalization allows for a high degree of polymerization with a low molecular weight distribution and a good control of the block composition [12,23]. The presented ABA-triblock copolymers are based on a polystyrene-*block*-poly(4-hydroxystyrene)-*block*-polystyrene (PS-PHS-PS) backbone. Poly(4-hydroxystyrene) (PHS) has been selected as backbone for the functionalized middle block because of the relatively high glass transition temperature (T_g) of the resulting functionalized polymer [24]. Furthermore, the phenolic functionality allows for subsequent polymer analogous etherification reactions in addition to the esterification possible with aliphatic alcohols such as hydroborated poly(1,2-dienes) or poly(2-(2-hydroxyethyl methacrylate)) [12,25–27].

Two different routes for the polymerization of the block copolymer backbones were employed. The direct anionic polymerization of 4-hydroxystyrene (HS) is precluded by its phenol group; thus, 4-*tert*-butoxystyrene (*t*BS) was utilized as a protected monomer [28].

In route 1, the ABA-block copolymers **1–3** were prepared using a bifunctional initiator for the anionic polymerization of *t*BS and styrene (S) yielding linear ABA-

Route 1

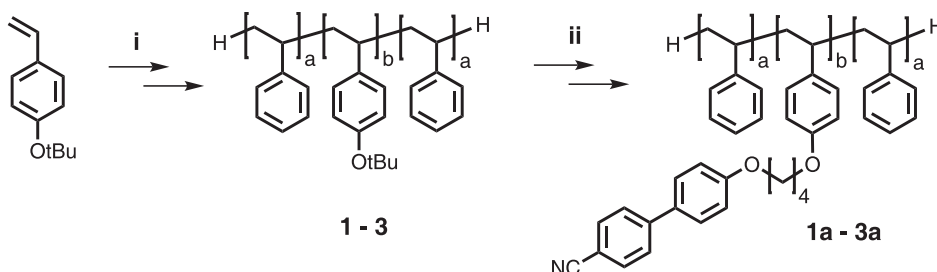


Fig. 2. Synthetic pathways to the cyanobiphenyl-functionalized block copolymers **1a–3a** using route 1. **i:** 1. sodium naphthalene, tetrahydrofuran (THF), $-66\text{ }^{\circ}\text{C}$; 2. styrene, THF, $-66\text{ }^{\circ}\text{C}$; 3. MeOH. **ii:** 1. HCl, THF, $66\text{ }^{\circ}\text{C}$; 2. 4'-(4-bromobutoxy)biphenyl-4-carbonitrile, K_2CO_3 , KI, 18-crown-6, dimethylformamide (DMF), $110\text{ }^{\circ}\text{C}$.

triblock copolymers containing a central functionalizable poly(*tert*-butoxystyrene) (PtBS) B-block linked to polystyrene A-blocks, with variations regarding the lengths of A- and B-blocks (see Fig. 2). Advantageously, this route results in symmetrical ABA-triblock copolymers that intrinsically feature identical lengths of both A-blocks.

In route 2, a monofunctional anionic initiator was used for the sequential polymerization of S, tBS, and S resulting in the linear ABA'-block copolymer **4** (see Fig. 3). Due to the subsequent polymerization, the A- and A'-blocks are not identical. However, this route offers the possibility to employ coupling agents in order to modify the architecture of the resulting block copolymer. In this case, after the complete polymerization of the last block, we used silicon tetrachloride yielding the star block copolymer backbone **5**.

To ensure the selective solubility of the middle block of the triblock copolymers **1–5** in the nematic liquid crystal 5CB, the B-block was functionalized with cyanobiphenyl (CB) moieties. These moieties were chosen because of their structural similarity to the solvent. The *tert*-butoxy protection groups of the block copolymers **1–5** were cleaved under acidic conditions prior to the functionalization. Subsequently, the CB moieties were attached to the backbone via a flexible alkyl spacer in a polymer analogous Williamson etherification reaction yielding the block copolymers **1a–5a**. Characteristic data of precursors **1–3** and the functionalized block copolymers **1a–3a** are given in Table 1 and for the precursors **4, 5** prepared via route 2 and their respective functionalized block copolymers **4a, 5a** in Table 2.

In this series, the molecular weight with respect to polystyrene standards of the functionalized block copolymers ranges from 630 kg mol^{-1} (**4a**) to 2107 kg mol^{-1} (**3a**) while the degree of conversion (DC) of the polymer analogous functionalization is between 75 % (**5a**) and 88 % (**1a**). The repeating units (ru) of the B-block range from $\text{ru}_B \approx 680$ (**4a**) to $\text{ru}_B \approx 2670$ (**3a**). **1a** and **4a** have the lowest overall molecular weight in the series and shortest B-block lengths (**1a**: $\text{ru}_B \approx 930$; **4a**: $\text{ru}_B \approx 680$). The length of the A-blocks decreases with increasing number of the polymer (**1a, 2a, 3a, 4a**) from $\text{ru}_A \approx 490$ (**1a**) to $\text{ru}_A \approx 120, 190$ (**4a**). **4a** also forms each of the arms (*y*) in the star block copolymer **5a**, that is a mixture of $y = 1$: 25 %, $y = 2$: 35 % and $y = 3$: 40 %. The mass percentage of the PS in the block copolymers ranges from 24 % (**1a**) to 8 % (**3a**),

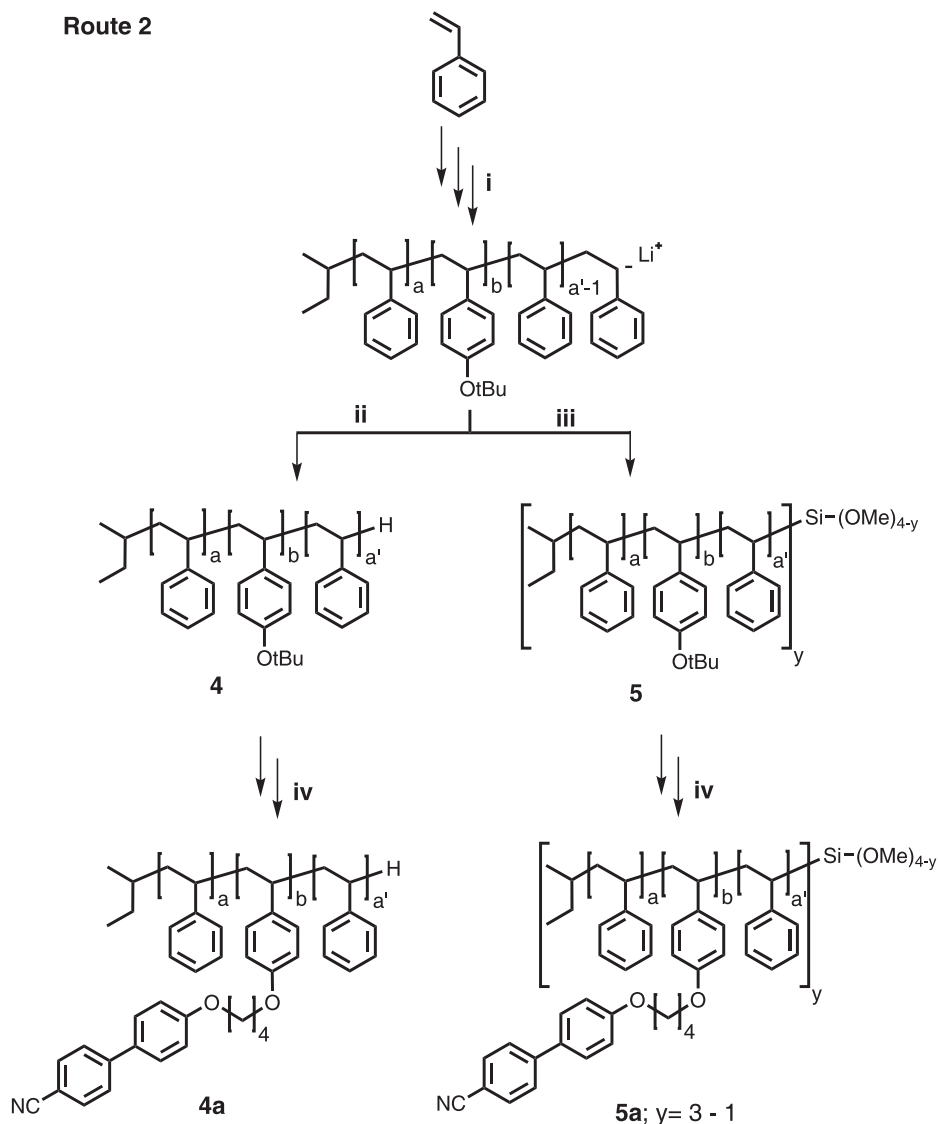


Fig. 3. Synthetic pathways to the cyanobiphenyl-functionalized block copolymers **4a** and **5a** using route 2. **i**: 1. *sec*-butyllithium, THF, -66°C ; 2. *tert*-butoxystyrene, THF, -66°C ; 3. styrene, THF, -66°C . **ii**: MeOH. **iii**: 1. silicon tetrachloride, THF, -60°C ; 2. MeOH. **iv**: 1. HCl, THF, 66°C ; 2. 4-(4-bromobutoxy)biphenyl-4-carbonitrile, K₂CO₃, KI, 18-crown-6, dimethylformamide (DMF), 110°C .

whereas **2a**, **4a** and **5a** have virtually the same PS weight fraction with $\sim 14\%$. Differential scanning calorimetry (DSC), polarization optical microscope (POM) and X-ray diffraction (XRD) characterizations were employed to identify potential mesophases, but none of the functionalized block copolymers exhibits an identifiable liquid crystalline phase.

Table 1. Characteristic data of the block copolymers **1a–3a** and their precursors **1–3** prepared via route 1.

Precursor	Block copolymer	M_n^a kg mol ⁻¹	M_w^a	PDI ^b	DC ^c %	w_{CB}^d %	ABA ru _A ^e	ru _B ^e	ru _A ^e
1	–	278	306	1.10	–	–	490	930	490
–	1a	894	947	1.06	88	76	490	930	490
2	–	403	436	1.08	–	–	430	1860	430
–	2a	1409	1713	1.22	78	87	430	1860	430
3	–	528	558	1.06	–	–	360	2670	360
–	3a	1560	2107	1.30	83	92	360	2670	360

^a determined by SEC (eluent: THF (**1–3**)/THF + electrolyte (**1a–3a**)); molecular weight with respect to polystyrene standards, UV-detection; ^b polydispersity index, M_w/M_n ; ^c degree of conversion of polymer analogous reaction, determined by ¹H-NMR; ^d mass fraction of the cyanobiphenyl-containing segment; ^e average number of repeating unit, rounded to 10 units, calculated from M_n for first block in polymerization sequence, calculated from block ratio determined by ¹H-NMR for other block(s).

Table 2. Characteristic data of the block copolymers **4a** and **5a** and their precursors **4** and **5** prepared via route 2.

Precursor	Block copolymer	M_n^a kg mol ⁻¹	M_w^a	PDI ^b	DC ^c %	w_{CB}^d %	ABA ru _A ^e	ru _B ^e	ru _A ^e
4	–	125	128	1.03	–	–	190	680	120
–	4a	601	630	1.05	87	86	190	680	120
5*	–	239	298	1.24	–	–	190	680	120
–	5a	850	1035	1.22	75	85	190	680	120

^a determined by SEC (eluent: THF (**4, 5**)/THF + electrolyte (**4a, 5a**)); molecular weight with respect to polystyrene standards, UV-detection; ^b polydispersity index, M_w/M_n ; ^c degree of conversion of polymer analogous reaction, determined by ¹H-NMR; ^d mass fraction of the cyanobiphenyl-containing segment; ^e average number of repeating unit, rounded to 10 units, calculated from M_n for first block in polymerization sequence, calculated from block ratio determined by ¹H-NMR for other block(s); * coupling of triblock copolymer **4**, 40 % triarm, 35 % dimer, 25 % unimer.

3.2 Liquid crystalline gels

3.2.1 Rheology

We investigated the influence of the gelating network on mechanical properties of the liquid crystalline gels by oscillatory rheology measurements. Two different sets of experiments were performed. In the first part the influence of block copolymer concentration on the rheological behavior is demonstrated using the functionalized block copolymer **3a**. In the second part the influence of the different block copolymers **1a–5a** on the temperature-dependent rheological properties was studied in samples with a fixed block copolymer mass concentration.

Previous electro-optical investigations [22] on the rotational viscosity of dilute solutions of **3a** in 5CB have shown that formation of network clusters occurs above a mass concentration of 1 %. Dynamic measurements of rotational viscosity in these dilute

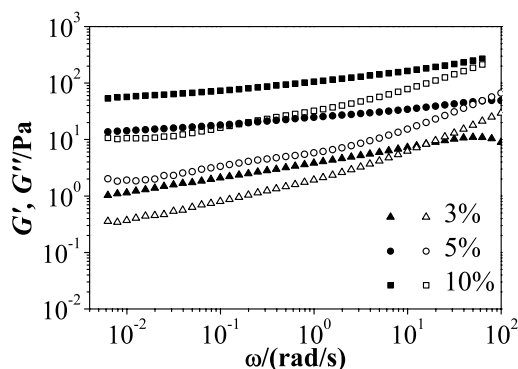


Fig. 4. Frequency sweep of the storage (G' , closed symbols) and loss moduli (G'' , open symbols) for mixtures containing mass concentrations of 3%, 5% and 10% of the functionalized block copolymer **3a** in 5CB at 25 °C.

solutions provided a determination of the critical gelator concentration that was estimated to be around 2.7%.

Representative results of frequency-dependent rheological experiments of **3a** in 5CB at 25 °C in a log-log plot are given in Fig. 4. The storage modulus $G'(\omega)$ and loss modulus $G''(\omega)$ against angular frequency ω are plotted for mass concentrations of 3%, 5%, and 10%. $G'(\omega)$ is higher than $G''(\omega)$ for all concentrations over a wide frequency range indicating a rubbery, *i.e.* gel-like state. All samples show a crossover of $G'(\omega)$ with $G''(\omega)$ at high frequencies. This crossover shifts to higher ω with increasing gelator mass concentration from 20 rad s^{-1} for 3% to around 100 rad s^{-1} for 10%. Above this frequency the mixtures exhibit a viscous liquid-like behavior. $G'(\omega)$ and $G''(\omega)$, as well as their difference, increase with increasing gelator concentration, while for all samples both moduli show a weak dependence on the frequency. For the 3% sample this dependency is slightly more pronounced than for the higher concentrations.

Generally, in isotropic solvents the solubility of many polymers is a function of the temperature; thus, the quality of the solvent changes gradually. In contrast, liquid crystalline solvents exhibit an abrupt change in solvent quality at the temperature of first-order transition from the isotropic into the liquid crystalline phase. Therefore, the association of the A-blocks due to microphase separation and, thus, the formation of the network is expected to occur at T_{ni} [17]. This coupling of gel temperature (T_{gel}) to the isotropic to liquid crystalline transition is a major difference of LC gels formed by polymer gelators compared to physical gels obtained by the self-assembly of fibrous solid networks of low molecular weight gelators. In the latter case commonly the sol-gel transition of the gelator and the isotropic-anisotropic transition of a liquid crystal are observed as two independent transitions [20].

To study the gelation in our system and to investigate the rheological behavior in the proximity of the gel temperature, temperature-dependent measurements were carried out at a heating rate of 1 K min^{-1} and a fixed frequency of 1 Hz (6.28 rad s^{-1}). Temperature regimes with $G' > G''$ are referred to as gel state while the inverse case is denoted as sol state. The temperature of the $G' - G''$ crossover is used as the gel temperature (T_{gel}).

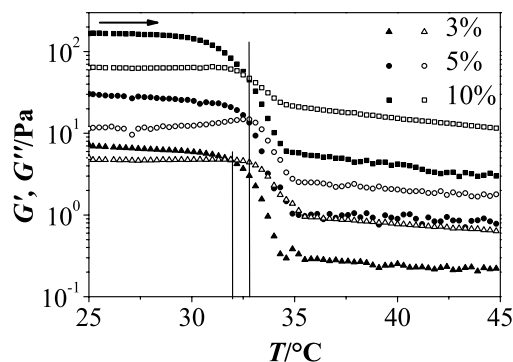


Fig. 5. Temperature dependence of the storage (G' , closed symbols) and loss moduli (G'' , open symbols) ($\omega = 6.28 \text{ rad s}^{-1}$) of 5CB mixtures with concentrations of 3 %, 5 % and 10 % of **3a** on heating with a heating rate of 1 K min^{-1} (arrow indicates direction of sweep).

Firstly, the influence of the gelator concentration is shown by using block copolymer **3a**. The logarithmic plot of the storage modulus (G') and loss modulus (G'') for increasing temperature for 3 %, 5 %, and 10 % mass concentrations of **3a** in 5CB are given in Fig. 5. For all concentrations, at low temperatures G' is nearly constant and higher than G'' indicating a solid-like behavior in the gel state. In the temperature range from $31 \text{ }^\circ\text{C}$ to $34 \text{ }^\circ\text{C}$, G' exhibits a drastic decrease enclosing the crossover with G'' at T_{gel} . Above $35 \text{ }^\circ\text{C}$, in the isotropic sol state, the samples exhibit characteristics of a liquid, $G' < G''$, and both moduli develop nearly parallel. This strong change at T_{gel} is attributed to the segregation of PS-blocks forming network points by association. With increasing block copolymer concentration, both moduli increase over the whole temperature range, as already discussed for the frequency-dependent investigation in Fig. 4. Additionally, T_{gel} changes slightly with decreasing concentration. For 10 % and 5 % concentrations T_{gel} is $32.8 \text{ }^\circ\text{C}$ while for 3 % it is shifted to $31.8 \text{ }^\circ\text{C}$. These determined gel temperatures show a negative deviation from the clearing temperature of neat 5CB that was determined to $35.8 \text{ }^\circ\text{C}$ at a heating rate of 1 K min^{-1} by DSC measurements. A small hysteresis in the gel temperature was observed resulting in $0.1\text{--}0.7 \text{ K}$ higher values on heating than on cooling (not shown). The plateau values of both moduli were virtually identical in the sol and in the gel state.

To study the influence of the gelator backbone on the gelation temperature, in Fig. 6, the temperature dependence of G' and G'' of samples containing a mass concentration of 5 % of the functionalized block copolymers **1a–5a** is shown in the temperature range of $25 \text{ }^\circ\text{C}$ to $45 \text{ }^\circ\text{C}$. The sample containing **1a**, featuring the longest PS A-blocks ($r_{\text{uA}} = 490$), exhibits the sharpest transition from the gel to the sol state. Between $25 \text{ }^\circ\text{C}$ and $34 \text{ }^\circ\text{C}$, G' is higher than G'' and both are nearly constant. In an interval of 2 K around T_{ni} of 5CB, G' decreases abruptly, showing a crossover with G'' at $35.4 \text{ }^\circ\text{C}$. At temperatures outside this interval G' and G'' again run parallel with a minimal slope. Only in this sample T_{gel} coincides with the nematic to isotropic transition temperature of the solvent. For the samples containing **2a** and **3a** the temperature range of the gel–sol transition broadens slightly and T_{gel} shifts to lower temperatures. Both samples exhibit similar storage moduli in the gel state that are about one third the value of G' for the

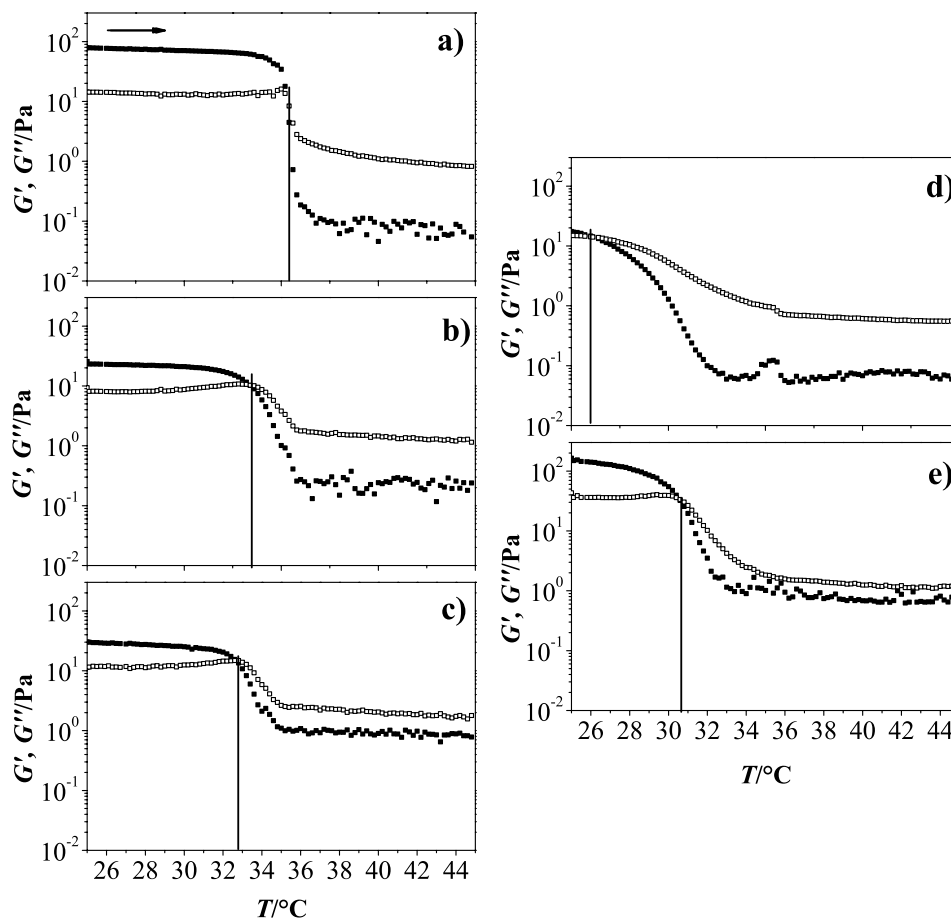


Fig. 6. Temperature dependence of the storage (G' , closed symbols) and loss moduli (G'' , open symbols) of 5CB samples containing a mass concentration of 5% of CB functionalized linear triblock copolymer **1a** (a), **2a** (b), **3a** (c), **4a** (d), and the star block copolymer **5a** (e) on heating with a heating rate of 1 K min^{-1} at $\omega = 6.28 \text{ rad s}^{-1}$ (arrow indicates direction of sweep).

sample containing **1a**. The sample **4a** with the lowest molecular weight as well as the shortest A- and B-blocks in this series behaves like a liquid over the observed temperature range at the given block copolymer mass concentration. Even at $25 \text{ }^{\circ}\text{C}$, G' is only 2 Pa higher than G'' and their crossover occurs at $26.2 \text{ }^{\circ}\text{C}$.

The decrease of the gel temperature and the increasing deviation from the T_{ni} in the series of linear gelators corresponds to the decreasing lengths of the polystyrene A-blocks. The formation of the physical gel network is based on the association of the PS-segments. The phase separation between the nematic solvent and the isotropic PS-segments is dependent on the molecular weight of the PS [1]. Thus, it is reasonable to assume that the shift of the gel temperature to lower values is caused by the decreasing lengths of the PS-segments, although it has to be noted that the absolute differences in the repeating units of the block copolymer segments are rather small ($ru_{\text{A}} = 490$ (**1a**),

430 (**2a**), 360 (**3a**), 190/120 (**4a**)). A similar trend has been observed for AB-diblock copolymers comprising a PS-block and a functionalized side group liquid crystalline segment. In mixtures with 5CB the microphase separation temperature was influenced by the length of the PS-segments and could be adjusted above or below the T_{ni} [16].

These results show that variations in length of the B-block have only a weak influence on the rheological behavior of the mixtures. In contrast, small variations in length of the A-block feature a substantially larger influence. The sample containing **1a** exhibits the highest G' in the gel state in this series which might be attributed to the short middle block that determines the network span. Nevertheless, samples with **2a** ($r_{uB} = 1860$) and **3a** ($r_{uB} = 2670$) exhibit similar storage moduli under the given experimental conditions.

The sample containing the star block copolymer **5a** shows a significantly different behavior than the respective linear block copolymer **4a**. Here, the gel temperature is determined at 30.7 °C. This is still below the values found for the block copolymers **1a–3a** with longer A-segments but an increase of 4.5 °C compared to **4a**. Additionally, G' in the gel state is considerably higher than for the samples containing linear gelators. In a gel containing a linear ABA-triblock copolymer gelator each polymer chain in a bridge conformation can be connected to two different physical nodes [17]. In the case of a three arm star block copolymer with each arm consisting of a linear triblock copolymer the number of physical crosslinking points is increased to three and a new chemical link is introduced connecting the three arms. The inner core of the star-shaped block copolymer where polystyrene A-blocks are covalently connected can also serve as a physical crosslinking point in the network created by the gelator in the low molecular weight liquid crystal 5CB.

In isotropic solvents for $(AB)_x$ star block copolymers with an increasing arm number up to a maximum of four arms an increase in G' and G'' has also been observed [29]. Thus, in our case the increase of the gel temperature and the higher storage modulus might be attributed to the introduction of a chemical link.

3.2.2 Electro-optical measurements

We characterize the influence of the polymer network structure on the electro-optical properties of the liquid crystalline gels by examining their light scattering behavior in thin films. The test cells, filled with the liquid crystalline mixtures, are optically transparent in the isotropic state. When the cells are cooled below T_{ni} , all samples are opaque in the nematic state. The application of an electric field leads to a decrease of the scattering in this anisotropic state. At sufficiently high voltages, the transmittance of light approaches the isotropic one. Thus, to study the transition from opaque to transparent states under electric fields, the temporal evolution of transmitted light intensity I at different driving voltages was recorded at $T_{meas} = 25$ °C. Before each measurement, the samples were heated up into the isotropic state and subsequently cooled down to T_{meas} . This procedure provides identical initial conditions for all measurements of each sample.

All electro-optical measurements were done at a fixed mass concentration of block copolymer in 5CB to compare the influence of the different chemical structures. The scattering efficiency of the nematic gel increases with increasing polymer content.

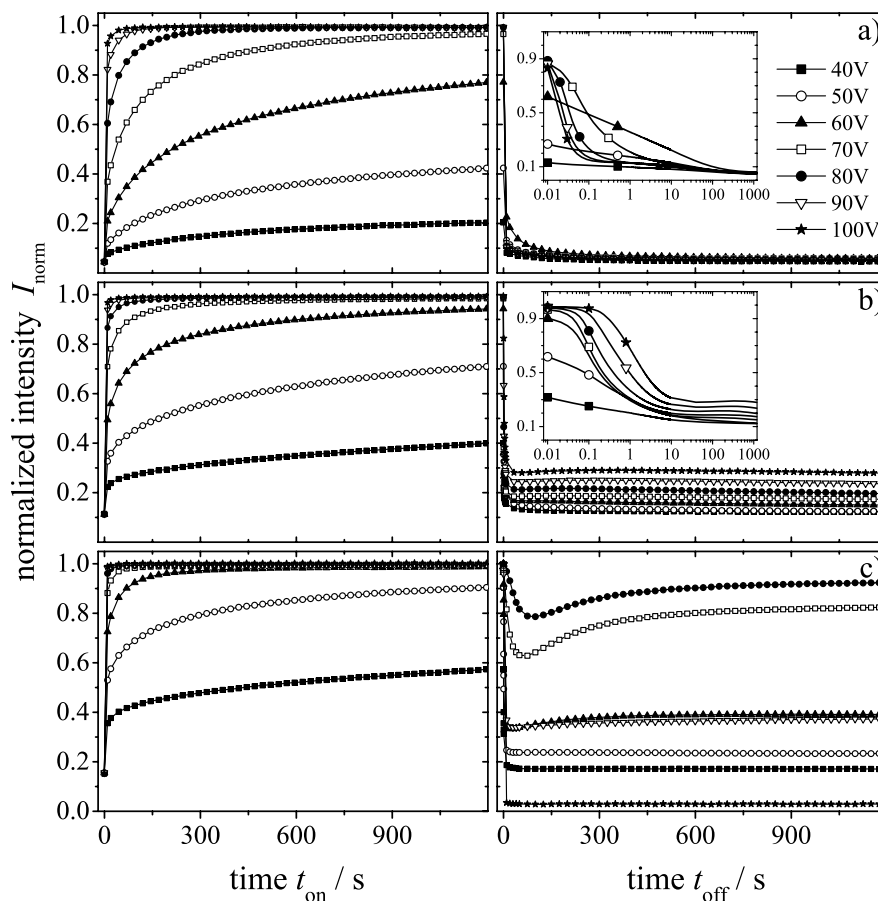


Fig. 7. Temporal evolution of the normalized transmitted light intensity after applying an overcritical electric voltage U_{on} at $t_{\text{on}} = 0$ and switching back to $U_{\text{off}} = 1 \text{ V}$ at $t_{\text{off}} = 0$. The data represent 5CB samples containing a) 10% of **1a**, b) 10% of **2a** or c) 10% of **3a**, after a moderate cooling rate of around 0.01 K s^{-1} within the anisotropic regime. The semi logarithmic insets give a better resolution of the fast switching behavior.

Hence, to achieve sufficiently high scattering, we selected a mass concentration of 10% for all samples.

Figure 7 shows the electro-optical response of 5CB mixtures containing functionalized block copolymers **1a–3a** after switching to different voltages U_{on} at $t_{\text{on}} = 0$ and back to $U_{\text{off}} = 1 \text{ V}$ at $t_{\text{off}} = 0$. In the initial state ($t_{\text{on}} = 0$), these mixtures exhibit a strongly scattering macroscopically opaque state, yielding different values of the initial normalized transmittance $I_{\text{norm}} = I/I_{\text{iso}} = 0.05 - 0.15$.

When an electric voltage U_{on} is suddenly applied, the transmittance of all samples increases with time (left part of Fig. 7) due to the reorientation of the mesogenes – 5CB has a positive dielectric anisotropy and tends to align parallel to an electric field. For all of our investigated mixtures this reorientation is slower than for pure 5CB, because of the elastic coupling between the liquid crystal molecules and the network. The intensity

saturates to a certain value, which depends on the magnitude of U_{on} and on the network properties defined by the block copolymer structure.

After switching the voltage back to U_{off} , the samples relax to a stronger scattering state, but in many cases they do not reach the initial value of $I_{\text{norm}}(t_{\text{on}} = 0)$. The semi-logarithmic insets of Fig. 7a and 7b indicate a faster relaxation for the sample with **1a** compared to the mixture with **2a** upon switching from high transmitting states, $I_{\text{norm}}(t_{\text{off}} = 0) \approx 1$. Generally, with increasing U_{on} an increase in the off-level $I_{\text{norm}}(t_{\text{off}} = 1200 \text{ s})$ can be observed. In contrast, on the right hand-side of Fig. 7c, the lines for $U_{\text{on}} = 90 \text{ V}$ and 100 V do not fit this trend. At these voltages, a macroscopic change of the scattering state occurs in the cell. It can be observed by naked eye and results in an inhomogeneity of the opaque scattering structure. This effect is not yet understood and will be investigated in further experiments. It is also remarkable that some of the curves show a non-monotonic decay.

Figure 8 is the analogue of Fig. 7, but for mixtures with the block copolymer **4a** and **5a**. For these samples also a higher cooling rate (0.05 K s^{-1}) was studied, as the initial scattering was low for the usual moderate cooling rate (0.01 K s^{-1}). The overall switching behavior of the on-process, shown at the left-hand side of Fig. 8, demonstrates the same trend as described for samples with **1a–3a**. Notably, in some cases the transmittance shows a non-monotonic behavior at the on-process which seems to be reduced by a faster cooling rate. The off-process is monotonic, but does not reach the initial value of $I_{\text{norm}}(t_{\text{on}} = 0)$ in all cases.

To study the influence of the cooling rate on the initial scattering states, the initial intensity obtained from Figs. 7 and 8 against the temperature span between T_{ni} and T_{gel} (obtained from the temperature-dependent rheology measurements in Fig. 6) is shown in Fig. 9. With increasing $T_{\text{ni}} - T_{\text{gel}}$ the initial intensity of the samples increases.

The differences of initial scattering states at identical cooling rates might be due to the aligning process of the liquid crystal which occurs below T_{ni} and above T_{gel} . Upon cooling the sample slowly from T_{ni} to room temperature, the liquid crystal molecules are arranged in well aligned macroscopic domains with a similar orientation. Due to the elastic coupling of the 5CB molecules to the side-group mesogenes, the polymer backbone is adjusted to reduce the elastic distortion of the liquid crystal matrix. When the nodes of the network are formed no reorientation of the polymer molecules is possible and the scattering intensity is determined by the size of the domains of similar orientation. As the order parameter of the LC solvent increases with decreasing temperature, a larger difference $T_{\text{ni}} - T_{\text{gel}}$ leads to lower scattering.

The difference between the initial intensities, obtained after different cooling rates (investigated for samples containing **4a** and **5a**) might be explained by the low mobility of the block copolymers. Hence, the final degree of alignment of the network in the LC molecules depends on the time interval between crossing T_{ni} and T_{gel} . A higher cooling rate decreases this time interval and reduces the possibility of the polymer to adopt the aligning of 5CB molecules. Hence, the size of well aligned 5CB domains is decreased resulting in a higher scattering.

Figure 10 summarizes the switching behavior of all investigated samples. Figure 10a shows the maximal transmitted intensity I_{max} at the on-state. For the non-monotonic curves, this is the maximum. For the monotonic curves, this maximum is extrapolated by an exponential fit on the tail of the transmission curve, because the

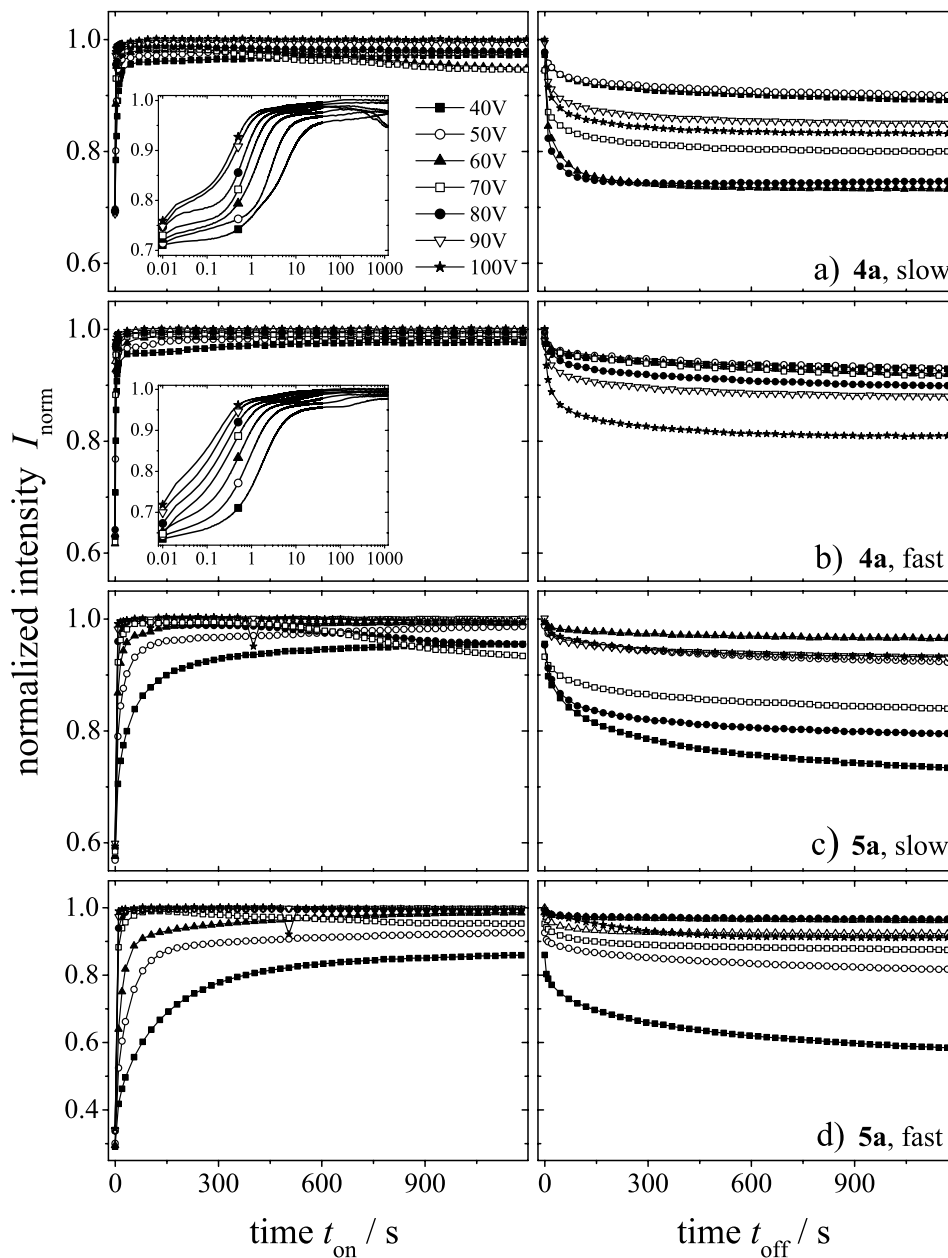


Fig. 8. Temporal evolution of the normalized transmitted light intensity after applying an overcritical electric voltage U_{on} at $t_{\text{on}} = 0$ and switching back to $U_{\text{off}} = 1$ V at $t_{\text{off}} = 0$. a) and c) correspond to measurements after a moderate cooling rate of around 0.01 K s^{-1} , b) and d) to a fast cooling rate of about 0.05 K s^{-1} within the anisotropic regime. The data represent 5CB samples containing 10% of **4a** (a, b) or **5a** (c, d). The semi logarithmic insets give a better resolution of the fast switching behavior.

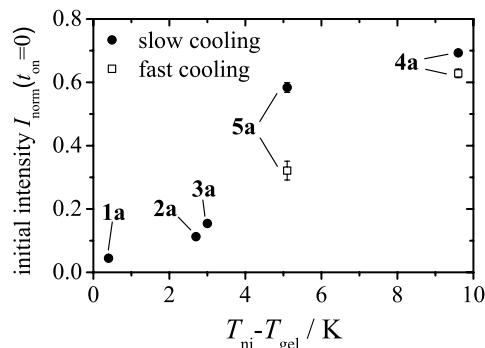


Fig. 9. Initial transmission of light at room temperature vs. deviation of the gelation temperature T_{gel} of the block copolymer mixture from the clearing temperature T_{ni} of pure 5CB. A slow cooling indicates a cooling rate of $\approx 0.01 \text{ K s}^{-1}$ in the anisotropic regime $T < 35 \text{ }^\circ\text{C}$, fast cooling represents $\approx 0.05 \text{ K s}^{-1}$.

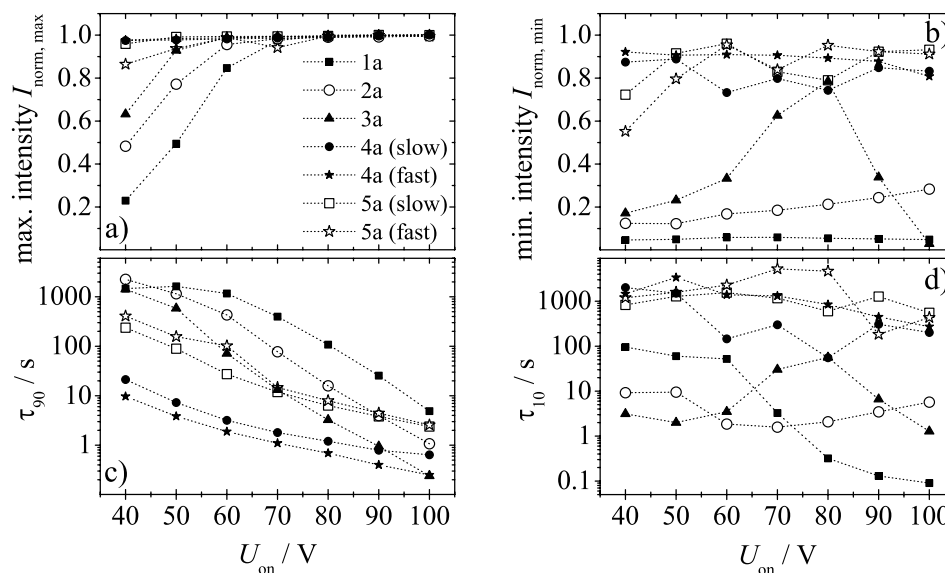


Fig. 10. a) Maximal transmitted intensity while applying an overcritical voltage U_{on} . b) Minimal intensity after switching off the voltage. For unsaturated states, a single exponential increase/decay was fitted on the second part of the transmission curves to estimate the saturation value. For non-monotonic curves, the local extremum was used for maximal/minimal intensity. c) Time required to reach 90% of the maximal intensity. d) Time required for returning back to 10% of the difference between maximal and minimal intensity.

saturation value was not reached within the measurement time. The minimum intensity, displayed in Fig. 10b, is obtained by the corresponding logic. The maximal transmitted intensity increases for all of our samples with the increase of U_{on} . The non-monotonic behavior of the minimal intensity for the mixture with **3a** corresponds to the macroscopic change of the scattering state mentioned in connection with Fig. 7c.

At low voltages U_{on} , the electric torque appears to be too small to induce a homeotropic orientation of the liquid crystal molecules in all domains. Hence, the transmitted intensity is low. Increasing the strength of the electric field, one reaches a critical value where the transmission approaches a maximum value of $I_{\text{norm}} \approx 1$. The magnitude of that critical voltage varies with the lengths of the copolymer blocks. For **1a** at a voltage of $U_{\text{on}} = 70$ V, the intensity seems to saturate to the maximal possible intensity but not within the measurement time of 20 min, whereas this is already the case for **2a**. For **3a**, a voltage of $U_{\text{on}} = 60$ V is already enough to switch to the highest transmittance. Except for the initial scattering states, the difference in cooling rate does not influence the electro-optical behavior of **4a** and **5a** significantly (compare Fig. 8). Figure 10a shows that for both samples the critical voltage is very low compared to **1a–3a**.

Within the off-state, characterized in Fig. 10b, only for the sample containing the block copolymer **1a** the intensity decays to the initial value – *i.e.* the strongest scattering state – independent on U_{on} . For the mixtures with **2a** and **3a**, this can only be achieved for low voltages. After higher voltages, the minimal intensity increases indicating a less scattering structure. The off-states of samples with **4a** and **5a** show continuously high intensities. Even for the lowest U_{on} , these mixtures do not relax back to the initial scattering state.

Figure 10c characterizes the temporal response to the electric field by τ_{90} , the time which is required to reach 90 % of the difference between initial and maximum transmittance. These rise times decrease with increasing U_{on} by one to three orders of magnitude in all measurements. The mixture with **1a** presents the slowest response while an increase of the middle block length – as in samples **2a** and **3a** – leads to faster reactions for all U_{on} . The response of sample **4a** is very fast, independent of the cooling rate. Using the star block copolymer **5a** yields an increase of τ_{90} compared to the corresponding linear block copolymer **4a**.

Figure 10d displays the decay times τ_{10} , where 10 % of the difference between $I_{\text{norm}}(t_{\text{off}} = 0)$ at U_{on} and the minimal intensity at U_{off} is reached. Samples with **1a**, **2a** and **3a** exhibit the trend of a faster relaxation than **4a** and **5a** mixtures when the voltage is switched off. With increasing U_{on} the sample with **1a** shows a decrease of τ_{10} , resulting in the fastest relaxation after high voltages. The relaxation time of **2a** is almost constant while **3a** shows an increase of τ_{10} for $U_{\text{on}} < 90$ V. In general, for low voltages $U_{\text{on}} < 60$ V, there is a tendency of an increase of τ_{10} with decreasing B-block length. But particularly for higher voltages, there is a high discontinuity, which could be also an effect of the limited accuracy on the estimation of the saturation values. It also has to be noted, that in the case of non-monotonic off-curves, the local minimum defines the lower limit of the intensity range. Hence, the corresponding τ_{10} values might be limited in comparability.

The results of the electro-optical measurements allow us to draw some conclusions regarding the network structure of the polymer gelator. In the gel state, the network can be regarded as a system of A-block nodes connected by B-block bridges (see Fig. 1). The liquid crystal solvent occupies the space between the network filaments, interacting with the side-group mesogens of the polymer. Hence, by applying an electric field, the rotation of the 5CB molecules is coupled to the elastic distortion of the polymer network [19]. This network elasticity is influenced by B-block lengths and, thus, variation

of these lengths leads to differences in the response to an electric field resulting in different critical voltages. The block copolymer **1a** has the shortest B-block ($ru_B = 930$) compared to **2a** ($ru_B = 1860$) and **3a** ($ru_B = 2670$), resulting in shorter and less flexible network bridges and a strong restoring torque on the 5CB molecules. Hence, the mixture with **1a** shows the highest critical voltage and the slowest response at the on-state. With increasing length of the B-block (**2a** and **3a**), the network density decreases and the effective volume of the liquid crystal filled domains increases. Thus, the restoring torque on the liquid crystal molecules decreases and a higher orientation towards a homeotropic state can be reached with the same electric field.

Additionally, the disassembly and reformation of the physical crosslinks, formed by the A-blocks, has to be taken into account. Under a strong electric field an irreversible restructuring of the network might occur if the A-blocks are short. Consequently, in the samples with block copolymer **1a–3a**, the decreasing A-block lengths ($ru_A = 490 - 360$) results in an increasing off-level of the transmittance after application of the same electric fields. Only the sample containing **1a** with the longest A-blocks shows a relaxation to the initial scattering state, independent on the previously applied voltage.

The correlation between the B-block length and the elasticity of the network does not hold for the electro-optical response of samples with **4a** and **5a**. Regarding **4a**, it has to be noted, that the electro-optical measurements were performed at 25 °C at which temperature the rheological indication of a gel state is weak. Although **4a** and **5a** are the block copolymers with the shortest B-block ($ru_B = 680$), which are expected to result in a dense network with a high restoring torque, their critical voltages (see Fig. 10a) are even lower than for **3a**. The fast response to U_{on} shown for **4a** is also remarkable when compared to the trend provided by **1a**, **2a** and **3a**. For those samples it is obvious, that a short B-block favors a slower response to the electric field. Furthermore, the samples with **4a** and **5a** show high transmission in the off states and no complete relaxation to the initial state even after small U_{on} .

This observations might be explained by the A-block lengths ($ru_A = 120, 190$) that are the shortest in this series **1a–5a**. Thus, the physical crosslinks might be less strong resulting in a disassembly of the nodes even under weak electric fields.

4. Conclusion

A series of new cyanobiphenyl-functionalized ABA-triblock copolymers has been presented capable of gelating the liquid crystal 5CB at low polymer concentrations. Variations regarding the block lengths as well as the backbone architecture allowed us to study the impact of the polymer backbone on the properties of the liquid crystalline gels. Oscillatory rheological measurements revealed that the gel temperature equals the nematic to isotropic temperature only for longer A-blocks and is shifted below the phase transition temperature with decreasing block length. While in this case rather small variations in block length ($120 \leq ru_A \leq 490$) seem to have a significant impact, the length of the functionalized B-block does not show such a strong influence. Nonetheless, gels with gelator **1a**, containing a short B-block ($ru_B = 930$), showed a higher storage modulus than gels prepared with linear gelators with longer B-blocks ($ru_B = 1860, 2670$). The change from linear to star block copolymer architecture by

introducing chemical linkages increased the gel temperature as well as the storage modulus in the gel state compared to the respective linear gelator.

The electro-optical response in light scattering experiments showed with increasing B-block length a decrease of critical voltages for switching to the highest transmission due to a higher elasticity of the network. Additionally, longer B-blocks also result in a faster response at the same driving voltage. Only the gel containing gelator **1a**, with the longest A-segments, exhibited a fully reversible switching behavior for all driving voltages, *i.e.*, after switch off, the system relaxed back to the initial transmission intensity. For shorter lengths of the PS-block the initial values were not fully restored while the difference between initial and final intensity increased with decreasing A-block length of the gelators. This is attributed to an irreversible deformation of the network due to the weakness of the physical crosslinks, another effect expanding the tuneability of the properties of liquid crystalline gels.

Acknowledgement

We gratefully acknowledge financial support of the Deutsche Forschungsgemeinschaft (DFG), FOR608, project “Thermoreversible liquid crystalline gels under the influence of electric fields”. R.P. would also like to thank the Elite Study Program – Macromolecular Science for support.

References

1. M. Ballauff, *Mol. Cryst. Liquid Cryst.* **136** (1986) 175.
2. M. Ballauff, *Ber. Bunsen Ges. Phys. Chem.* **90** (1986) 1053.
3. H. Orendi and M. Ballauff, *Macromolecules* **24** (1991) 5874.
4. M. Ballauff, *Mol. Cryst. Liquid Cryst.* **196** (1991) 47.
5. P. J. Flory and A. Abe, *Macromolecules* **11** (1978) 1119.
6. A. Abe and P. J. Flory, *Macromolecules* **11** (1978) 1122.
7. P. J. Flory and R. S. Frost, *Macromolecules* **11** (1978) 1126.
8. R. S. Frost and P. J. Flory, *Macromolecules* **11** (1978) 1134.
9. P. J. Flory, *Macromolecules* **11** (1978) 1138.
10. P. J. Flory, *Macromolecules* **11** (1978) 1141.
11. H. Ringsdorf, H. W. Schmidt, and A. Schneller, *Makromol. Chem. Rapid Commun.* **3** (1982) 745.
12. J. Adams and W. Gronski, *Makromol. Chem. Rapid Commun.* **10** (1989) 553.
13. M. Walther, H. Faulhammer, and H. Finkelmann, *Macromol. Chem. Phys.* **199** (1998) 223.
14. N. R. Scruggs, J. A. Kornfield, and J. Lal, *Macromolecules* **39** (2006) 3921.
15. N. R. Scruggs and J. A. Kornfield, *Macromol. Chem. Phys.* **208** (2007) 2242.
16. N. R. Scruggs, R. Verduzco, D. Uhrig, W. Khan, S.-Y. Park, J. Lal, and J. A. Kornfield, *Macromolecules* **42** (2009) 299.
17. M. D. Kempe, N. R. Scruggs, R. Verduzco, J. Lal, and J. A. Kornfield, *Nat. Mater.* **3** (2004) 177.
18. M. D. Kempe, R. Verduzco, N. R. Scruggs, and J. A. Kornfield, *Soft Matt.* **2** (2006) 422.
19. R. Verduzco, N. R. Scruggs, S. Sprunt, P. Palffy-Muhoray, and J. A. Kornfield, *Soft Matt.* **3** (2007) 993.
20. T. Kato, Y. Hirai, S. Nakaso, and M. Moriyama, *Chem. Soc. Rev.* **36** (2007) 1857.
21. N. Mizoshita, Y. Suzuki, K. Kishimoto, K. Hanabusa, and T. Kato, *J. Mater. Chem.* **12** (2002) 2197.
22. M. Khazimullin, T. Müller, S. Messlinger, I. Rehberg, W. Schöpf, A. Krekhov, R. Pettau, K. Kreger, and H.-W. Schmidt, *Phys. Rev. E* **84** (2011) 2171.

23. G. Mao, J. Wang, S. R. Clingman, C. K. Ober, J. T. Chen, and E. L. Thomas, *Macromolecules* **30** (1997) 2556.
24. C. T. Imrie, F. E. Karasz, and G. S. Attard, *Macromolecules* **26** (1993) 3803.
25. M. Häckel, L. Kador, D. Kropp, C. Frenz, and H.-W. Schmidt, *Adv. Funct. Mater.* **15** (2005) 1722.
26. T. Breiner, K. Kreger, R. Hagen, M. Haeckel, L. Kador, A. H. E. Mueller, E. J. Kramer, and H.-W. Schmidt, *Macromolecules* **40** (2007) 2100.
27. H. Audorff, K. Kreger, R. Walker, D. Haarer, L. Kador, and H.-W. Schmidt, *Adv. Polym. Sci.* **228** (2010) 59.
28. R. Pettau, C. Erdelen, and H.-W. Schmidt, *Macromol. React. Eng.* **4** (2010) 65.
29. H.-H. Lin and Y.-L. Cheng, *Macromolecules* **34** (2001) 3710.

2.3 Ordering of Granular Rod Monolayers Driven Far from Thermodynamic Equilibrium

Authors: Thomas Müller, Daniel de las Heras, Ingo Rehberg,
and Kai Huang

Journal: Physical Review E

Date of submission: March 12, 2015

Preprint: <http://arxiv.org/abs/1503.03737>

Status: under review

Ordering of Granular Rod Monolayers Driven Far from Thermodynamic Equilibrium

Thomas Müller,¹ Daniel de las Heras,² Ingo Rehberg,¹ and Kai Huang^{1,*}

¹*Experimentalphysik V, Universität Bayreuth, D-95440 Bayreuth, Germany*

²*Theoretische Physik II, Universität Bayreuth, D-95440 Bayreuth, Germany*

(Dated: April 22, 2015)

The orientational order of vertically agitated granular rod monolayers is investigated experimentally and compared quantitatively with equilibrium Monte Carlo simulations and density functional theory. At sufficiently high number density, short rods form a tetratic state and long rods form a uniaxial nematic state. The length-to-width ratio at which the order changes from tetratic to uniaxial is around 7.3 in both experiments and simulations. This fact illustrates the universal aspects of the ordering of rod-shaped particles across thermal and athermal systems. Moreover, the assembly of granular rods into ordered states is found to be independent on the frequency and strength of the agitations, suggesting that the detailed nature of energy injection into such a nonequilibrium system does not play a crucial role.

PACS numbers: 45.70.-n, 05.70.Ln, 64.70.M-

I. INTRODUCTION

The ordering of anisotropic particles is a universal phenomenon appearing widely in nature, ranging from thermally driven molecules or colloids [1–4] to active particles such as bacteria colonies [5], actin filaments [6, 7], animal groups [8–10], and living liquid crystals [11]. In equilibrium lyotropic systems, such as hard rods interacting only through excluded volume interactions, the transition of sufficiently anisotropic particles into various ordered states is entropy driven. The loss in rotational degrees of freedom in the ordered state is compensated by the gain in the translational ones [3, 4, 12]. Taking a two-dimensional system of hard rectangles as an example, a tetratic state with four-fold rotational symmetry has recently been discovered in Monte Carlo (MC) simulations [13, 14], and studied theoretically with density functional theory (DFT) [15–17]. The number density and the length-to-width ratio (aspect ratio) of the particles are found to be the key parameters determining the ordered states of hard rectangles with only excluded volume interactions [15]. Given the ubiquity of ordering transitions in nature, it is important to ask how well the existing knowledge on such transitions in equilibrium (thermal) systems can be extended to nonequilibrium (athermal) systems.

Due to the dissipative interactions between particles, agitated granular matter has been frequently used as a nonequilibrium model system for phase transitions [18–24]. Rich and often counterintuitive dynamical behaviors [25] have been discovered for granular rods, including vortex patterns [26], collective swirling motions [27], giant number fluctuations [28, 29], violation of the equipartition theorem [30], and an enhanced ordering transition in an effective ‘thermal’ bath of spherical particles [31]. Reminiscent to equilibrium systems, ordering transitions of vertically agitated granular rods have

been investigated in three-dimensional (3D) and quasi-two-dimensional systems. In 3D, the aspect ratio of the rods was found to influence the ordered state of cylindrically shaped rods [36]. In quasi-two-dimensional systems, a bulk isotropic-uniaxial nematic (I-U) transition was observed for cylindrical rods with large aspect ratio [32] and an effective elastic constant was characterized quantitatively [33]. Particularly in strict monolayer systems, the shape of the rods was found to play an important role in determining the ordered states: Tetratic, nematic or smectic ordering was found for cylindrical rods, tapered rods or rice particles correspondingly [34]. Moreover, tetratic ordering was also found for tubular shaped particles and the influence of the container shape was discussed in [35].

Despite of these progresses, it is still unclear to which extent one can draw quantitative connections between systems in and out of thermodynamic equilibrium. More specifically, a quantitative comparison between the state diagram of dissipative granular rods and that of the corresponding equilibrium model system is still lacking. This quantitative comparison is the purpose of the present work. Here, we investigate experimentally the orientational ordering of cylindrically shaped granular rod monolayers driven far from thermodynamic equilibrium, and compare the results to MC simulations as well as DFT of the analogous equilibrium system. Focusing on the bulk region of the system, we detect both tetratic and uniaxial nematic states by varying the aspect ratio of the rods. We demonstrate that the aspect ratio and the number density of rods are the key parameters determining the state diagram in both systems. In the state diagram, we find a common aspect ratio that separates tetratic and uniaxial nematic states in both experiments and MC simulations. Such an agreement illustrates the universal aspects of the ordering of rod-shaped particles.

* kai.huang@uni-bayreuth.de

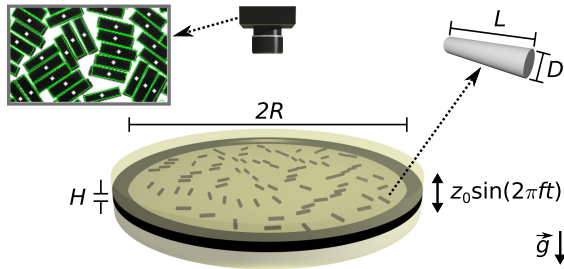


FIG. 1. (Color online) Sketch of the experimental set-up. The closed cylindrical container of height H and radius R is driven sinusoidally against gravity with an electromagnetic shaker. The rods have a length L and a diameter D . The embedded image shows a close view of the detected particles.

II. METHODS

A. Experiments

A sketch of the experimental set-up is shown in Fig. 1. Monodisperse polyvinyl chloride (PVC) rods of diameter D and length L , cut from welding wires of $D = 3$ mm (aspect ratio $L/D \leq 5$) or 1.5 mm ($L/D \geq 5$), are confined in a cylindrical container of height H and radius $R = 10$ cm. The ratio $H/D = 4/3$ is chosen for both diameters to ensure a monolayer of particles; that is, no rods can cross or jump over each other. The inner surface of the container is covered with antistatic spray (Kontakt Chemie, Antistatik 100) to minimize electrostatic forces. An electromagnetic shaker (Tira TV50350) is employed to drive the sample sinusoidally against gravity with frequency $f = 50$ Hz and peak acceleration $\Gamma = 4\pi^2 f^2 z_0/g$, where z_0 is the peak vibrational amplitude and g is the gravitational acceleration. The acceleration is monitored with an accelerometer (Dytran 3035B2). We capture high contrast images of the rods using backlight LED illumination and a camera (IDT MotionScope M3) mounted above the container. The camera is synchronized with the shaker so as to capture images at a fixed phase of each vibration cycle. The images are subjected to an analysis algorithm that determines the center of mass $P_i = (x_i, y_i)$ and the orientation $\theta_i \in [0, \pi[$ of the i -rod with $i \in [1, N]$. θ_i is the angle of the main rod axis with respect to a fixed laboratory axis, and N is the total number of rods in the container. The detection rate is 100 % for $D = 3$ mm and 95 % for $D = 1.5$ mm.

To systematically study the collective behavior of the rods, we vary the global area fraction $\Phi_g = \frac{NLD}{\pi R^2}$ between ~ 0.3 and ~ 0.9 , and the aspect ratio L/D between 2.0 and 13.3. For each Φ_g and L/D , we vary the peak acceleration Γ with a step of 1 from 2 to 20 and back. The waiting time between each step is fixed at ~ 1.5 minutes. We repeat the whole cycle at least 3 times.

B. Simulations and theory

Correspondingly, we model the particles as two-dimensional hard rectangles of length L and width D that interact through excluded volume interactions. N of such particles are placed in a box with dimensions L_x and L_y along the x - and y -axes, respectively. We use periodic boundary conditions in both axes and study the equilibrium bulk configurations by means of standard MC simulations [37] in the canonical ensemble. That is, we fix the number of particles N and the system area $A = L_x L_y$ (the temperature is irrelevant in hard models). The number of particles is similar to that in the experiments, $N \sim 10^3$. We use simulation boxes with rectangular and square shapes. No difference has been found between both geometries.

The simulation method is as follows. In order to equilibrate the system we start at very high area fractions, $\phi \approx 0.95$, placing the particles, with their main axes pointing in the same direction, in a rectangular lattice. Next we run 10^7 Monte Carlo steps (MCSs). Each MCS is an attempt to move and rotate all the particles in the system. The maximum displacement Δr_{\max} and maximum rotation $\Delta \theta_{\max}$ that each particle is allowed to perform in a MCS is determined such that the acceptance probability is 0.2. Then we remove a few particles randomly chosen, recalculate Δr_{\max} and $\Delta \theta_{\max}$, and start a new simulation. The number of removed particles is such that the change in area fraction is $\Delta \phi \lesssim 0.01$. In order to rule out metastable configurations related to the preparation of the initial state, we discard simulations with $\phi \gtrsim 0.8$. When the area fraction is below that limit we start the proper simulation. For each simulation we first run 10^6 MCSs to equilibrate the system and then accumulate data over 10^7 MCSs. For selected L/D we have also simulated the system by increasing the number of particles, i.e. by adding particles instead of removing them. We have found no differences between both methods.

In addition, an Onsager-like DFT is employed to study the equilibrium bulk phase behavior. Details on the implementation of the DFT are provided in appendix A.

III. RESULTS AND DISCUSSION

This section is organized as follows: We first introduce the ordered states observed in experiments and MC simulations in section III A. In section III B, we characterize experimentally the influence of the container walls and the driving conditions. Finally in section III C, we quantify the ordering transition threshold for various aspect ratios and compare the state diagrams obtained experimentally, in simulations and with DFT.

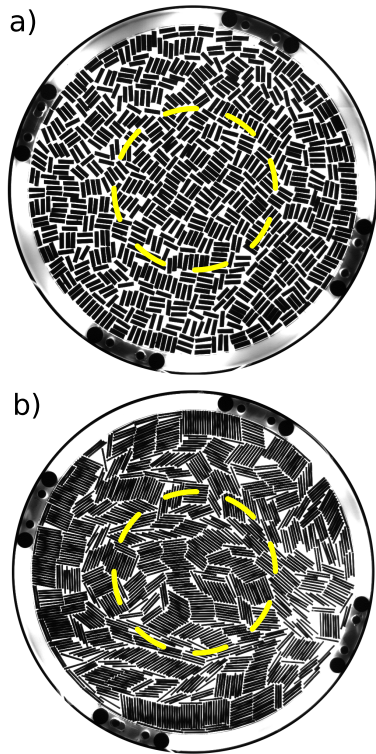


FIG. 2. (Color online) Raw experimental images (topview) showing typical configurations of rods with aspect ratio $L/D = 3.3$ (a) and $L/D = 10.0$ (b) at high global area fractions. The yellow dashed circle indicates the region of interest.

A. Ordered states

Figure 2 shows typical snapshots of the ordered states obtained experimentally. Short rods (a) tend to develop tetratic ordering with two alignment directions perpendicular to each other. Long rods (b) form uniaxial nematic ordering with only one preferred alignment direction. In both cases, the container promotes either homeotropic (perpendicular) or planar (parallel) anchoring of the rods close to the boundaries. To minimize the influence of boundary effects, we consider only those particles located in the central region of the container, as marked in Fig. 2. A quantitative justification of this region of interest (ROI) will be given in section III B. Sometimes during the experiments, especially at low global area fractions, we observe regions with very low number density of rods (almost empty regions). As we are interested in the bulk behavior, we discard those configurations in which the “empty regions” and the ROI overlap.

Figure 3 shows a direct comparison of the ordered states obtained in both experiments and MC simulations. The color coded rod configurations are reconstructed from agitated granular rods in the ROI of the container (upper panels) and from MC simulations (middle panels)

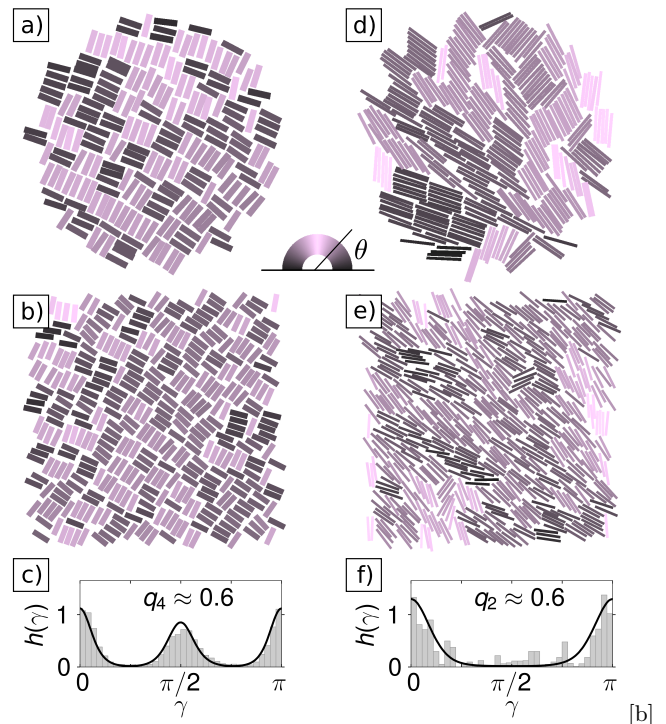


FIG. 3. (Color online) Typical snapshots of tetratic (left column, $L/D = 3.3$) and uniaxial nematic (right column, $L/D = 10.0$) states. a) and d) are reconstructed from the positions and orientations of the particles detected in the center region of the container. b) and e) are from MC simulations with periodic boundary conditions. The rods are color coded according to their orientations. The lower panels show the orientational distribution functions $h(\gamma)$ of the rods in experiments (gray bars) and simulations (solid line). γ is the angle with respect to the director. [b]

with periodic boundary conditions. In the tetratic state with fourfold rotational symmetry (left column), the orientational distribution function $h(\gamma)$, where γ is the angle with respect to the director \hat{n} , has two peaks at $\gamma = 0$ and $\gamma = \pi/2$ (c). In contrast, in the uniaxial nematic state (right column), the elongated particles are oriented on average along the director, yielding only one peak at $\gamma = 0$ (f). The director \hat{n} is calculated as the eigenvector of the largest eigenvalue of the tensorial order parameter $Q_{\alpha\beta} = \langle 2w_{\alpha,i}w_{\beta,i} - \delta_{\alpha\beta} \rangle$. Here $w_{\alpha,i}$ is the α th Cartesian coordinate of the unit vector $\hat{w}_i = (\cos \theta_i, \sin \theta_i)$, $\delta_{\alpha\beta}$ is the Kronecker delta, and $\langle \dots \rangle$ denotes an average over the rods [38, 39]. To quantify the orientational order we measure

$$q_k = \int_0^\pi d\gamma h(\gamma) \cos(k\gamma), \quad k = \{2, 4\}, \quad (1)$$

where q_2 and q_4 are the uniaxial and tetratic order parameters, respectively. In an isotropic state (no orientational order) q_2 and q_4 vanish. In a uniaxial nematic state $q_2 > 0$ and $q_4 > 0$. Finally in a tetratic state $q_2 = 0$ and $q_4 > 0$. The states in Fig. 3 are selected such that

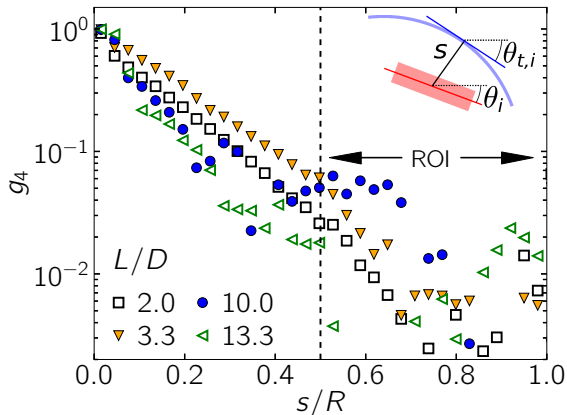


FIG. 4. (Color online) Wall-rod angular correlation function g_4 as a function of the rescaled distance s/R to the wall for various L/D . A sketch with various definitions is shown in the inset. The data are obtained through an average over all Γ , global area fraction Φ_g and experimental runs. The typical error for g_4 ($\sim 5 \times 10^{-3}$) is comparable to the size of the symbols for $s/R < 0.5$. Note the logarithmic scale on the y-axis.

q_2 and q_4 are comparable in both experiments and MC simulations.

B. Experiments: The influence of boundary and driving

Former experiments [32, 34, 40, 41] and MC simulations [39] show that the container induces a preferential alignment of the particles close to the wall. In order to facilitate the investigation in the bulk, we first need to characterize such an influence quantitatively.

Following the ideas in [32], we calculate the wall-rod angular correlation function $g_4(s) = \langle \cos[4(\theta_{t,i} - \theta_i(s))] \rangle$, where s is the shortest distance from the rod center to the container wall, $\theta_{t,i}$ is the tangential direction of the corresponding point on the wall (see inset in Fig. 4), and $\langle \dots \rangle$ denotes an average over all the particles at a distance s . Either homeotropic or planar alignment of the particles with respect to the wall results in $g_4 \sim 1$. In Fig. 4, g_4 is presented as a function of the rescaled distance to the wall s/R with a binning width of $0.03R$. For all aspect ratios investigated, g_4 decays exponentially with s/R . To minimize the influence of the wall, we consider only those particles with $s/R > 0.5$ to be in the ROI. In this region, g_4 is always smaller than 0.06 and remains in a range comparable to the experimental uncertainties. We characterize the state of the system by measuring the area fraction Φ and $h(\gamma)$ in circular regions with radius $3L$ inscribed in the ROI. Subsequently, we calculate $q_k(\Phi)$ from $h(\gamma)$ accumulated over all the regions that share the same Φ .

Figure 5 shows the order parameters as a function of

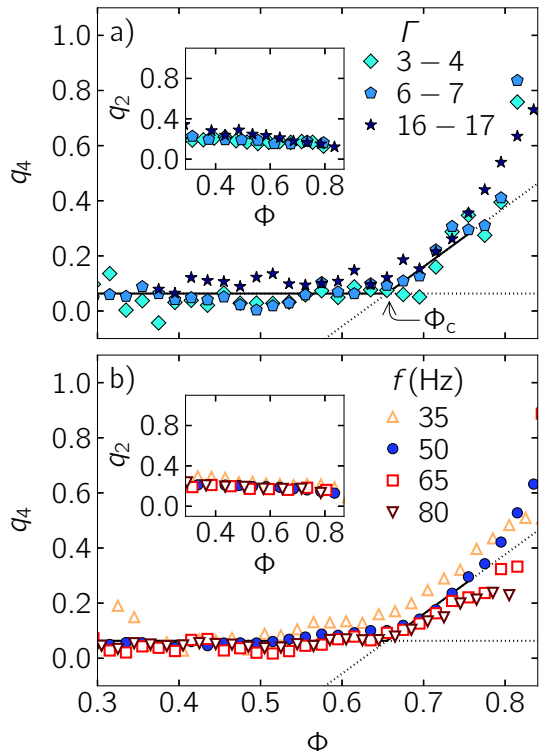


FIG. 5. (Color online) Tetratic q_4 and uniaxial q_2 order parameters in the ROI as a function of the area fraction Φ , for rods with aspect ratio $L/D = 3.3$. (a) For three ranges of peak acceleration Γ at $f = 50$ Hz and (b) for four frequencies obtained by accumulating over all Γ . The threshold Φ_c is obtained through linear fits to the data accumulated over all Γ for $f = 50$ Hz (see text for details). The order parameters are not exactly zero in the isotropic state due to the finite size of the system [38].

Φ for short rods with $L/D = 3.3$. It indicates an area fraction Φ_c above which the tetratic order parameter q_4 grows from its initial low value, while the uniaxial order parameter q_2 remains low. Such a combination of q_2 and q_4 suggests a gradual isotropic-tetratic (I-T) transition. As shown in (a), the behavior of q_2 and q_4 does not depend on the peak vibration acceleration. This is further confirmed through a comparison among data obtained for all Γ in the range of $2 \leq \Gamma \leq 20$ and also for all aspect ratios investigated. As shown in (b), a variation of the vibration frequency f from 35 Hz to 80 Hz for $L/D = 3.3$ also yields the same behavior of $q_k(\Phi)$.

Such agreements indicate that the details of how the rods are effectively ‘thermalized’ in our nonequilibrium system are not essential in determining the ordering transitions, providing us the opportunity to draw connections to the corresponding equilibrium systems. Accordingly, we accumulate the data over all Γ at $f = 50$ Hz for a more accurate characterization of the transition threshold Φ_c . By fitting q_4 with a constant value in the isotropic region and with a straight line in the ordered state, we obtain

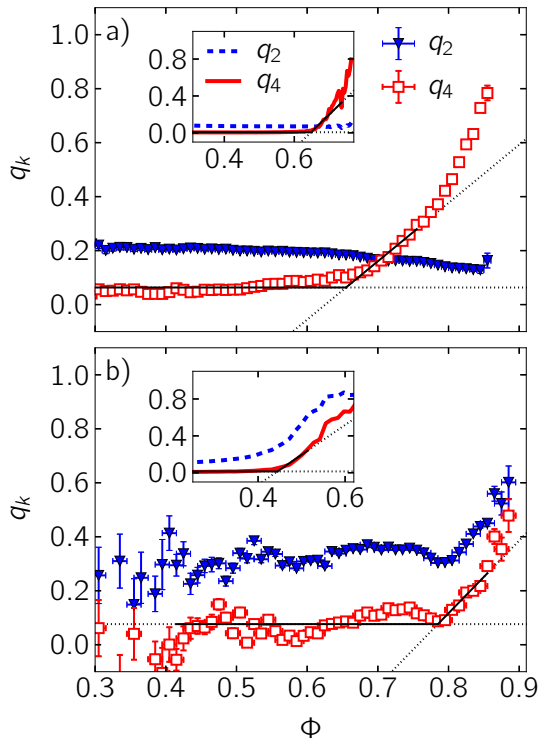


FIG. 6. (Color online) Tetratic and uniaxial order parameters q_k as a function of the area fraction Φ for a) $L/D = 3.3$ and b) $L/D = 10.0$. The insets show the corresponding results from MC simulations. The experimental data is an accumulation over all Γ at $f = 50$ Hz. Straight lines are linear fits to determine the threshold Φ_c .

Φ_c as the intersection point which minimizes the standard error. Only data with sufficient statistics (i.e. error bar < 0.02) and $q_4 < 0.3$ are chosen for the fits.

Moreover, the height of the container is found to play a minor role in determining the ordering transition: A variation of H/D from $4/3$ to 2 leads to the same behavior of q_k . Experiments with $H/D = 2$ for $L/D = 3.3$ and $L/D = 10.0$ give rise to slightly lower transition thresholds Φ_c . More specifically, we find a decrease of 12% for short rods and of 5% for long rods, which is in both cases within the uncertainty of the fit. In addition, for a specific aspect ratio of $L/D = 5.0$, the same experiments have been performed for two different rod diameters. The results agree with each other within the error bar, suggesting that the mass of the rods does not play a dominating role in the ordering transition.

C. Experiments vs. simulations and DFT

Based on the above characterizations of the boundary influence, we compare the ordering transitions of granular rods in the ROI to the corresponding thermal system. Figure 6 shows the averaged order parameters obtained in both experiments and MC simulations (insets)

for rods with $L/D = 3.3$ (a) and $L/D = 10.0$ (b). As discussed above, tetratic ordering occurs in the system of short rods. For long rods, both order parameters start to grow above Φ_c , suggesting a gradual I-U transition. Qualitatively, the agreement between experiments and MC simulations on the behavior of both tetratic q_4 and uniaxial q_2 order parameters is remarkable for both aspect ratios. Such similarities indicate that the ordering of granular rods is governed by the geometric constrain of non-overlapping rods, which is the only interaction considered in the simulations. Quantitatively, the threshold $\Phi_c = 0.66 \pm 0.11$ obtained experimentally for the I-T transition for rods with $L/D = 3.3$ agrees with the one 0.65 ± 0.02 obtained from MC simulations within the error. However, the experimentally obtained threshold $\Phi_c = 0.79 \pm 0.04$ of the I-U transition for rods with $L/D = 10.0$ is larger than the one obtained for the corresponding thermal system, 0.44 ± 0.03 .

As L/D and Φ are the key parameters determining the state of the system, we compare the experimental (nonequilibrium) results with the MC (equilibrium) simulations in a state diagram shown in Fig. 7. In both systems short rods form a tetratic state and long rods an uniaxial state at sufficiently high area fractions. The aspect ratio at which the ordered state changes from tetratic to uniaxial nematic agrees quantitatively. It is found to be $(L/D)_{T-U} \approx 7.3 \pm 0.7$ in both simulation and experiment [42]. This result agrees with previous simulations in which a tetratic phase was found for $L/D = 7$ and some evidence of uniaxial ordering for $L/D = 9$ [45]. The quantitative agreement of $(L/D)_{T-U}$ across systems in and out of thermodynamic equilibrium illustrates the universal aspect of the ordering transitions.

On the other hand, the threshold Φ_c for agitated rods differs from that in MC simulations, indicating the non-universal aspects of the ordering transitions. First, the experimentally determined Φ_c exhibit a peak around $(L/D)_{T-U}$. In contrast, MC simulations show a monotonic decay with L/D . Second, there exists a systematic deviation of Φ_c in experiments compared to MC simulations as L/D grows. For the largest aspect ratio investigated experimentally, $L/D = 13.3$, much higher area fraction is required for the uniaxial state to develop. This difference might be attributed to the following mechanisms. (i) The strong fluctuations in the nonequilibrium steady states of granular rods may lead to temporal disorder in a system that could in principle relax into an ordered state. (ii) Due to the dissipative rod-rod interactions, the tendency of clustering for granular rods is larger in comparison to MC simulations, especially for large L/D (compare panels (d) and (e) of Fig. 3). (iii) Finally, the container wall may frustrate the orientational order of the agitated rods in the entire cavity. Further experiments using containers with different sizes and shapes might shed light on such a discrepancy.

Concerning the fluctuations, it is known that the velocity distributions of agitated granular spheres are non-gaussian and exhibit exponential tails, no matter whether

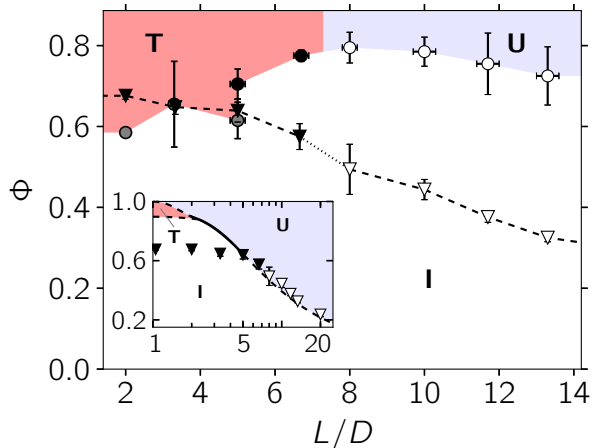


FIG. 7. (Color online) State diagram in the plane of aspect ratio L/D , and area fraction Φ obtained via experiments of agitated granular rods (circles) and MC simulations of thermally driven hard rectangles (triangles). The labels denote the states: isotropic (I), uniaxial nematic (U), and tetratic (T). They are colored according to the experimental data. The diameter of the rods used in the experiments is $D = 3.0$ mm for $L/D \leq 5$ and $D = 1.5$ mm for $L/D \geq 5$. Closed and open symbols indicate the I-T and I-U transitions, respectively. The inset shows the state diagram of equilibrium hard rods according to DFT in comparison to MC simulations in an extended region of L/D . Dashed lines are continuous transitions and solid lines denote first order transitions.

the particles form clusters [43] or not [44]. As the dissipative nature does not depend on the shape of the particles, we expect similar behavior in our system. This feature sets agitated granular rods apart from thermally driven liquid crystals, and triggers the question of how to define an effective ‘thermal’ energy scale for an athermal system. Experiments on monitoring the mobility of individual granular rods with high speed photography could help to shed light on the difference between thermal and athermal systems found here.

In the inset of Fig. 7 we show the state diagram according to DFT together with the thresholds obtained from MC simulations in an extended region of L/D . It is similar to the one predicted by the scaled particle theory [15]. DFT also predicts I-T transitions for small L/D and I-U transitions for large L/D . However, the tetratic state is stable only for $L/D \lesssim 2.2$, most likely because only two-body correlations are considered in the theory [16, 45]. Concerning the ordering transition threshold Φ_c , there is a good agreement between DFT and MC simulations for $L/D \gtrsim 7$. For low aspect ratios, the deviations between both approaches are due to the mean field character of the theory. In systems with $L/D < (L/D)_{T-U}$, DFT predicts a T-U transition at very high area fractions. Due to the limitations in both experiments and MC simulations, the region of very high area fractions, where the T-U transition may arise, has not been explored.

IV. CONCLUSIONS

To summarize, the ordering of agitated monodisperse granular rod monolayers is found to be determined predominantly by the aspect ratio of the rods and the area fraction, while the frequency and the strength of the agitation are not essential. It suggests that the detailed nature of energy injection into such a nonequilibrium system is not important, analogous to the role that temperature plays in equilibrium hard rod models. In comparison to former experimental investigations on monolayer systems, we have focused on the bulk region of the container and found both tetratic and uniaxial nematic ordering for cylindrical rods. This enables a direct comparison to the phase diagram of the corresponding equilibrium system. We find that, depending on whether the aspect ratio is smaller or larger than ≈ 7.3 , a gradual isotropic-tetratic or isotropic-uniaxial nematic transition arises for both systems as the area fraction grows. This agreement with the predictions from equilibrium MC simulations considering only excluded volume interactions suggests some degree of universality for the ordering of rod shaped particles across systems in and out of thermodynamic equilibrium. Nevertheless, we have also found a qualitative difference between both systems, namely the trend of the area fraction threshold at the ordering transitions.

Further investigations will focus on the characterization of the area fraction and velocity fluctuations of the system, in order to find an effective ‘thermal’ energy scale for such an athermal system. Moreover, a comparison to molecular dynamics simulations [46] with tunable rod-rod dissipation energy could help to elucidate how fluctuations influence the ordering transition threshold.

Appendix A: Density functional theory

We use an Onsager-like DFT with Parsons-Lee rescaling. A similar DFT was previously used to analyze the state diagram of two-dimensional rods confined in a circular cavity [47]. We are interested in the behavior of fluid states in which the density is spatially homogeneous. Hence we can write, without loss of generality, the one body density distribution as

$$\rho(\vec{r}, \gamma) = \rho h(\gamma), \quad (\text{A1})$$

where ρ is the number density and $h(\gamma)$ is the orientational distribution function. Here γ is the angle with respect to the director. $h(\gamma)$ is normalized such that

$$\int_0^\pi d\gamma h(\gamma) = 1. \quad (\text{A2})$$

We split the free energy into two parts

$$F[\rho] = F_{\text{id}}[\rho] + F_{\text{ex}}[\rho], \quad (\text{A3})$$

where F_{id} is the ideal gas part and F_{ex} is the excess part accounting for the excluded volume interactions. The

ideal free energy per unit of area A is given exactly by

$$\frac{\beta F_{\text{id}}[\rho]}{A} = \int_0^\pi d\gamma \rho h(\gamma) \ln(\Lambda \rho h(\gamma) - 1), \quad (\text{A4})$$

where $\beta = 1/k_{\text{B}}T$ with k_{B} the Boltzmann's constant and T the absolute temperature. Λ is the (irrelevant) thermal volume that we set to one. The excess part is approximated by

$$\frac{F_{\text{ex}}[\rho]}{A} = \frac{\psi_{\text{ex}}(\phi)}{4LD} \rho \int_0^\pi d\gamma_1 \int_0^\pi d\gamma_2 h(\gamma_1) h(\gamma_2) v_{\text{exc}}(\gamma_{12}). \quad (\text{A5})$$

$v_{\text{exc}}(\gamma_{12})$ is the excluded area between two rectangles with length L , width D and relative orientation γ_{12} :

$$v_{\text{exc}}(\gamma_{12}) = (L^2 + D^2)|\sin \gamma_{12}| + 2LD(1 + |\cos \gamma_{12}|), \quad (\text{A6})$$

and $\psi_{\text{ex}}(\phi)$ is the excess free energy per particle of a reference system of hard disks at the same area fraction $\phi = \rho LD$ as our system of hard rectangles. The diameter of the disks is selected such that both disks and rectangles have the same area. Following Baus and Colot [48] we approximate ψ_{ex} by:

$$\beta \psi_{\text{ex}}(\phi) = (c_2 + 1) \frac{\phi}{1 - \phi} + (c_2 - 1) \ln(1 - \phi), \quad (\text{A7})$$

with $c_2 = 7/3 - 4\sqrt{3}/\pi \approx 0.1280$. Eq. (A5) recovers the Onsager approximation in the low density limit.

Finally, the grand potential is given by

$$\Omega[\rho]/A = F[\rho]/A - \mu\rho, \quad (\text{A8})$$

with μ the chemical potential. We minimize Ω with respect to ρ and $h(\gamma)$ in order to find the equilibrium states. We use a standard conjugated gradient method to minimize the functional. We use a truncated Fourier expansion to describe $h(\gamma)$. We truncate the expansion such that the absolute value of the last coefficient in the expansion is smaller than 10^{-7} .

ACKNOWLEDGMENTS

The authors would like to thank Wilhelm August for the preliminary work on the experimental set-up. Inspiring discussions with M. Schmidt, D. van der Meer, and C. Krülle are greatly acknowledged. TM and KH acknowledge the support from the DFG through Grant No. HU1939/2-1.

-
- [1] M. J. Stephen and J. P. Straley, *Rev. Mod. Phys.* **46**, 617 (1974).
 - [2] P. G. de Gennes and J. Prost, *The Physics of Liquid Crystals* (Clarendon Press, 1995).
 - [3] L. Onsager, *Ann. N. Y. Acad. Sci.* **51**, 627 (1949).
 - [4] G. J. Vroege and H. N. W. Lekkerkerker, *Rep. Prog. Phys.* **55**, 1241 (1992).
 - [5] H. P. Zhang, A. Beer, E.-L. Florin, and H. L. Swinney, *PNAS* **107**, 13626 (2010).
 - [6] V. Schaller, C. Weber, C. Semmrich, E. Frey, and A. R. Bausch, *Nature* **467**, 73 (2010).
 - [7] T. Sanchez, D. T. N. Chen, S. J. DeCamp, M. Heymann, and Z. Dogic, *Nature* **491**, 431 (2012).
 - [8] J. Buhl, *Science* **312**, 1402 (2006).
 - [9] I. D. Couzin, J. Krause, N. R. Franks, and S. A. Levin, *Nature* **433**, 513 (2005).
 - [10] Q.-X. Liu, A. Doelman, V. Rottschäfer, M. d. Jager, P. M. J. Herman, M. Rietkerk, and J. v. d. Koppel, *PNAS* **110**, 11905 (2013).
 - [11] S. Zhou, A. Sokolov, O. D. Lavrentovich, and I. S. Aranson, *PNAS* **111**, 1265 (2014).
 - [12] D. Frenkel, *Physica A* **263**, 26 (1999).
 - [13] K. W. Wojciechowski and D. Frenkel, *Comput. Methods Sci. Technol.* **10**, 235 (2004).
 - [14] A. Donev, J. Burton, F. H. Stillinger, and S. Torquato, *Phys. Rev. B* **73**, 054109 (2006).
 - [15] Y. Martínez-Ratón, E. Velasco, and L. Mederos, *J. Chem. Phys.* **122**, 064903 (2005).
 - [16] Y. Martínez-Ratón and E. Velasco, *Phys. Rev. E* **79**, 011711 (2009).
 - [17] J. Geng and J. V. Selinger, *Phys. Rev. E* **80**, 011707 (2009).
 - [18] H. M. Jaeger, S. R. Nagel, and R. P. Behringer, *Rev. Mod. Phys.* **68**, 1259 (1996).
 - [19] G. H. Ristow, G. Straßburger, and I. Rehberg, *Phys. Rev. Lett.* **79**, 833 (1997).
 - [20] A. Götzendorfer, C.-H. Tai, C. A. Krüelle, I. Rehberg, and S.-S. Hsiau, *Phys. Rev. E* **74**, 011304 (2006).
 - [21] P. Eshuis, K. van der Weele, D. van der Meer, R. Bos, and D. Lohse, *Phys. Fluids* **19**, 123301 (2007).
 - [22] A. Fingerle, K. Roeller, K. Huang, and S. Herminghaus, *New J. Phys.* **10**, 053020 (2008).
 - [23] K. Huang, C. Krülle, and I. Rehberg, *Zeit. Angew. Math. Mech.* **90**, 911 (2010).
 - [24] C. May, M. Wild, I. Rehberg, and K. Huang, *Phys. Rev. E* **88**, 062201 (2013).
 - [25] T. Börzsönyi and R. Stannarius, *Soft Matter* **9**, 7401 (2013).
 - [26] D. L. Blair, T. Neicu, and A. Kudrolli, *Phys. Rev. E* **67**, 031303 (2003).
 - [27] I. S. Aranson, D. Volfson, and L. S. Tsimring, *Phys. Rev. E* **75**, 051301 (2007).
 - [28] V. Narayan, S. Ramaswamy, and N. Menon, *Science* **317**, 105 (2007).
 - [29] I. S. Aranson, A. Snezhko, J. S. Olafsen, and J. S. Urbach, *Science* **320**, 612 (2008).
 - [30] K. Harth, U. Kornek, T. Trittel, U. Strachauer, S. Höme, K. Will, and R. Stannarius, *Phys. Rev. Lett.* **110**, 144102 (2013).
 - [31] N. Kumar, H. Soni, S. Ramaswamy, and A. K. Sood, *Nat. Commun.* **5**, 4688 (2014).
 - [32] J. Galanis, D. Harries, D. L. Sackett, W. Losert, and

- R. Nossal, Phys. Rev. Lett. **96**, 028002 (2006).
- [33] J. Galanis, R. Nossal, and D. Harries, Soft Matter **6**, 1026 (2010).
- [34] V. Narayan, N. Menon, and S. Ramaswamy, J. Stat. Mech. **2006**, P01005 (2006).
- [35] R. Sánchez and A. Huerta, Rev. Mex. Fis. **60**, 119 (2014).
- [36] V. Yadav, J.-Y. Chastaing, and A. Kudrolli, Phys. Rev. E **88**, 052203 (2013).
- [37] M. P. Allen and D. J. Tildesley, *Computer simulation of liquids* (Oxford University Press, 1987).
- [38] J. A. Cuesta and D. Frenkel, Phys. Rev. A **42**, 2126 (1990).
- [39] D. de las Heras and E. Velasco, Soft Matter **10**, 1758 (2014).
- [40] J. Galanis, R. Nossal, W. Losert, and D. Harries, Phys. Rev. Lett. **105**, 168001 (2010).
- [41] A. Kudrolli, G. Lumay, D. Volfson, and L. S. Tsimring, Phys. Rev. Lett. **100**, 058001 (2008).
- [42] This value represents the average between $L/D = 6.6$ (uniaxial) and $L/D = 8$ (tetratic).
- [43] J. S. Olafsen and J. S. Urbach, Phys. Rev. Lett. **81**, 4369 (1998).
- [44] A. Kudrolli and J. Henry, Phys. Rev. E **62**, R1489 (2000).
- [45] Y. Martínez-Ratón, E. Velasco, and L. Mederos, J. Chem. Phys. **125**, 014501 (2006).
- [46] D. Volfson, A. Kudrolli, and L. S. Tsimring, Phys. Rev. E **70**, 051312 (2004).
- [47] D. de las Heras, E. Velasco, and L. Mederos, Phys. Rev. E **79**, 061703 (2009).
- [48] M. Baus and J. L. Colot, Phys. Rev. A **36**, 3912 (1987).

2.4 Scaling of the Normal Coefficient of Restitution for Wet Impacts

Authors: Thomas Müller, Frank Gollwitzer, Christof A. Krülle, Ingo Rehberg, and Kai Huang

Journal: AIP Conference Proceedings

Volume: 1542

Pages: 787–790

Date of publication: June 18, 2013

DOI: <http://dx.doi.org/10.1063/1.4812049>

© 2013 AIP Publishing

Scaling of the Normal Coefficient of Restitution for Wet Impacts

Thomas Müller*, Frank Gollwitzer*, Christof A. Krülle†, Ingo Rehberg* and Kai Huang*

**Experimentalphysik V, Universität Bayreuth, 95440 Bayreuth, Germany*

†*Maschinenbau und Mechatronik, Hochschule Karlsruhe - Technik und Wirtschaft, 76133 Karlsruhe, Germany*

Abstract. A thorough understanding of the energy dissipation in the dynamics of wet granular matter is essential for a continuum description of natural phenomena such as debris flow, and the development of various industrial applications such as the granulation process. The coefficient of restitution (COR), defined as the ratio between the relative rebound and impact velocities of a binary impact, is frequently used to characterize the amount of energy dissipation associated. We measure the COR by tracing a freely falling sphere bouncing on a wet surface with the liquid film thickness monitored optically. For fixed ratio between the film thickness and the particle size, the dependence of the COR on the impact velocity and various properties of the liquid film can be characterized with the Stokes number, defined as the ratio between the inertia of the particle and the viscosity of the liquid. Moreover, the COR for infinitely large impact velocities derived from the scaling can be analyzed by a model considering the energy dissipation from the inertia of the liquid film.

Keywords: coefficient of restitution, impact, wetting, particle-laden flow, granular flow

PACS: 45.70.-n, 45.50.Tn, 47.55.Kf

INTRODUCTION

Understanding the energy dissipation associated with particle-particle interactions is crucial for describing the collective behavior of granular matter [1], i.e., large agglomerations of macroscopic particles. The coefficient of restitution (COR), firstly introduced by Newton as the ratio between relative rebound and impact velocities [2], can be used to characterize the energy dissipation at the particle level. This number provides one of the basic ingredients of computer assisted modeling, such as molecular dynamics (MD) simulation, which has been developed into a powerful tool to describe the large scale collective behavior of granular matter in the past decades [3, 4]. Besides the energy dissipation from particle-particle interactions, the dissipation arising from the interstitial air or liquid has to be considered when coping with natural phenomena such as dune migration [5] or debris flow [6], as well as with various industrial applications such as granulation process [7, 8].

The experience of building sand sculptures tells us that the rigidity of a granular material increases as a small amount of a wetting liquid is added. This is largely due to the cohesion arising from the formation of capillary bridges between adjacent particles [9]. The so-called wet granular matter behaves dramatically different from non-cohesive dry granular matter while agitated, with emerging critical behavior, such as phase transitions [10] and pattern formations [11], being traceable to the energy or force scale of a single capillary bridge. In order to gain

insights into the dynamical behavior of wet granular matter, it is essential to explore the COR and the associated energy dissipation of wet impacts. A recent investigation reveals that the dependence of the COR on various particle and liquid properties can be scaled with two dimensionless numbers: the ratio between the inertia of the particle and the viscosity of the liquid (Stokes number), and that between the liquid film thickness and the size of the particle [12]. Here, further experimental results with a different density ratio between the particle and the wetting liquid are presented, in order to test the scaling of the COR with these three dimensionless numbers.

EXPERIMENTAL PROCEDURE

We measure the COR by recording a freely falling sphere with a highspeed camera (Photron, Fastcam Super 10K) at a frame rate up to 500 fps. Using a Hough transformation, the center of the sphere can be tracked in the images and the position of the sphere can be plotted against time (see Fig. 1). Fitting parabolic curves on the trajectories results in crossing points, which represent the time when the sphere hits the ground. The height of the crossing points varies slightly, owing to the various distance of the bouncing point to the camera. The slopes of the two fitted parabolae at each crossing point yield the impact velocity v_{imp} and the rebound velocity v_{reb} of the sphere, respectively. Hence the normal coefficient of restitution $e_n = v_{\text{reb}}/v_{\text{imp}}$ can be determined for

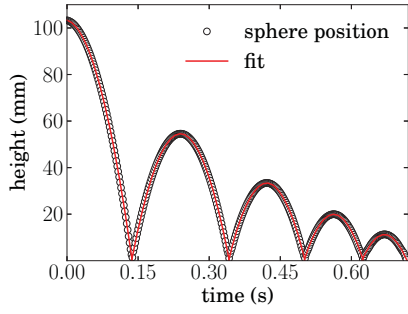


FIGURE 1. Typical trajectory of a bouncing sphere. The diagram shows a PE sphere of diameter $D = 7.9$ mm bouncing on a glass plate covered with a $190 \mu\text{m}$ thick silicone oil (M5) film.

every impact. Polyethylene (PE) spheres with various diameter D and a density $\rho_p = 0.94 \text{ g/cm}^3$ are cleaned and pre-wetted before use. Two types of silicone oil (M5 and M50 from Carl Roth) with different dynamic viscosities $\eta = 4.6 \text{ mPa} \cdot \text{s}$ for M5 and $48 \text{ mPa} \cdot \text{s}$ for M50, and similar densities $\rho_{\text{liq}} = 0.93 \text{ g/cm}^3$ and 0.97 g/cm^3 for M5 and M50 correspondingly are used. The bottom of the glass container, which has an inner area of $A = 100 \text{ cm}^2$ is leveled within 0.03 degrees to ensure a horizontal surface and a uniform initial liquid film thickness. A sketch of the set-up and a more detailed description can be found in Ref. [12].

To investigate the influence of the liquid film on the COR, an accurate determination of its thickness is essential. Here, the thickness is measured optically by detecting the deflection of a laser beam (see Fig. 2 a) guided through the liquid film. The laser beam hits the glass plate with an incident angle of α and a refractive angle $\beta = \arcsin(n_{\text{air}} \sin \alpha / n_{\text{glass}})$, where n_{air} and n_{glass} are the refractive indices of air and glass, respectively. Without a liquid film, a part of the beam is reflected at the glass–air interface and then reflected at a mirror at the bottom of the glass plate. After a few reflections $j_0 = 4$, determined by the length of the mirror), the beam passes through the bottom of the glass plate again and is detected by a CCD camera.

With a liquid film of thickness h_{liq} on top of the glass plate, one reflection of the beam within the liquid film leads to a horizontal shift of the beam by a distance $l_{\text{liq}} = 2h_{\text{liq}} \tan \gamma$, with the refractive angle in the liquid $\gamma = \arcsin(n_{\text{glass}} \sin \beta / n_{\text{liq}}) = \arcsin(n_{\text{air}} \sin \alpha / n_{\text{liq}})$.

For the typical case that the number of reflections at the air–liquid interface j_{liq} is the same as that in the dry glass plate (Fig. 2 a), the total shift of the laser beam along the horizontal plane is $j_{\text{liq}} \cdot l_{\text{liq}}$ with $j_{\text{liq}} = j_0$. It is also possible, as shown in Fig. 2 b, to detect

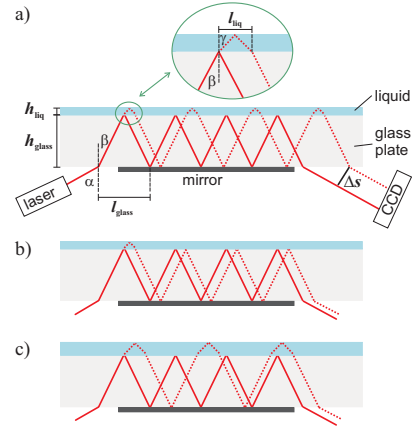


FIGURE 2. a) A sketch of the film thickness determination part of the setup. The solid lines show the beam for a dry container, the dashed lines illustrate the deviation with a liquid layer on top of the glass plate. Number of shifts by passing through the glass plate $j_{\text{glass}} = 4$, number of reflections in the liquid film $j_{\text{liq}} = 4$. b) $j_{\text{glass}} = 4$, $j_{\text{liq}} = 1$. c) $j_{\text{glass}} = 3$, $j_{\text{liq}} = 3$.

reflected beams with a smaller number of passes through the liquid film ($j_{\text{liq}} < j_0$), due to partial reflections at the glass–liquid interface. If the filling level is too high and consequently the shift of the beam is too big, an additional reduction of reflections in the glass plate to $j_{\text{glass}} < j_0$ is also possible (Fig. 2 c). In such a case, a negative shift of $(j_0 - j_{\text{glass}}) \cdot l_{\text{glass}}$ has to be considered, where $l_{\text{glass}} = 2h_{\text{glass}} \tan \beta$ is a constant value.

Taking all the above possibilities into account, the reflected beams leave the glass with a horizontal shift which results in

$$\Delta s = [j_{\text{liq}} \cdot l_{\text{liq}} - (j_0 - j_{\text{glass}}) \cdot l_{\text{glass}}] \cos \alpha \quad (1)$$

at the CCD. Consequently, the liquid film thickness can then be calculated by

$$h_{\text{liq}} = \frac{\Delta s}{\cos \alpha} + \frac{2(j_0 - j_{\text{glass}})h_{\text{glass}} \tan \beta}{2j_{\text{liq}} \tan \gamma} \quad (2)$$

Note that for thin films (when $j_0 - j_{\text{glass}} = 0$), h_{liq} is independent on the properties of the glass plate.

Experimentally, the camera captures a series of spots with each of them corresponding to a certain combination of j_{liq} and j_{glass} . The brightest spot corresponds to the case $j_{\text{liq}} = j_{\text{glass}} = j_0$, therefore it is commonly used for the film thickness measurement. Figure 3 shows a comparison of the film thickness obtained from V/A , with V the volume of liquid added, and h_{liq} given by Eq. 2. With a certain V , the multiple spots detected give rise to multiple Δs . As V increases, the shift of each spot Δs follows a linear growth with various slopes and offset-

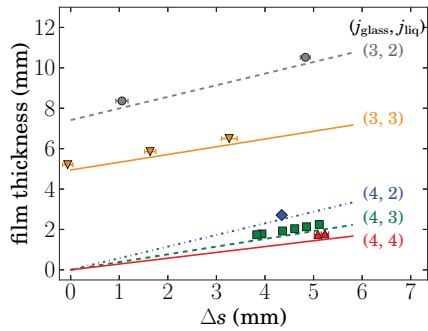


FIGURE 3. The relation between the water film thickness and the shift of the laser beam Δs at the CCD predicted from Eq. 2 (solid lines) and estimated with V/A , the total liquid volume over the area of the container (data points).

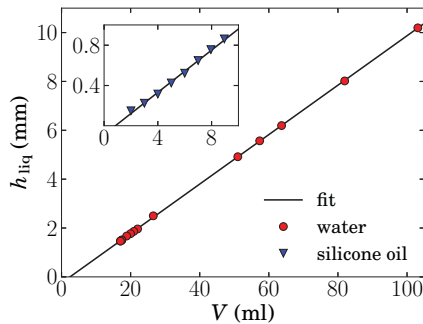


FIGURE 4. The film thickness obtained with Δs and Eq. 2 as a function of the filling volume of water and silicone oil (inset). The error bars are within the size of the symbols. Linear fits of the data with $h_{liq} = k(V - V_{men})$ yield the same $k = 0.01 \text{ cm}^{-2}$ for both liquids, and $V_{men} = (2.45 \pm 0.10) \text{ ml}$ for water and $(0.84 \pm 0.15) \text{ ml}$ for silicone oil.

s, which follows the prediction based on Eq. 2 with various combination of j_{liq} and j_{glass} . The systematic overestimation of the film thickness from V/A for all data sets is presumably due to the volume of the liquid captured in the meniscus of the liquid film V_{men} , since the systematic deviation from the estimation of Eq. 2 does not depend on the parameters j_{liq} and j_{glass} .

Therefore, using the variation of any spot detected by the camera, not only the brightest one, we can measure the liquid film thickness h_{liq} . This additional information from the spots with smaller intensity gives the opportunity to expand the range of h_{liq} that can be detected, provided that the free parameters j_{liq} and j_{glass} have been correctly determined from the first few data points.

Figure 4 shows that the optically obtained film thickness grows linearly with the liquid volume V , giving rise to a slope $k = 1/A$ and an estimation of the meniscus volume V_{men} . Therefore, an estimation of h_{liq} with V/A

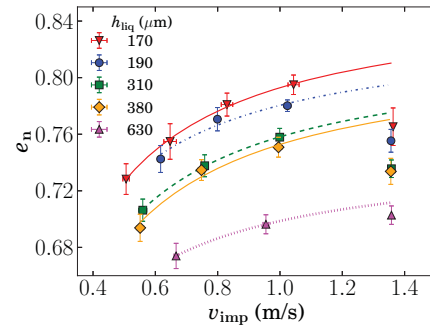


FIGURE 5. Normal coefficient of restitution ϵ_n against the impact velocity v_{imp} for a PE sphere of fixed diameter $D = 7.9 \text{ mm}$ at different silicone oil M5 film thickness h_{liq} .

is also appropriate, provided that the meniscus volume is subtracted. Nevertheless, the optical way provides a real-time monitoring of the film thickness. This will be helpful in future analysis on surface waves generated by the impact, and in monitoring the loss of liquid due to evaporation. The small deviation from the linear fit for the silicone oil film thickness data (inset of Fig. 4) indicates a correlation between V_{men} and h_{liq} for thin films, which we leave to future investigations. Figure 4 also shows the possibility to measure the film thickness up to 1 cm combining the information from various spots detected. The error of h_{liq} , on the order of $\approx 10 \mu\text{m}$, arises mainly from the fluctuations of the spot intensity. At a larger film thickness, the spots will become too weak to be detected accurately by the camera. For thin films, silicone oil instead of water is preferable, because its low surface tension prevents the dewetting instability. Thus it is used for the following experiments.

RESULTS AND DISCUSSION

Towards a comprehensive understanding of the dependence of the COR for wet impacts on various liquid and particle properties, previous experiments with glass beads have revealed that the Stokes number and the dimensionless film thickness $\tilde{h} = h_{liq}/D$ can characterize the influence from inertia and viscous damping on the COR [12]. The Stokes number is defined as $St = \rho_p D v_{imp} / 9\eta$. Here, we test the scaling with PE particles, which correspond to a density ratio $\tilde{\rho} = \rho_{liq} / \rho_p \approx 1$. Without the liquid, the COR for the PE particle on the glass plate, depending weakly on v_{imp} for the range of interest here, is measured to be 0.88 ± 0.03 , averaged over 368 bouncing events.

Figure 5 shows the COR measured with an initial falling height of 9.5 cm and various film thicknesses h_{liq} .

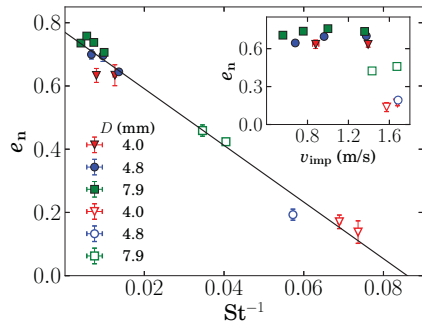


FIGURE 6. Normal coefficient of restitution e_n against the inverse Stokes number St^{-1} for a fixed $\tilde{h} \approx 0.04$. Data with closed and open symbols present measurements with silicone oil M5 and M50 correspondingly. The inset shows the same data, but plotted against v_{imp} .

The number of data points for each h_{liq} corresponds to the number of bouncings used for extrapolating the COR. The error bar arises from the statistics over 8-10 runs of the experiment. Except for the first bouncing data (the one with largest v_{imp}), the monotonic growth of the COR with v_{imp} could be fitted with $e_n = e_{inf}(1 - v_c/v_{imp})$, giving rise to a limiting COR e_{inf} at $v_{imp} \rightarrow \infty$ and a critical impact velocity v_c below which no rebound would occur. The decrease of the COR with the increase of h_{liq} clearly suggests the influence of the viscous damping, since the energy dissipated through a viscous force depends on the distance that the particle travels during the impact. Different from the case of glass beads [12], the COR for the first rebound is smaller than the fitted line for all film thicknesses. This could be attributed to the much stronger influence from the mass of liquid added to the particle during the first bouncing for the less dense PE sphere.

Besides the liquid film thickness, the COR depends also strongly on the viscosity of the wetting liquid. As shown in the inset of Fig. 6, the COR measured with silicone oil M50 as wetting liquid yields much lower values than those measured with M5. A re-plot of the COR with St^{-1} in Fig. 6 denotes a linear decay, suggesting that the dependence of the COR on h_{liq} , viscosity η and the impact velocity v_{imp} could be characterized by the Stokes number for fixed \tilde{h} . A linear fit with $e_n = e_{inf}(1 - St_c/St)$ yields a saturated COR $e_{inf} = 0.77 \pm 0.04$ and a critical Stokes number $St_c = 11.64 \pm 1.55$. Following a former theory [12], we could estimate $e_{inf} = e_{dry} - 3\tilde{\rho}\tilde{h}/2e_{dry} = 0.81 \pm 0.03$, which agrees with the measurement within the experimental uncertainties. This agreement suggests that the fact that e_{inf} is smaller than e_{dry} is due to the inertia of the wetting liquid, which provides the dependence on $\tilde{\rho}$ and \tilde{h} .

CONCLUSION

To conclude, the normal coefficient of restitution for the impact between a spherical particle and a flat surface covered with a liquid film is investigated for various impact velocities, particle and liquid properties. The technique to determine the film thickness optically and the calibration results are described in detail. Compared with the former methods [12], it provides an extended upper limit of the film thickness, and also allows the possibility to estimate the volume of the meniscus. At a certain density and size ratio, the COR is found to decay linearly with St^{-1} , which represents the scaling with the impact velocity and various particle as well as liquid properties. The parameter e_{inf} obtained from the fitting, corresponding to the saturated value of the COR, can be understood by a model considering the inertia of the liquid. A more detailed comparison to the model with various combinations of \tilde{h} and $\tilde{\rho}$ will be a focus of our further investigations.

ACKNOWLEDGMENT

We thank L. Meissner for performing the dry COR measurements. We are grateful for the support from Deutsche Forschungsgemeinschaft through HU1939/2-1.

REFERENCES

1. J. Duran, *Sands, Powders and Grains*, Springer, New York, 2000.
2. I. Newton, *Mathematical Principles of Natural Philosophy*, 1687, axioms, or Laws of motion. Corollary VI.
3. C. Bizon, M. D. Shattuck, J. B. Swift, W. D. McCormick, and H. L. Swinney, *Phys. Rev. Lett.* **80**, 57–60 (1998).
4. N. Brilliantov, and T. Poeschel, *Kinetic theory of granular gases*, Oxford Univ. Press, 2004.
5. R. A. Bagnold, *The physics of blown sand and desert dunes*, Methuen, London, 1941.
6. R. M. Iverson, *Rev. Geophys.* **35**, 245 (1997).
7. S. M. Iveson, J. D. Litster, K. Hapgood, and B. J. Ennis, *Powd. Technol.* **117**, 3 (2001).
8. S. Antonyuk, S. Heinrich, N. Deen, and H. Kuipers, *Particuology* **7**, 245 (2009).
9. M. Scheel, R. Seemann, et al., *Nature Mater.* **7**, 189 (2008).
10. A. Fingerle, K. Röller, K. Huang, and S. Herminghaus, *New J. Phys.* **10**, 053020 (2008).
11. K. Huang, and I. Rehberg, *Phys. Rev. Lett.* **107**, 028001 (2011).
12. F. Gollwitzer, I. Rehberg, C. A. Kruehle, and K. Huang, *Phys. Rev. E* **86**, 011303 (2012).

A Appendix

Distortion Factor of the Shaking Device

In the granular rods experiments, a commercial vibration system 50350-120 from TIRA GmbH was used to induce a continuous agitation of the particles. The sinusoidal signal was generated with a waveform generator 33220A from Agilent, connected to the power amplifier of the vibration system. The circular confinement, containing the monolayer of particles, was mounted on top of the shaking device. Its motion along the vertical direction (z -axis) is described by $z(t) = z_0 \sin(2\pi ft)$. Further details on the setup are described in the third publication (section 2.3). Information about the construction of the circular container can also be found in the diploma thesis written by Wilhelm August (2008).

In typical experiments, the driving frequency f was in the range of 30 Hz to 80 Hz. The shaking amplitude of the container was varied by changing the amplitude of the raw signal at the waveform generator. With a constant amplification, this yielded various peak accelerations $\Gamma = 4\pi^2 f^2 z_0 / g$ of the confinement, normalized by the gravitational constant g . Typically, z_0 was in the range of 0.2 mm to 2 mm. The acceleration of the container was logged using a Dytran 3035B2 acceleration sensor at a sampling rate of 10 kHz. A sinusoidal fit of the acceleration signal resulted in an estimation of the peak acceleration Γ . In order to characterize the harmonic distortion, the FFT of the acceleration signal was analyzed. The distortion factor

$$k = \sqrt{\frac{U_2^2 + U_3^2 + U_4^2 + \dots}{U_1^2 + U_2^2 + U_3^2 + \dots}} \quad (\text{A.1})$$

was calculated from the amplitudes U_i corresponding to the i -th harmonic. Figure A.1 shows the distortion factor k for various peak accelerations Γ at a fixed frequency of $f = 50$ Hz. The data were recorded under four different circumstances:

- i) Without any load of the shaking device. The acceleration sensor was mounted directly on the base plate of the shaker.
- ii) With the empty container mounted on the base plate. The acceleration sensor was attached to the container.
- iii) The container was mounted, including 400 granular polyvinyl chloride rods (length 1 cm, diameter 3 mm). This corresponds to a total area fraction of around 0.4.

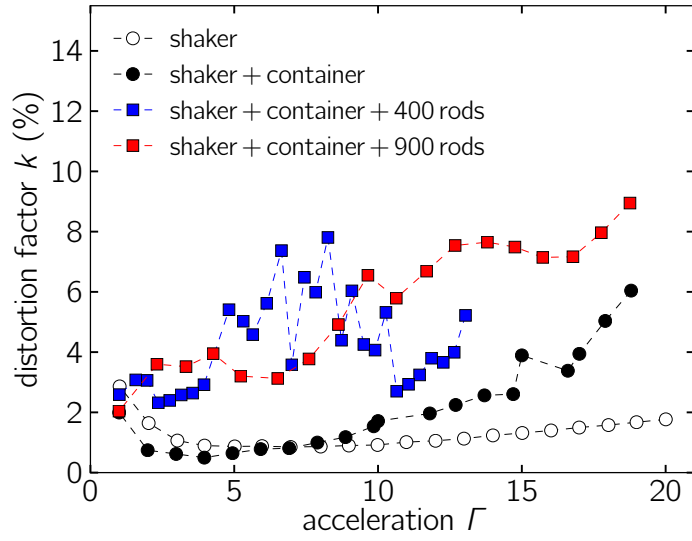


Figure A.1: Distortion factor as a function of the dimensionless peak acceleration Γ at a frequency of $f = 50$ Hz. Open symbols correspond to measurements of the unloaded shaker. Closed symbols correspond to the acceleration data of the mounted container, loaded with various portions of particles.

- iv) The container was mounted and filled with 900 rods, which corresponds to a total area fraction of around 0.8.

According to the data that are shown in Fig. A.1, the harmonic distortion of the vibration system without any load is below $k = 2\%$. The application of the empty confinement already influences the sinusoidal movement. In comparison to the unloaded shaking device, the harmonic distortion is bigger for peak accelerations above $\Gamma \approx 10$. For typical amplitudes used in the experiments, the distortion factor for an empty confinement remains below $k = 6\%$. Furthermore, Fig. A.1 illustrates the strong influence of the addition of granular particles to the container. The collective motion of the particles causes an additional vibration leading to the distortion of the mainly sinusoidal movement.

Bibliography

- ACHARD, M. F., BEDEL, J. PH., MARCEROU, J. P., NGUYEN, H. T. & ROUILLON, J. C. 2003 Switching of banana liquid crystal mesophases under field. *Eur. Phys. J. E* **10**, 129–134.
- AUGUST, W. 2008 Granulare Dynamik nichtsphärischer Partikel in einem Schwingförderer. *Diploma Thesis* (Universität Bayreuth).
- BALL, P. 2004 *The self-made tapestry: Pattern formation in nature*. Oxford University Press.
- BALLAUFF, M. 1986 Phase Equilibria in Mixtures of Thermotropic Liquid Crystals and Flexible Polymers. *Mol. Cryst. Liq. Cryst.* **136**, 175–195.
- BLINOV, L. M. & CHIGRINOV, V. G. 1996 *Electrooptic Effects in Liquid Crystal Materials*. Springer Verlag.
- BOGI, A. & FAETTI, S. 2001 Elastic, dielectric and optical constants of 4'-pentyl-4-cyanobiphenyl. *Liq. Cryst.* **28**, 729–739.
- BÖRZSÖNYI, T. & STANNARIUS, R. 2013 Granular materials composed of shape-anisotropic grains. *Soft Matter* **9**, 7401–7418.
- BÖRZSÖNYI, T., SZABÓ, B., TÖRÖS, G., WEGNER, S., TÖRÖK, J., SOMFAI, E., BIEN, T. & STANNARIUS, R. 2012 Orientational Order and Alignment of Elongated Particles Induced by Shear. *Phys. Rev. Lett.* **108**, 228302.
- BROCHARD, F. 1979 Viscosities of Dilute Polymer Solutions in Nematic Liquids. *J. Polym. Sci., Polym. Phys. Ed.* **17** (8), 1367–1374.
- BROWN, E., RODENBERG, N., AMEND, J., MOZEIKA, A., STELTZ, E., ZAKIN, M. R., LIPSON, H. & JAEGER, H. M. 2010 Universal robotic gripper based on the jamming of granular material. *PNAS* **107** (44), 18809–18814.
- BUCHALTER, B. J. & BRADLEY, R. M. 1992 Orientational order in random packings of ellipses. *Phys. Rev. A* **46** (6), 3046–3056.
- CANGIALOSI, D., BOUCHER, V. M., ALEGRÍA, A. & COLMENERO, J. 2013 Physical aging in polymers and polymer nanocomposites: recent results and open questions. *Soft Matter* **9**, 8619–8630.
- CHANDRASEKHAR, S. 1994 *Liquid Crystals*, 2nd edition. Cambridge University Press.

Bibliography

- CIFERRI, A. (ed.) 1991 *Liquid Crystallinity in Polymers: Principles and Fundamental Properties*. VCH Publishers, Inc.
- DURAN, J. 2000 *Sands, Powders, and Grains*. Springer.
- FLORY, P. J. 1956 Phase equilibria in solutions of rod-like particles. *Proc. R. Soc. A* **234**, 73–89.
- FRIEDEL, G. 1922 The Mesomorphic States of Matter (Les états mésomorphes de la matière). *Annales de Phys.* **18**, 273–474, (transl. extracts).
- GALANIS, J., NOSSAL, R. & HARRIES, D. 2010a Depletion forces drive polymer-like self-assembly in vibrofluidized granular materials. *Soft Matter* **6**, 1026–1034.
- GALANIS, J., NOSSAL, R., LOSERT, W. & HARRIES, D. 2010b Nematic Order in Small Systems: Measuring the Elastic and Wall-Anchoring Constants in Vibrofluidized Granular Rods. *Phys. Rev. Lett.* **105**, 168001.
- DE GENNES, P.G. & PROST, J. 2006 *The Physics of Liquid Crystals*, 2nd edition. Oxford University Press.
- GIBBS, J. W. 1878 On the Equilibrium of Heterogeneous Substances (Abstract by the Author). *Am. J. of Sci.* **16** (3).
- GIBBS, J. W. 2015 APS Physics Historic Sites about J. W. Gibbs. URL <http://www.aps.org/programs/outreach/history/historicsites/index.cfm>, (20.01.2015).
- GOLLWITZER, F., REHBERG, I., KRUELLE, C. A. & HUANG, K. 2012 Coefficient of restitution for wet particles. *Phys. Rev. E* **86**, 011303.
- GRAY, G. W., HARRISON, K. J. & NASH, J. A. 1973 New family of nematic liquid crystals for displays. *Electronics Letters* **9** (6), 130–131.
- HAGEN, G. H. L. 1852 Über den Druck und die Bewegung des trocknen Sandes. *Bericht über die zur Bekanntmachung geeigneten Verhandlungen der Königlich Preussischen Akademie der Wissenschaften zu Berlin* pp. 35–42.
- HARDIE, C. 1966 *The Six-Cornered Snowflake by Johannes Kepler (translation by Colin Hardie)*. Clarendon Press.
- HERMANS, J. JR. 1962 The Viscosity of Concentrated Solutions of Rigid Rodlike Molecules. *J. Colloid Sci.* **17**, 638–648.
- HERSHKOVITS, E., TANNENBAUM, A. & TANNENBAUM, R. 2008 Adsorption of Block Copolymers from Selective Solvents on Curved Surfaces. *Macromolecules* **41**, 3190–3198.
- HERTZ, H. 1882 Ueber die Berührung fester elastischer Körper. *J. reine und angewandte Mathematik* **92**, 156–171.

- HINRICHSEN, H. & WOLF, D. E. (eds.) 2004 *The Physics of Granular Media*. Wiley-VCH Verlag.
- HUANG, K., BRINKMANN, M. & HERMINGHAUS, S. 2012 Wet granular rafts: aggregation in two dimensions under shear flow. *Soft Matter* **8**, 11939–11948.
- JAEGER, G. 1998 The Ehrenfest Classification of Phase Transitions: Introduction and Evolution. *Arch. Hist. Exact. Sci.* **53**, 51–81.
- JAEGER, H. M., NAGEL, S. R. & BEHRINGER, R. P. 1996 Granular solids, liquids, and gases. *Rev. Mod. Phys.* **68** (4), 1259–1273.
- DE JEU, W. H. 1980 *Physical properties of liquid crystalline materials*. Gordon and Breach Science Publishers.
- KATO, T., HIRAI, Y., NAKASO, S. & MORIYAMA, M. 2007 Liquid-crystalline physical gels. *Chem. Soc. Rev.* **36**, 1857–1867.
- KEMPE, M. D., KORNFELD, J. A. & LAL, J. 2004 Chain Anisotropy of Side-Group Liquid Crystalline Polymers in Nematic Solvents. *Macromolecules* **37**, 8730–8738.
- KHAZIMULLIN, M., MÜLLER, T., MESSLINGER, S., REHBERG, I., SCHÖPF, W., KREKHOV, A., PETTAU, R., KREGER, K. & SCHMIDT, H.-W. 2011 Gel formation in a mixture of a block copolymer and a nematic liquid crystal. *Phys. Rev. E* **84**, 021710.
- KHOO, I.-C. & SIMONI, F. 1991 *Physics Of Liquid Crystalline Materials*. Gordon and Breach Science Publishers.
- KNIGHT, J. B., EHRICHS, E. E., KUPERMAN, V. Y., FLINT, J. K., JAEGER, H. M. & NAGEL, S. R. 1996 Experimental study of granular convection. *Phys. Rev. E* **54** (5), 5726–5738.
- KRALJ, S. & ŽUMER, S. 1992 Fréedericksz transitions in supra- μm nematic droplets. *Phys. Rev. A* **45** (4), 2461–2470.
- LEHMANN, O. 1889 Über fließende Kristalle. *Z. Phys. Chem.* **4**, 462 – 472.
- LÜDERS, K. & VON OPPEN, G. 2008 *Bergmann–Schäfer, Lehrbuch der Experimentalphysik, Band I: Mechanik, Akustik, Wärme*, 12. Auflage. Walter de Gruyter.
- MAIER, W. & SAUPE, A. 1959 Eine Einfache Molekular-Statistische Theorie der Nematischen Kristallinflüssigen Phase, I. *Z. Naturforsch.* **14a**, 882–889.
- MAIER, W. & SAUPE, A. 1960 Eine Einfache Molekular-Statistische Theorie der Nematischen Kristallinflüssigen Phase, II. *Z. Naturforsch.* **15a**, 287–292.

Bibliography

- MANSARÉ, T., DECRESSAIN, R., GORS, C. & DOLGANOV, V. K. 2002 Phase Transformations And Dynamics Of 4-Cyano-4'-Pentylbiphenyl (5cb) By Nuclear Magnetic Resonance, Analysis Differential Scanning Calorimetry, And Wideangle X-Ray Diffraction Analysis. *Mol. Cryst. Liq. Cryst.* **382**, 97–111.
- MAY, C., WILD, M., REHBERG, I. & HUANG, K. 2013 Analog of surface melting in a macroscopic nonequilibrium system. *Phys. Rev. E* **88**, 062201.
- MEHTA, A. 2007 *Granular Physics*. Cambridge University Press.
- MEHTA, A. & BARKER, G. C. 1994 The dynamics of sand. *Rep. Prog. Phys.* **57** (4), 383–416.
- MESCHEDÉ, D. 2006 *Gerthsen Physik*, 23. Auflage. Springer Verlag.
- MIZOSHITA, N., SUZUKI, Y., KISHIMOTO, K., HANABUSA, K. & KATO, T. 2002 Electrooptical properties of liquid-crystalline physical gels: a new oligo(amino acid) gelator for light scattering display materials. *J. Mater. Chem.* **12**, 2197–2201.
- MONTAINE, M., HECKEL, M., KRUELLE, C., SCHWAGER, T. & PÖSCHEL, T. 2011 Coefficient of restitution as a fluctuating quantity. *Phys. Rev. E* **84**, 041306.
- MOTTE, A. 1729 *The mathematical principles of natural philosophy by Isaac Newton (translation by Andrew Motte)*. London.
- MÜLLER, P., HECKEL, M., SACK, A. & PÖSCHEL, T. 2013a Complex Velocity Dependence of the Coefficient of Restitution of a Bouncing Ball. *Phys. Rev. Lett.* **110**, 254301.
- MÜLLER, T., GOLLWITZER, F., KRÜLLE, C. A., REHBERG, I. & HUANG, K. 2013b Scaling of the Normal Coefficient of Restitution for Wet Impacts. *AIP Conf. Proc.* **1542**, 787–790.
- MÜLLER, T., DE LAS HERAS, D., REHBERG, I. & HUANG, K. 2015 Ordering of Granular Rod Monolayers Driven Far from Thermodynamic Equilibrium. *Phys. Rev. E*, [arXiv:1503.03737](https://arxiv.org/abs/1503.03737), (under review).
- NARAYAN, V., MENON, N. & RAMASWAMY, S. 2006 Nonequilibrium steady states in a vibrated-rod monolayer: tetratic, nematic, and smectic correlations. *J. Stat. Mech.* **1**, P01005.
- NOLTING, W. 2005 *Grundkurs Theoretische Physik 4: Spezielle Relativitätstheorie, Thermodynamik*, 6. Auflage. Springer-Verlag.
- OLMSTED, J. A. & WILLIAMS, G. A. 1997 *Chemistry: The Molecular Science*, 2nd edition. Wm. C. Brown Publishers.
- ONSAGER, L. 1949 The Effects of Shape on the Interaction of Colloidal Particles. *Ann. NY Acad. Sci.* **51**, 627–659.

- PETTAU, R., MÜLLER, T., KHAZIMULLIN, M., REHBERG, I. & SCHMIDT, H.-W. 2012 Structure-Property Relations of Liquid Crystalline Gels with ABA-Triblock Copolymers as Gelators. *Z. Phys. Chem.* **226**, 645–664.
- POULIN, P. & WEITZ, D. A. 1998 Inverted and multiple nematic emulsions. *Phys. Rev. E* **57** (1), 626–637.
- RAMÍREZ, R., PÖSCHEL, T., BRILLIANTOV, N.V. & SCHWAGER, T. 1999 Coefficient of restitution of colliding viscoelastic spheres. *Phys. Rev. E* **60** (4), 4465–4472.
- REINITZER, F. 1888 Beiträge zur Kenntnis des Cholesterins. *Monatsh. Chem.* **9**, 421–441.
- ROTH, M., D'ACUNZI, M., VOLLMER, D. & AUERNHAMMER, G. K. 2010 Viscoelastic rheology of colloid-liquid crystal composites. *J. Chem. Phys.* **132**, 124702.
- RUSSEL, B. 2004 *History of Western Philosophy*. Routledge Classics.
- SÁNCHEZ, R. & HUERTA, A. 2014 Collapse-driven formation of a tetratic structure of confined quasi-2D granular tubes. *Rev. Mex. de Fís.* **60**, 119–122.
- SCHIMANK, H. 1960 Temperatur, Konstitution der Materie und Aggregatzustände: Zur Geschichte der Physik im 18. Jahrhundert. *Phys. Bl.* **16**, 417–425.
- SCHWAGER, T. & PÖSCHEL, T. 1998 Coefficient of normal restitution of viscous particles and cooling rate of granular gases. *Phys. Rev. E* **57** (1), 650–654.
- SCRUGGS, N. R., VERDUZCO, R., UHRIG, D., KHAN, W., PARK, S.-Y., LAL, J. & KORNFIELD, J. A. 2009 Self-Assembly of Coil/Liquid-Crystalline Diblock Copolymers in a Liquid Crystal Solvent. *Macromolecules* **42**, 299–307.
- STARK, H. 2001 Physics of colloidal dispersions in nematic liquid crystals. *Physics Reports* **351** (6), 387–474.
- TORQUATO, S. & STILLINGER, F. H. 2010 Jammed hard-particle packings: From Kepler to Bernal and beyond. *Rev. Mod. Phys.* **82**, 2633–2672.
- TSCHIRSKE, C. 2002 Liquid crystals stack up. *Nature* **419**, 681–683.
- VILLARRUEL, F.X., LAUDERDALE, B.E., MUETH, D.M. & JAEGER, H.M. 2000 Compaction of rods: Relaxation and ordering in vibrated, anisotropic granular material. *Phys. Rev. E* **61** (6), 6914–6921.
- VÖLTZ, C., MAEDA, Y., TABE, Y. & YOKOYAMA, H. 2006 Director-Configurational Transitions around Microbubbles of Hydrostatically Regulated Size in Liquid Crystals. *Phys. Rev. Lett.* **97**, 227801.
- WACHTER, A. & HOEBER, H. 2005 *Repetitorium Theoretische Physik*, 2. Auflage. Springer-Verlag.

Bibliography

YADAV, V., CHASTAING, J.-Y. & KUDROLLI, A. 2013 Effect of aspect ratio on the development of order in vibrated granular rods. *Phys. Rev. E* **88**, 052203.

Acknowledgement

There are many people who supported me in the past few years and who made a considerable contribution to the success of my work. Thus, I would like to express my special gratitude at the end of this thesis.

First of all I would like to thank Prof. Dr. Ingo Rehberg for giving me the opportunity to work at his chair and to expand my knowledge in experimental physics. I enjoyed his way of supervision during my years at EPV, with a free working atmosphere that broadened my self-dependence. His regular feedback in our weekly discussions guided me in the right direction.

I am also thankful to Dr. Wolfgang Schöpf. He supported me in many issues within the liquid crystal group and always gave constructive feedback to my results. Besides, I would like to thank Dr. Kai Huang, who gave me the possibility to enter the sandgroup during my second period at EPV. He introduced me into the physics of granular matter and supported me in every way.

Furthermore, I would like to thank my room mate Stephan Messlinger. Whatever problem arose, especially on electronic devices, he was always willing to help. He was also the right person for discussions about any kind of physical problem. In a similar manner, Dr. Thomas Friedrich was also a colleague for motivated discussions and spontaneous coffee breaks at any time. Thank you, Stephan and Thomas!

Many of the experiments would have never taken place without the great technical support of Klaus Oetter and his close collaboration with the mechanical workshop. Thank you Klaus for all the help, for the construction of various experimental set-ups and the immediate realization of any kind of idea. My thanks go also to our secretary Christine Linser. She always assisted me with any administrative question and found an uncomplicated and immediate solution, no matter what problems arose. There are many others at EPV, technicians, bachelor, master and diploma students, who all made their contribution to the progress of our scientific research and generated a great working atmosphere at the chair. Thanks to all of them!

I also had the opportunity for fruitful collaborations with several scientists besides of EPV during the last few years. I am grateful for the possibility to benefit from their expert knowledge and for the chance to collectively publish some of my experimental results. Thus, I would like to thank all the coauthors of the publications that are summarized in this thesis. Especially, I would like to thank Dr. Maxim Khazimullin who introduced me to the experiments with liquid crystalline materials. Even after his return to Russia, he kept having a sympathetic ear for any of my questions. I would also like to thank Dr. Alexei Krekhov for helpful discussions about the theoretical understanding of liquid crystalline systems. A special thanks goes to Dr. Robin Pettau for synthesizing the liquid crystalline polymers and broadening my knowledge

about the chemical background of polymeric liquid crystals. Unfortunately, he left us far too early. I am also thankful to Daniel de las Heras for the nice collaboration and the inspirational time during my work on the granular rods project.

Many scientific and nonscientific encounters during my time at the University of Bayreuth evolved into close friendships. I would like to thank all of them for moral support and all the activities besides of the work. In particular, I would like to mention Dr. Martin Gläsel and thank him for proof reading my thesis.

Last but not least, I want to thank all of my family. They kept me grounded and gave me the opportunity of a carefree academic study and doctoral time. Especially I am grateful to my wife Regina. She is the person I can count on day and night. She is the person supporting me with all her energy. Even in stressful times, she is always patient and understanding. Thank you for all the great moments I could share with you during the last years. Hopefully, we will experience many more in our gradually growing family in the future!

Eidesstattliche Versicherung

Hiermit versichere ich an Eides statt, dass ich die vorliegende Arbeit selbstständig verfasst und keine anderen als die von mir angegebenen Quellen und Hilfsmittel verwendet habe.

Zusätzlich erkläre ich hiermit, dass ich keinerlei frühere Promotionsversuche unternommen habe.

Weiterhin erkläre ich, dass ich die Hilfe von gewerblichen Promotionsberatern bzw. -vermittlern oder ähnlichen Dienstleistern weder bisher in Anspruch genommen habe, noch künftig in Anspruch nehmen werde.

Bayreuth, den 18.05.2015

Thomas Müller

